Decarbonization of Engineered Cementitious Composites (ECC)

by

Weihsiu Hu

A dissertation submitted in partial fulfillment
of the requirements for the degree of
Doctor of Philosophy
(Civil Engineering)
in the University of Michigan
2023

Doctoral Committee:

Associate Professor Brian R. Ellis, Co-Chair
Professor Victor C. Li, Co-Chair
Professor Jerome P. Lynch, Duke University
Professor Steve Skerlos
Professor Duo Zhang, Wuhan University

Weihsiu Hu

hwhsiu@umich.edu

ORCID iD: 0000-0001-6789-0456

ACKNOWLEDGMENTS

First and foremost, I would like to thank my advisors, Professor Victor C. Li and Professor Brian R. Ellis, for their continuous support throughout my four-year Ph.D. study and research. Despite the significant challenges posed by the widespread outbreak of the COVID-19 pandemic during my doctoral journey, I completed my thesis owing to their invaluable guidance, inspiration, and encouragement.

I would like to thank Professor Duo Zhang for his valuable suggestions and guidance in carbonation curing and low-carbon ECC research. I also thank Dr. Zhu He for his inspiring suggestions.

I sincerely thank Professor Jerome P. Lynch and Professor Steve Skerlos for serving as my committee members and for their valuable comments and suggestions.

I would like to thank Professor Esayas G. Ftwi for his help developing sisal fiber and his kind support in the experiments. I also want to thank Professor Suleyman H. Gokce and Professor Kequ Yu for their great help during their visiting scholarship.

I would like to acknowledge Mr. Justin Roelofs for his valuable help in setting up the experiments and designing useful molds for my research. I would like to thank Mr. Steve Donajkowski, Mr. Jan Pantolin, and Mr. Ethan Kennedy for their kind laboratory support.

I would like to thank my colleagues, Ms. Mengjun and Ms. Wen Zhou, for their kind help in research and friendships. Dr. Jubilee Adeoye, Ms. Ellen Thompson, Dr. Anne Menefee, Dr. Tae Hwan Lim, Ms. Eva Albalghiti, Mr. Tianyu Wang, Mr. Yichao Wang, Dr. Hugo, and the others for their kind assistance. I am grateful to my friends, Mr. Yuhsuan Tong, Mr. Yuehhan Wu, Mr. Jintian Lian, Mr. Jianda Lin, Mr. Weitai Chen, Mr. Yancheng Jian, Mr. Jiawei Shiu, Ms. Chiehying Chen, and many other friends for their friendships during my study.

I am so grateful to my wife, YiAn. She has provided me with a warm and lovely family environment that supports me in completing this thesis. I want to thank my parents for their encouragement during these four years.

Finally, I wish everyone good fortune, health, and happiness!

Weihsiu Hu

TABLE OF CONTENTS

LIST OF TABLES

LIST OF FIGURES

ABSTRACT

Mitigating CO_2 emissions has emerged as one of the most critical global challenges. The concrete industry comprises approximately 8% of global CO_2 emissions due primarily to the large carbon footprint from ordinary Portland cement (OPC) production. Concrete's brittle nature necessitates early infrastructure reconstruction and rehabilitation, leading to high operational embodied carbon emissions throughout its service life. Engineered cementitious composites (ECC) have demonstrated a capacity to enhance structural fatigue resistance and reduce CO_2 emissions during the use phase through their high tensile performance and crack width control capability. However, ECC's high cement content and use of synthetic fiber incur substantial economic and environmental costs. Therefore, there is an urgent need to address ECC's high embodied carbon footprint during the production phase if it is to be used as a sustainable alternative to traditional concrete.

The goals of this doctoral research encompass the development of strategies to decarbonize ECC while maintaining its unique ductile performance and showcasing its economic and environmental competitiveness compared to regular concrete. Three major approaches are proposed in this research, including carbon sequestration through carbonation curing, the use of industrial waste materials (IWMs), and the employment of localized materials. The impacts of carbonation curing on ECC are investigated, such as changes to mechanical and micromechanical properties. With the incorporation of IWMs, a low-carbon sustainable WPE-ECC is designed by substituting virgin polyethylene (PE) fiber with waste polyethylene fiber (WPE) from waste marine fishing nets. The low carbon ECC's mechanical properties, including compressive, tensile, flexural strength, and ductility, are examined. Considering the increasing cost and limited availability of commonly used IWMs such as fly ash and manufactured silica sand, a case study of the Kingdom of Saudi Arabia examines replacing these materials with locally available alternatives, namely volcanic ash (VA) and desert sand (DS), to mitigate the embodied carbon and cost associated with long-distance material transportation. A localized self-stressing VA-DS-ECC is developed and optimized to mitigate challenges posed by alternative materials and ensure a

sufficient working time window and mechanical performance of the ECC. The reductions of embodied carbon footprint and cost for each of these three approaches are quantified and compared to conventional concrete materials.

Results indicate that carbonation curing significantly improves fatigue life and reduces the midspan deflection of ECC. CO_2-cured ECC exhibits approximately 20% CO_2 uptake per cement mass. Carbonation curing increases ECC's flexural strength and promotes effective crack width control, resulting in reduced post-fatigue crack width. The positive impact of carbonation curing on the fatigue behavior of ECC can simultaneously lower the embodied and operational carbon of ECC structural members during service.

In the case of the IWMs method, the findings suggest that carbonation-cured WPE-reinforced ECC has only 50% of the CO_2 footprint and 67% of the cost of conventional concrete. Meanwhile, this low-carbon ECC maintains at least 4 MPa tensile strength and 6% tensile ductility, demonstrating the feasibility of developing environmentally-friendly construction materials without compromising high performance for civil infrastructure applications. Similarly, the localized self-stressing ECC exhibits comparable mechanical performance to other ECC grades, showing the feasibility of replacing FA and silica sand with locally available materials, resulting in a low-carbon ECC with promising implications for practical construction applications.

This research provides three distinct approaches for ECC decarbonization that can be integrated with one another, offering a potential pathway into the construction industry that urgently needs to be decarbonized.

Chapter 1. Introduction

1.1. Background

Engineered cementitious composites (ECC), also known as bendable concrete, belongs to the broad fiber-reinforced concrete (FRC) class. While FRC typically undergoes tension-softening after the initiation of the first crack [1], ECC demonstrates strain-hardening behavior that limits tensile deformation by generating multiple microcracks. This unique characteristic imparts ECC with a superior tensile ductility exceeding 2%. In recent studies, ECC has even achieved a tensile ductility of over 8% [2–4] with a wide range of compressive and tensile strength feasible [5]. The high deformability of ECC surpasses brittle fracture, making it a promising material for infrastructure applications. Noteworthy examples include using ECC in constructing the Michigan bridge deck [6] and the Tokyo high-rise [7], where it has demonstrated earthquake resiliency and durability enhancement, as shown in Figure 1-1. The high performance of ECC-based infrastructure contributes significantly to reducing maintenance and repair needs, thus reducing the use phase operation carbon footprint. However, ECC's extensive high embodied carbon footprint and material costs hinder its broader applications.

The mitigation of CO_2 emissions has been recognized as a critical global challenge by the U.S. National Academy of Engineering. Despite current efforts for all countries to meet the targets set by the Paris climate agreement, it is estimated that global warming will still reach 2.6-3.2 ℃ by 2100. (refer to Figure 1-2(a)) [8]. A substantial reduction in global greenhouse gas is required to achieve the Intergovernmental Panel on Climate Change (IPCC) recommendation of keeping warming below 1.5 ℃ [9]. The concrete industry is a notable CO_2 emissions contributor, with Portland cement, a primary component of concrete, accounting for 6~8% of anthropogenic CO_2 emissions during its production [8–10], as shown in Figure 1-2(b). As the global construction market continues to expand, practical strategies to mitigate concrete CO_2 footprint for both the material production phase and that associated with the structural product use phase are urgently needed.

ECC exhibits high tensile ductility several hundred times that of regular concrete and autogenous crack width control capacity [5,11]. The intrinsic tight crack width of ECC, even under high strain, results in lower water permeability [12] and chloride diffusivity [13], enhancing infrastructure durability and reducing operational carbon and energy footprints [14]. Thus, low maintenance of ECC infrastructure is needed, suggesting a low operation carbon footprint in the use phase of the infrastructure life-cycle. However, unlike typical high-strength or ultra-high-performance concrete, which relies on dense particle packing, ECC is systematically designed by synergistic interactions between fiber, matrix, and the fiber/matrix interface [15,16]. It requires ECC to eliminate the coarse aggregate and implement a significant amount of cement, as well as synthetic fiber such as polyethylene (PE), polypropylene (PP), or polyvinyl alcohol (PVA) fiber, to achieve such synergistic interactions. As a result, ECC shows a high embodied CO_2 footprint. For example, a typical well-studied M45 ECC mixture possesses an embodied carbon footprint twice that of conventional concrete [17]. Therefore, urgent efforts are required to find approaches to decarbonize the ECC.

To address this concern, three methods were employed to reduce the carbon emissions associated with ECC: carbonation curing, the use of industrial waste materials (IWMs), and utilizing localized materials. Carbonation curing, which is suitable for the precast industry [18], involves the conversion of CO_2 to $CaCO_3$, thereby sequestrating carbon and lowering the overall CO_2 footprint. However, the impacts of carbon curing on ECC performance, specifically the fatigue performance, are not well studied. It is necessary to clarify the flexural fatigue behavior of ECC after carbonation curing and fill existing knowledge gaps.

The adoption of IWMs, such as fly ash, limestone calcined clay cement (LC3), and ground granulated blast-furnace slag (GGBFS), as substitutes for raw materials in typical ECC mixtures [19–24] represents another approach to mitigate the high embodied carbon footprint of ECC [14]. However, even with these IWMs, the CO_2 footprint of ECC remains higher than that of conventional concrete. No ECC has an embodied carbon footprint lower than concrete [17]. Moreover, the availability and cost of widely used IWMs, such as fly ash, are subject to fluctuations due to the future decline in the operation of coal combustion plants [25,26]. Additionally, in certain regions, particularly in the Middle East, the primary power generation sources are oil and natural gas, with coal contributing only a minor fraction to the power supply [27,28], leading to high costs and carbon footprint associated with long-distance transportation for

those IWMs like FA should also be considered. Thus, finding suitable locally available IWMs alternatives to substitute FA in ECC is imperative. Developing a low-carbon ECC utilizing IWMs and potentially new localized IWMs is also crucial.

(a) (b)

Figure 1-1. ECC field-scale applications of (a) durability enhancement in Michigan bridge deck [6] and (b) earthquake resiliency enhancement for Tokyo high-rise [7]

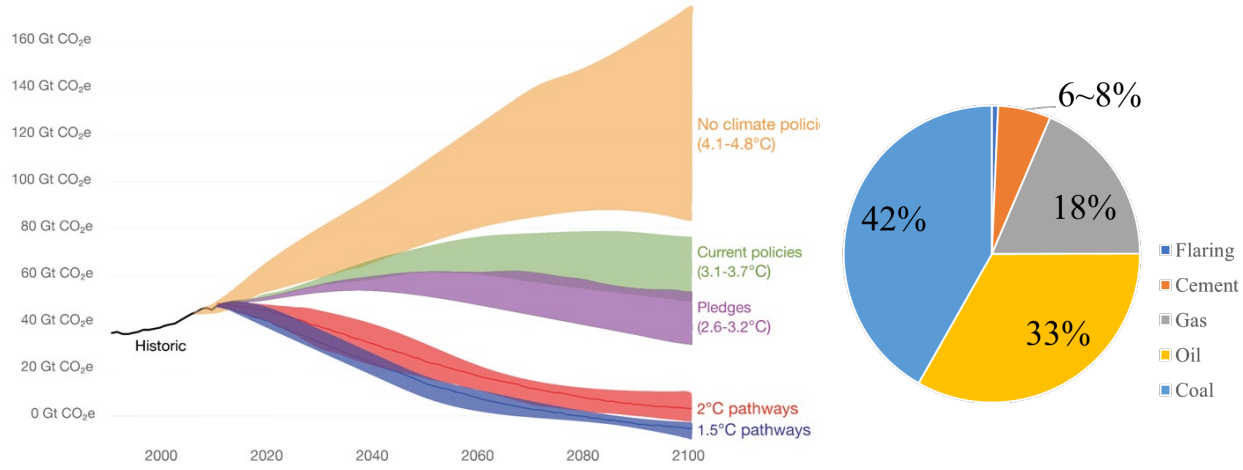

(a) (b)

Figure 1-2. (a) Global greenhouse gas emissions scenarios and (b) World CO_2 emissions by fuel and industrial production [8].

1.2. Review on carbonation curing and Industrial waste materials (IWMs)

Over the past few decades, considerable research efforts have been dedicated to utilizing IWMs in ECC. The concept of carbonation curing for ECC has also emerged in recent years. This section presents a brief overview of the basic information, including the typical carbonation process for carbonation-cured ECC and commonly used IWMs in ECC.

1.2.1 Carbonation curing

Carbonation curing is one of the methods for carbon sequestration in the precast industry. At the early-stage hydration process, CO_2 reacts with Portland cement and its hydration products to form calcium carbonate ($CaCO_3$). Meanwhile, carbonation curing can also improve the ultimate tensile and compressive strength at early ages due to the accelerated cement reaction [18]. Carbonation curing leads to a denser microstructure due to $CaCO_3$ precipitation [29,30], which is proven to enhance the material durability in various environments, such as during sulfate and acid attack, freeze-thaw deterioration, and chloride permeation [31–34].

The corresponding reactions for carbon sequestration via carbonation curing are governed by the following Equation (1-1) to (1-4) [35]:

$$2C_3S + 11H \rightarrow C_3S_2H_8 + 3CH \quad (1\text{-}1)$$

$$2C_2S + 9H \rightarrow C_3S_2H_8 + CH \quad (1\text{-}2)$$

$$CH + CO_2 \rightarrow CaCO_3 + H \quad (1\text{-}3)$$

$$C - S - H + 2CO_2 \rightarrow 2SiO_2 + 2CaCO_3 + H \quad (1\text{-}4)$$

where C_3S and C_2S represents the tricalcium and dicalcium silicate from cement, respectively. The hydration reactions of both calcium silicates with water (H) in Equation (1-1) and Equation (1-2) will form the Calcium hydroxide (CH) and Calcium silicate hydrate ($C_3S_2H_8$, C-S-H gel). Then, CH will capture the CO_2 and sequestrate it in the cementitious matrix in the format of Calcite (CH). Furthermore, the C-S-H gel generated by the hydration process in Equation (1-1) and Equation (1-2) also undergoes a reaction with CO_2. Both the carbon sequestration process of Equation (1-3) and Equation (1-4) will release water, which should be noted when using the mass loss [30] method to calculate the CO_2 sequestration ratio.

A standard carbonation process for lab-scale specimens was proposed to achieve efficient carbon sequestration, as depicted in Figure 1-3. All samples were de-molded after 18 hours of casting. Then, samples were fan dried in air for 4-8 hours, suggested by previous studies to evaporate capillary pore water for a better pathway for CO_2 diffusion [35,36]. Afterward, specimens would be cured in CO_2 for 24 hours in a pressure chamber, as shown in Figure 1-4. The CO_2 gas pressure was kept at 5 bar [18]. A whole range of different drying times, curing times and pressures were examined. For example, tested CO_2 pressures ranged from atmospheric up to supercritical CO_2 pressure. Pressures above 5 bar showed diminishing returns on additional carbonation, so 5 bar CO_2 pressure was chosen as the upper bound for CO_2 curing in this work. Similarly, if the curing time is less than 24 hours, the CO_2 uptake for the specimens will be limited. Extending the curing time beyond 48 hours is inefficient for precast manufacturing. Subsequently, samples were cured in the air at 20 ± 2°C and RH of 65 ± 2 until 28 days for mechanical experiments [37].

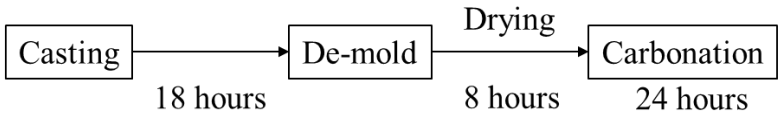

Figure 1-3. Typical carbonation process for lab-scale specimens

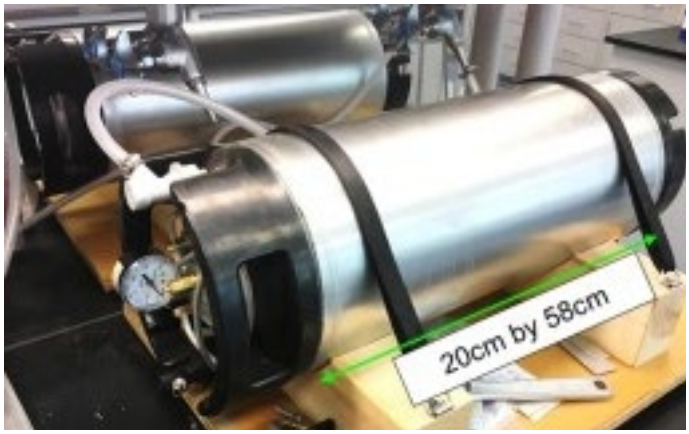

Figure 1-4. Lab-scale pressure chamber for carbonation curing [18].

1.2.2 Commonly used industrial waste materials (IWMs)

As mentioned in section 1.1, IWMs were widely used as substitution materials for ECC, which can be defined as three parts: binder (cement), filler (sand), and fiber [14] (see Figure 1-5). Finding IWMs among these groups will help design a low-carbon, green ECC.

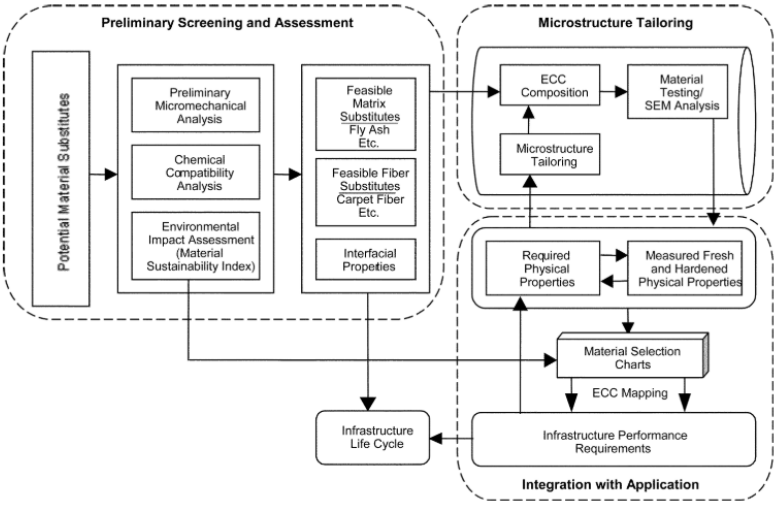

Figure 1-5. Schematic of green ECC materials development framework by Lepech et al. [14].

The widely used precursor substitution materials for cement are fly ash and ground granulated blast-furnace slag (GGBFS). Fly ash can enhance matrix workability and self-consolidating processing due to the round shape of fly ash particles. It can also reduce the heat of hydration and drying shrinkage of ECC [22]. GGBFS has also been found to improve fiber dispersion, thus enhancing the tensile properties of ECC [23,24]. More IWMs have been investigated in recent years outside these two well-known cement supplementary materials. Nematollahi et al. [38] created a geopolymer composite using four different mix proportions to fabricate ECC, and all mix proportions successfully achieved strain-hardening behavior [38]. Yu et al. [4] fabricated ultra-high performance engineered cementitious composites (UHP-ECC) that incorporated recycled fine powder (RFP, a combination of concrete and clay brick powder). With the use of RFP, the average crack width was reduced, and the early strength of ECC also increased due to the accelerated hydration process [4]. Zu et al., Yu et al., and Zhang et al. [19–21] used limestone calcined clay

cement (LC3) as a cement substitution material. They discovered that ECC's tensile ductility and crack width control capacity improved.

Adesina and Das [39] and Siad et al. [40] used recycled glass sand (GS) to substitute the filler (sand) part of ECC, which enhanced the compressive, tensile, and flexural properties of ECC mixtures. Local desert sand was used by Che et al. and Wu et al. [41,42] to reduce the transport cost and carbon footprint associated with the transportation of heavy silica sand while maintaining comparable performance with silica sand ECC. Li and Yang [43] implemented recycled concrete fines (RCF, fine aggregates, and particles from the demolition waste of old concrete) as the silica sand substitute in ECC production. Lepech et al. [14] used waste foundry sand (WFS) (also called molding sand) to design a green ECC. At the same time, the performance of the ECC slightly decreased due to an imbalance of carefully controlled fiber, matrix, and fiber-matrix properties.

It should be noted that the American Foundry Society indicated that less than 30% of the 10 million tons of WFS that are generated annually are recycled [44]. Nearly 7 million tons of WFS can be safely used and economically recycled, according to the United States Environmental Protection Agency (EPA) [45]. The tremendous amount of WFS can lead to lower production costs and a further reduction in the CO_2 footprint of ECC. Therefore, WFS becomes a good potential IWMs that could be applied to ECC.

It is more difficult to substitute fiber with IWMs since, according to Li et al. [11], fibers must have a minimum tensile strength of 1000 MPa, an inelastic failure strain more significant than 5%, and a suitable diameter. There are still some recycled/waste fibers that meet these criteria. The cost and energy consumption of High-tenacity polypropylene fiber (HTPP) fiber is lower than PVA fibers with comparable performance under proper mix design [46,47]. Singh et al. and Yu et al. [48,49] used recycled polyethylene terephthalate fiber (PET) and PVA fiber to enhance the properties of ECC by bridging the effect between hybrid fibers.

Using the IWMs above can mitigate ECC's CO_2 footprint and energy costs. However, there are also some limitations to using these materials. Geopolymer matrix typically involves more design variables than cement matrix [50], and the compressive strength of LC3-ECC is lower than OPC-ECC [19]. Alkali–silica reaction has been reported as the major problem affecting the use of GS [51]. Desert sand’s physical properties and material composition from different places show significant variability [52].

1.3. Thesis objectives and outline

The goal of having sustainable infrastructure becomes attainable through incorporating ECC, considering the superior durability of its intrinsic tight crack width and extended fatigue performance, leading to reduced operational carbon footprint of infrastructures. However, the high embodied carbon footprint and costs for ECC production impeded its further adoption by manufacturers. The main objective of this thesis is to develop ECC materials with a significantly lower carbon footprint than conventional concrete while preserving the unique high tensile ductility characteristics of the ECC family of composite materials via the proposed three approaches: carbonation curing, use of IWMs, and localized materials.

This thesis is structured in five chapters covering the scope of the study: Decarbonization of engineered cementitious composites (ECC). The detailed thesis research framework is shown in Figure 1-6.

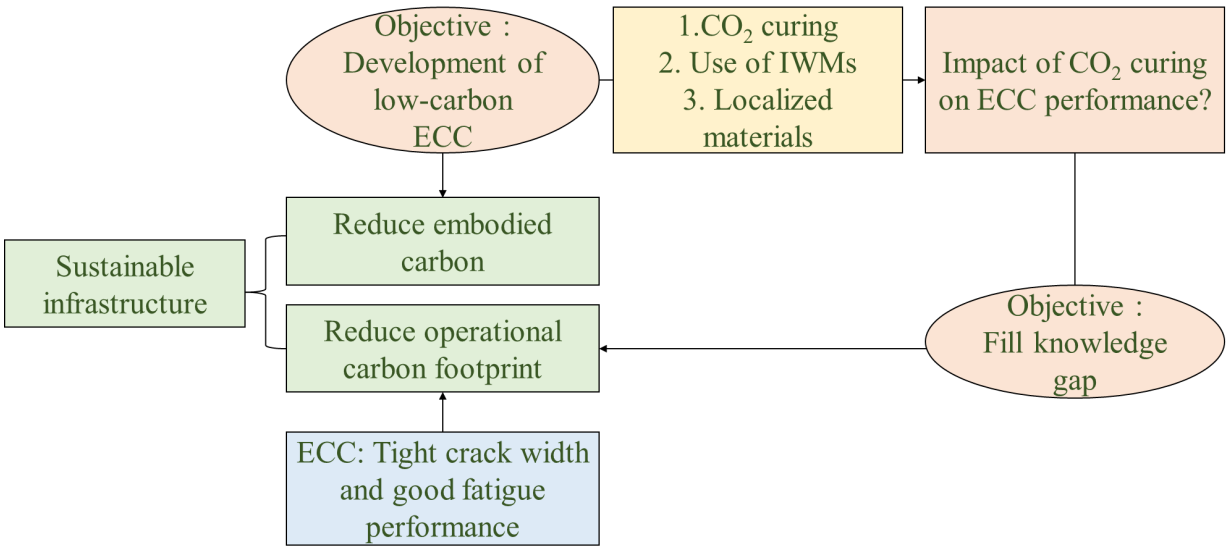

Figure 1-6. Thesis research framework.

Chapter 1 demonstrates the research background, a fundamental review of carbonation curing, IWMs commonly used in the past decades, and the thesis objectives and outline.

Chapter 2 provides the impact of carbonation curing on ECC. Two curing conditions were considered (carbonation curing and air curing). The failure mechanism and multiple cracking behaviors of the carbonation-cured and air-cured ECC were investigated. ECC beams were

prepared and tested under four-point static and fatigue bending load for midspan deflection evolution and fatigue stress-life relationship. Single fiber pullout tests were also conducted to determine the interfacial bond between fibers and cementitious matrix as affected by carbonation curing. The fiber bridging degradation was evaluated by optical microscopy. By assessing the flexural fatigue behavior of CO_2-cured ECC, Chapter 2 experimentally validates the ability to synergistically reduce embodied and operational carbon through ECC's carbonation curing, thus contributing to the sustainability of civil infrastructure.

Chapter 3 investigates a low-carbon and low-cost ECC. By combining the CO_2 sequestration method from Chapter 2, a low-carbon binder, and waste fiber utilization, Chapter 3 presents a sustainable ECC with comparable cost and CO_2 footprint to conventional concrete while recycling the plastic marine waste (waste marine fishing nets: waste polyethylene fiber (WPE)). A comprehensive experimental program was initiated using LC3, WPE, WFS, sisal fiber, and carbonation curing, including compressive strength, uniaxial tensile strength, crack patterns, interfacial bonding strength, cost, embodied carbon footprint, and energy evaluation. To identify the effects of adding sisal fiber on ECC's mechanical properties and carbonation efficiency, different amounts of sisal fiber were considered for both carbonation and air curing conditions for Portland cement ECC (OPC-ECC). For the one with the best performance, OPC was substituted by LC3 or WFS to minimize the cost and embodied carbon footprint. Thermogravimetric analysis (TGA) was used to evaluate the CO_2 uptake of ECC mix proportions. Single fiber pull-out tests were conducted on WPE and sisal fiber to determine the interfacial bond between the fiber and cementitious matrix.

Chapter 4 demonstrates the substitution of FA and silica sand with locally available materials: DS and volcanic ash (VA) for the Middle East regions. A durable self-stressing ECC utilizing VA, DS, and low content of CSA, which allows a sufficient construction time window in the summer season, is developed. Embodied carbon footprint is also compared between FA-ECC and the localized materials ECC (DS-VA-ECC). Through different water-to-binder ratio (W/B ratio), CSA dosages, and curing conditions, a comprehensive experimental program was conducted to evaluate the tensile performance, compressive strength, flexural strength, crack patterns, shrinkage, cost and embodied carbon footprint of DS-VA-ECC. Different W/B ratios were fabricated to identify the most suitable one based on its mechanical performance and

workability. Subsequently, modifications were made to CSA dosages and curing conditions to achieve optimal working time windows and self-stressing characteristics. X-ray Diffraction (XRD) and an optical microscope were carried out to investigate the mechanisms traced to the microstructure.

Chapter 5 summarizes the overall conclusions from this thesis, provides recommended future works, and identifies potential obstacles along the way.

1.4. Reference

[1] L. Xiaopeng, M. Li, G. Song, Energy-dissipating and self-repairing SMA-ECC composite material system, Smart Mater Struct. 24 (2015). https://doi.org/10.1088/0964-1726/24/2/025024.

[2] K. Yu, Y. Wang, J. Yu, S. Xu, A strain-hardening cementitious composites with the tensile capacity up to 8%, Constr Build Mater. 137 (2017) 410–419. https://doi.org/10.1016/j.conbuildmat.2017.01.060.

[3] K.Q. Yu, J.T. Yu, J.G. Dai, Z.D. Lu, S.P. Shah, Development of ultra-high performance engineered cementitious composites using polyethylene (PE) fibers, Constr Build Mater. 158 (2018) 217–227. https://doi.org/10.1016/j.conbuildmat.2017.10.040.

[4] K.Q. Yu, W.J. Zhu, Y. Ding, Z.D. Lu, J. tao Yu, J.Z. Xiao, Micro-structural and mechanical properties of ultra-high performance engineered cementitious composites (UHP-ECC) incorporation of recycled fine powder (RFP), Cem Concr Res. 124 (2019) 105813. https://doi.org/10.1016/j.cemconres.2019.105813.

[5] V.C. Li, Engineered Cementitious Composites – Bendable Concrete for Sustainable and Resilient Infrastructure, Springer, Germany, 2019. https://doi.org/10.1007/978-3-662-58438-5.

[6] M.D. Lepech, V.C. Li, Application of ECC for bridge deck link slabs, in: Materials and Structures/Materiaux et Constructions, 2009: pp. 1185–1195. https://doi.org/10.1617/s11527-009-9544-5.

[7] M. Maruta, T. Kanda, S. Nagai, Y. Yamamoto, New High-rise RC Structure Using Pre-cast ECC Coupling Beam, Concrete Journal. 43 (2005) 11.

[8] H. Ritchie, M. Roser, P. Rosado, CO_2 and Greenhouse Gas Emissions, OurWorldInData. (2020). https://ourworldindata.org/co2-and-greenhouse-gas-emissions (accessed March 10, 2023).

[9] M.D. Valérie, P. Zhai, H.O. Pörtner, D. Roberts, J. Skea, P.R. Shukla, A. Pirani, IPCC report Global warming of 1.5°C, IPCC. (2018). www.environmentalgraphiti.org.

[10] Y.C. Díaz, S.S. Berriel, U. Heierli, A.R. Favier, I.R.S. Sánchez Machado, K.L. Scrivener, J.F. Martirena Hernández, G. Habert, Limestone calcined clay cement as a low-carbon solution to meet expanding cement demand in emerging economies, Dev Eng. 2 (2017) 82–91. https://doi.org/10.1016/j.deveng.2017.06.001.

[11] V.C. Li, S. Wang, C. Wu, Tensile strain-hardening behavior or polyvinyl alcohol engineered cementitious composite (PVA-ECC), ACI Mater J. 98 (2001) 483–492. https://doi.org/10.14359/10851.

[12] M.D. Lepech, V.C. Li, Water permeability of engineered cementitious composites, Cem Concr Compos. 31 (2009) 744–753. https://doi.org/10.1016/j.cemconcomp.2009.07.002.

[13] M. Sahmaran, M. Li, V.C. Li, Transport Properties of Engineered Cementitious Composites Under Chloride Exposure, ACI Mater J. 104 (2007) 604–611.

[14] M.D. Lepech, V.C. Li, R.E. Robertson, G.A. Keoleian, Design of green engineered cementitious composites for improved sustainability, ACI Mater J. 105 (2008) 567–575. https://doi.org/10.14359/20198.

[15] V. Li, Tensile strain-hardening behavior or polyvinyl alcohol engineered cementitious composite (PVA-ECC), ACI Mater J. (2001). https://www.researchgate.net/publication/279888212.

[16] V. Li, On Engineered Cementitious Composites (ECC) A Review of the Material and Its Applications, Journal of Advanced Concrete Technology. 1 (2003) 215–230. https://www.researchgate.net/publication/237783722.

[17] D. Shoji, Z. He, D. Zhang, V.C. Li, The greening of engineered cementitious composites (ECC): A review, Constr Build Mater. 327 (2022). https://doi.org/10.1016/j.conbuildmat.2022.126701.

[18] D. Zhang, B.R. Ellis, B. Jaworska, W.H. Hu, V.C. Li, Carbonation curing for precast Engineered Cementitious Composites, Constr Build Mater. 313 (2021). https://doi.org/10.1016/j.conbuildmat.2021.125502.

[19] H. Zhu, D. Zhang, T. Wang, H. Wu, V.C. Li, Mechanical and self-healing behavior of low carbon engineered cementitious composites reinforced with PP-fibers, Constr Build Mater. 259 (2020) 119805. https://doi.org/10.1016/j.conbuildmat.2020.119805.

[20] J. Yu, H.L. Wu, C.K.Y. Leung, Feasibility of using ultrahigh-volume limestone-calcined clay blend to develop sustainable medium-strength Engineered Cementitious Composites (ECC), J Clean Prod. 262 (2020). https://doi.org/10.1016/j.jclepro.2020.121343.

[21] D. Zhang, B. Jaworska, H. Zhu, K. Dahlquist, V.C. Li, Engineered Cementitious Composites (ECC) with limestone calcined clay cement (LC3), Cem Concr Compos. 114 (2020). https://doi.org/10.1016/j.cemconcomp.2020.103766.

[22] E.H.Yang, Y.Yang, V.C.Li, Use of high volumes of fly ash to improve ECC mechanical properties and material greenness, ACI Mater. J. 104 (2007) 620–628.

[23] I. Lim, J.C. Chern, T. Liu, Y.W. Chan, Effect of ground granulated blast furnace slag on mechanical behavior of PVA-ECC, Journal of Marine Science and Technology (Taiwan). 20 (2012) 319–324. https://doi.org/10.51400/2709-6998.1810.

[24] J.K. Kim, J.S. Kim, G.J. Ha, Y.Y. Kim, Tensile and fiber dispersion performance of ECC (engineered cementitious composites) produced with ground granulated blast furnace slag, Cem Concr Res. 37 (2007) 1096–1105. https://doi.org/10.1016/j.cemconres.2007.04.006.

[25] E. Ghafari, D. Feys, K. Khayat, Feasibility of using natural SCMs in concrete for infrastructure applications, Constr Build Mater. 127 (2016) 724–732. https://doi.org/10.1016/j.conbuildmat.2016.10.070.

[26] I. Diaz-Loya, M. Juenger, S. Seraj, R. Minkara, Extending supplementary cementitious material resources: Reclaimed and remediated fly ash and natural pozzolans, Cem Concr Compos. 101 (2019) 44–51. https://doi.org/10.1016/j.cemconcomp.2017.06.011.

[27] S. Dietmar, A.R. Mohamed Jameel, Middle East Power Outlook 2035, 2017.

[28] W. Matar, R. Echeverri, A. Pierru, The Prospects for Coal-fired Power Generation in Saudi Arabia, 2015.

[29] V. Rostami, Y. Shao, A.J. Boyd, Z. He, Microstructure of cement paste subject to early carbonation curing, Cem Concr Res. 42 (2012) 186–193. https://doi.org/10.1016/j.cemconres.2011.09.010.

[30] D. Zhang, T. Liu, Y. Shao, Weathering Carbonation Behavior of Concrete Subject to Early-Age Carbonation Curing, Journal of Materials in Civil Engineering. 32 (2020) 04020038. https://doi.org/10.1061/(asce)mt.1943-5533.0003087.

[31] V. Rostami, Y. Shao, A.J. Boyd, Durability of concrete pipes subjected to combined steam and carbonation curing, Constr Build Mater. 25 (2011) 3345–3355. https://doi.org/10.1016/j.conbuildmat.2011.03.025.

[32] D. Zhang, B. Jaworska, Effect of Carbonation Curing on Portland Cement MgSO4 Attack: Laboratory Characterization at 900 Days, Journal of Materials in Civil Engineering. 33 (2021) 04021032. https://doi.org/10.1061/(asce)mt.1943-5533.0003647.

[33] D. Zhang, Y. Shao, Surface scaling of CO2-cured concrete exposed to freeze-thaw cycles, Journal of CO2 Utilization. 27 (2018) 137–144. https://doi.org/10.1016/j.jcou.2018.07.012.

[34] D. Zhang, Y. Shao, Enhancing chloride corrosion resistance of precast reinforced concrete by carbonation curing, ACI Mater J. 116 (2019) 3–12. https://doi.org/10.14359/51714461.

[35] D. Zhang, Y. Shao, Early age carbonation curing for precast reinforced concretes, Constr Build Mater. 113 (2016) 134–143. https://doi.org/10.1016/j.conbuildmat.2016.03.048.

[36] D. Zhang, X. Cai, Y. Shao, Carbonation Curing of Precast Fly Ash Concrete, Journal of Materials in Civil Engineering. 28 (2016) 04016127. https://doi.org/10.1061/(asce)mt.1943-5533.0001649.

[37] H.L. Wu, D. Zhang, B.R. Ellis, V.C. Li, Development of reactive MgO-based Engineered Cementitious Composite (ECC) through accelerated carbonation curing, Constr Build Mater. 191 (2018) 23–31. https://doi.org/10.1016/j.conbuildmat.2018.09.196.

[38] B. Nematollahi, J. Sanjayan, F.U.A. Shaikh, Comparative deflection hardening behavior of short fiber reinforced geopolymer composites, Constr Build Mater. 70 (2014) 54–64. https://doi.org/10.1016/j.conbuildmat.2014.07.085.

[39] A. Adesina, S. Das, Mechanical performance of engineered cementitious composite incorporating glass as aggregates, J Clean Prod. 260 (2020). https://doi.org/10.1016/j.jclepro.2020.121113.

[40] H. Siad, M. Lachemi, M. Sahmaran, K.M. Anwar Hossain, Potential for using waste recycled glass in engineered cementitious composites, Am. Concr. Institute, ACI Spec. Publ. (2017) 408–420.

[41] J. Che, D. Wang, H. Liu, Y. Zhang, Mechanical properties of desert sand-based fiber reinforced concrete (DS-FRC), Applied Sciences (Switzerland). 9 (2019). https://doi.org/10.3390/app9091857.

[42] H.L. Wu, J. Yu, D. Zhang, J.X. Zheng, V.C. Li, Effect of morphological parameters of natural sand on mechanical properties of engineered cementitious composites, Cem Concr Compos. 100 (2019) 108–119. https://doi.org/10.1016/j.cemconcomp.2019.04.007.

[43] J. Li, E.H. Yang, Macroscopic and microstructural properties of engineered cementitious composites incorporating recycled concrete fines, Cem Concr Compos. 78 (2017) 33–42. https://doi.org/10.1016/j.cemconcomp.2016.12.013.

[44] American Foundry Society, Industry Practices Regarding the Disposal and Beneficial Reuse of Foundry Sand, American Foundry Society. (2007).

[45] United States Environmental Protection Agency, Beneficial Uses of Spent Foundry Sands, Https://Www.Epa.Gov/Smm/Beneficial-Uses-Spent-Foundry-Sands. (2007).

[46] E. Yang, V.C. Li, A Micromechanical model for fiber cement optimization and component tailoring, 10th Int. Inorganic-Bonded Fiber Compos. Conf. . (2006).

[47] B. Felekoglu, K. Tosun-Felekoglu, R. Ranade, Q. Zhang, V.C. Li, Influence of matrix flowability, fiber mixing procedure, and curing conditions on the mechanical performance of HTPP-ECC, Compos B Eng. 60 (2014) 359–370. https://doi.org/10.1016/j.compositesb.2013.12.076.

[48] M. Singh, B. Saini, H.D. Chalak, Appraisal of hybrid fiber reinforced engineered cementitious composite, in: International Conference on Civil, Structural and

Transportation Engineering, Avestia Publishing, 2019. https://doi.org/10.11159/iccste19.192.

[49] J. Yu, J. Yao, X. Lin, H. Li, J.Y.K. Lam, C.K.Y. Leung, I.M.L. Sham, K. Shih, Tensile performance of sustainable Strain-Hardening Cementitious Composites with hybrid PVA and recycled PET fibers, Cem Concr Res. 107 (2018) 110–123. https://doi.org/10.1016/j.cemconres.2018.02.013.

[50] M. Ohno, V.C. Li, An integrated design method of Engineered Geopolymer Composite, Cem Concr Compos. 88 (2018) 73–85. https://doi.org/10.1016/j.cemconcomp.2018.02.001.

[51] H. Rashidian-Dezfouli, K. Afshinnia, P.R. Rangaraju, Efficiency of Ground Glass Fiber as a cementitious material, in mitigation of alkali-silica reaction of glass aggregates in mortars and concrete, Journal of Building Engineering. 15 (2018) 171–180. https://doi.org/10.1016/j.jobe.2017.11.018.

[52] Y. Ji, C. Liu, Z. Ding, Research and Analysis on Present Situation of Desert Sand Concrete, E3S Web of Conferences. 271 (2021) 3–6. https://doi.org/10.1051/e3sconf/202127102004.

Chapter 2. Carbonation Curing

In this chapter, the impact of carbonation curing on ECC is presented, including mechanical properties, CO_2 and costs evaluations, and the demonstration of field-scale application. The embodied carbon footprint is also quantified.

2.1. Introduction

As Civil infrastructure has a significant impact on environmental sustainability due to the CO_2 emissions from the concrete industry. One of its primary components, Portland cement, accounts for 8% of anthropogenic CO_2 emissions through its production [1–3]. Apart from embodied carbon, repeated repairs of civil infrastructure over its lifetime also contribute to significant operational carbon. Mitigating CO_2 emissions has been recognized by the U.S. National Academy of Engineering as one of the most important challenges for our society during the next century. To support the lowering of carbon footprint of the built environment, it is necessary to address both emissions associated with the material production phase and that associated with the structural product use phase.

ECC has high tensile ductility (nearly 500 times compared to that of normal concrete) and autogenous crack width control [4,5] which lends itself to reducing operational carbon and energy footprints via enhanced durability. However, the high cement content, and fibers usage for most ECC compositions lead to high embodied carbon compared to normal concrete [6,7]. One recent approach to address this concern is carbon sequestration by carbonation curing [8].

Carbonation curing is one of the methods for carbon sequestration in the precast industry. At the early-stage hydration process, CO_2 reacts with Portland cement and its hydration products to form calcium carbonate ($CaCO_3$). Carbon sequestrated in ECC by carbonation curing can convert CO_2 to $CaCO_3$ and lower the CO_2 footprint [8]. Meanwhile, carbonation curing can also improve the ultimate tensile and compressive strength at early ages due to the accelerated cement reaction [8]. Carbonation curing leads to a denser microstructure due to $CaCO_3$ precipitation [9,10], which is proved to enhance the material durability in various environments, such as during sulfate and acid attack, freeze-thaw deterioration, and chloride permeation [11–14].

Transportation infrastructure, such as pavement, prestressed railway ties, and bridge deck slabs, are subjected to cyclic loads and prone to fatigue damage. The flexural fatigue strength and fatigue life are among the most important criteria for structural design and service life predications to avoid repeated maintenance [15,16]. If the fatigue behavior is not properly considered, fatigue failure may be accelerated by concrete cracking and reinforcement failure [17]. Consequently, the structural stiffness would decrease, eventually leading to reduced load carrying capacity and shortened service life.

Fatigue damage in traditional concrete occurs in three phases [18,19]. In the first phase, micro-cracks initiate due to dimensional change effects (shrinkage, thermal, freeze-thaw) and/or chemical effects (sulphate attack, alkali silicate reactions) in the concrete. Then, the propagation of a localized macro-crack continues slowly and gradually under load cycles. Finally, structural failure occurs after the macrocrack achieves a critical length and becomes unstable. Crack control capability plays a vital role in resisting this process of fatigue failure. In recent research, fiber reinforced concrete (FRC) was used to gain better fatigue performance [20–22]. With the help of fiber bridging, fatigue failure of FRC was postponed by slowing down the crack propagation. Nevertheless, the tension-softening behavior of FRC [23] leads to a single crack failure: a crack initiation at mid-span, followed by propagation with increasing load cycles and eventually localizing into a final fracture failure. The tension-softening behavior of FRC limits its flexural fatigue performance. Unlike FRC, ECC exhibits significant deflection-hardening behavior with multiple microcracks on the tensile side of the beam. Compared to FRC, ECC has a longer fatigue life under the same flexural stress [24–27]. The multiple microcracks in ECC delay fracture localization, making it a desirable material for enhancing fatigue life of structural members subjected to repeated loading.

Despite the presence of a body of literature on the fatigue performance of water or air cured ECC, the fatigue performance of carbonation-cured ECC has not been studied. The objective of this research is to clarify the flexural fatigue behavior of ECC after carbonation curing.

To identify the impact of carbonation curing on ECC, two curing conditions were considered (carbonation curing and air curing). The failure mechanism and multiple cracking behaviors of the carbonation-cured and air cured ECC were investigated. Sixty ECC beam specimens were prepared and tested under four-point static and fatigue bending load for midspan deflection evolution and fatigue stress-life relationship. Single fiber pullout tests were also

conducted to determine the interfacial bond between fibers and cementitious matrix as affected by carbonation curing. The fiber bridging degradation was evaluated by optical microscopy. By evaluating the flexural fatigue behavior of CO_2-cured ECC, this research experimentally validates the ability to synergistically reduce embodied and operational carbon through carbonation curing of engineered cementitious composites, thus contributes to the sustainability of civil infrastructure.

2.2. Experimental program

2.2.1 Materials and mix proportions

A typical M45 ECC mix with a fly ash to cement ratio of 1.2 [28] was used. The detailed mix proportion is given in Table 2-1. The materials for this mixture include type I ordinary Portland cement (OPC, from Lafarge Holcim Cement Co., MI, USA) conforming to ASTM C150 [29], Class F fly ash (FA), F-75 whole-grain silica sand (from U.S. Silica Holdings Inc., TX, USA), high-range water reducer (HRWR, ADVA® 198, from GCP Applied Technologies), and polyvinyl alcohol (PVA) fibers (from Kuraray Co.) with 39μm diameter and 8mm length. The dimensional and mechanical characteristics of PVA fibers are listed in Table 2-2.

Table 2-1 Mix proportion of ECC (kg/m^3) [28]. [a] Volume fraction.

Mixture	OPC	FA	Sand	Water	HRWR	PVA[a]
M45	600	720	480	348	10	2%

Table 2-2 Properties of Fiber.

Fiber type	Length (mm)	Diameter (μm)	Fiber aspect ratio	Tensile strength (MPa)	Young's modulus (GPa)	Density (g/cm^3)
Polyvinyl alcohol fibers (PVA)	8	39	205	1600	42.8	1.3

2.2.2 Sample preparation and carbonation curing process

Static, flexural fatigue experiments, uniaxial tension tests and single fiber pull-out tests were conducted. Beam specimens for static and flexural fatigue tests were fabricated with a length of 304.8 mm, a width of 76.2 mm, and a depth of 38.1 mm. 27 beam specimens for carbonation-cured ECC and 33 beam specimens for air-cured ECC were prepared. Additionally, five single fiber pull-out specimens for each carbonation-cured and air-cured ECC were fabricated. All mold cast samples were de-molded after 18 hours. Then, carbonation-cured ECC specimens were fan dried in air for 4 hours and cured in CO_2 for 24 hours. The CO_2 gas pressure was kept at 5 bar [8]. The age for all specimens at testing was 28 days. In addition to beam specimens, dogbone shaped specimens were made to verify the tensile ductility for both air-cured and carbonation-cured ECC. Three 50x50x50 mm^3 cube and dogbone shaped specimens were made to evaluate the CO_2 uptake of carbonation-cured M45 ECC. The geometry of the beam and dogbone specimens is shown in Figure 2-1, which is general dimensions for flexural and tensile tests.

2.2.3 Test methods

In this study, a Material Testing Systems (MTS) loading frame with a 100 kN capacity was used. Uniaxial tension tests were conducted on the dogbone-shaped specimens with displacement control at a rate of 0.5 mm/min. The deformation was measured by two linear variable displacement transducers (LVDT) with a gauge length of 80 mm [30]. Four-point flexural static tests were also conducted under displacement control to determine the first crack flexural strength, maximum flexural strength, and load-deflection curve for both carbonation-cured and air-cured ECC. The first cracking is observed via the load data and deflection data. The first load drop with deformation is determined as the occurrence of first crack. All specimens had a span length (L) of 254 mm with two-point loads at one half of the span as shown in Figure 2-2.

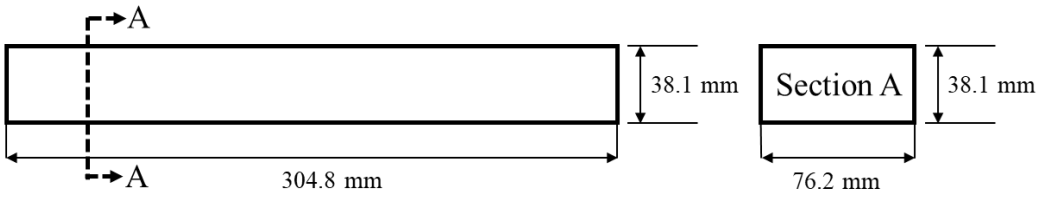

(a)

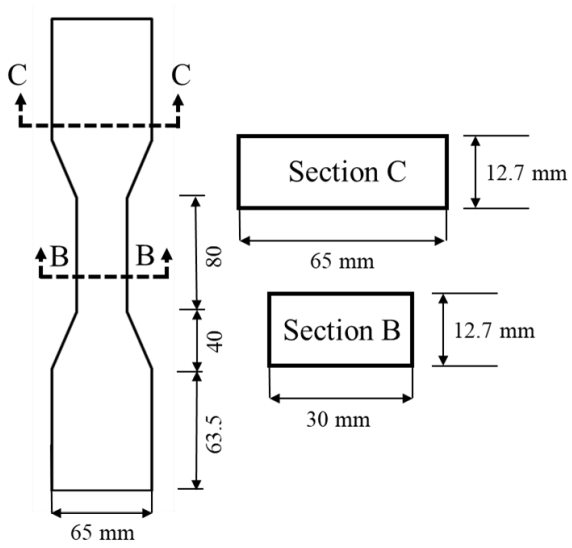

(b)

Figure 2-1. Dimensions of the (a) beam specimen for flexural static/fatigue test, (b) dogbone-shaped specimen for tension and CO_2 uptake tests.

The static flexural strength of each kind of ECC was determined by averaging three test results of specimens, after which, maximum fatigue load (P_{max}) can be determined. Four-point flexural fatigue tests were conducted under load control. By using the maximum flexural strength gained from the static test, the applied load P for 6 different stress levels (S) can then be determined: S = 0.85, 0.8, 0.7, 0.6, 0.5, and 0.45.

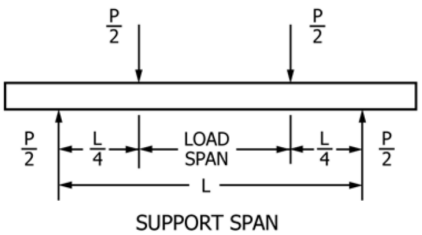

Figure 2-2 Loading configuration for four-point bending test.

2.2.3.1 Static test

Four-point static tests were conducted under displacement control. The detailed experimental system is shown in Figure 2-3. Optotrak Certus from NDI was installed to measure the midspan deflection of specimens. Each static flexural test specimen was attached with four Optotrak markers via hot melt glue. During the experiment, the Optotrak camera captured the displacement of each marker at 40 frames per second (40 Hz). The midspan deflection and load-deflection curve can then be calculated with the load gained by the MTS according to following equation:

$$\Delta_{midspan,Z} = 0.5(\Delta_{A,Z} + \Delta_{D,Z}) - 0.5(\Delta_{B,Z} + \Delta_{C,Z}) \quad (2\text{-}1)$$

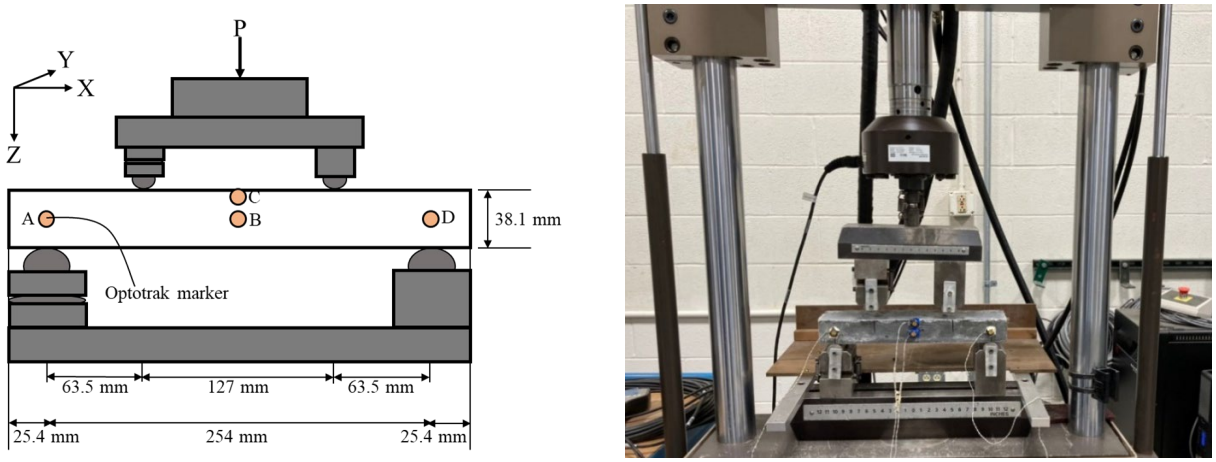

Figure 2-3 Experiment system for static flexural bending test.

2.2.3.2 Fatigue test

Flexural fatigue tests were carried out using sinusoidal cyclic load with a frequency of 8Hz [25]. The maximum (P_{max}) to minimum fatigue load (P_{min}) ratio was kept at 0.1 for all fatigue specimens (P_{max}/P_{min} = 0.1). The fatigue test began with a ramp up force to P_{max} at a rate of 100N/sec [31] followed by the sinusoidal waveform fatigue loading. The load pattern for the fatigue tests is shown in Figure 2-4. The fatigue tests stopped either when the specimen failed with a load-drop or after it reached three million cycles of fatigue life. The Optotrak Certus from NDI

was also used to measure the midspan deflection of specimens. An optical microscope was used to observe the residual crack widths, crack numbers, and fiber deteriorations after fatigue tests.

To obtain the full fatigue stress level (S) – fatigue life (N) relationship, six stress levels (S = 0.45, 0.5, 0.6, 0.7, 0.8 and 0.85) were evaluated up to 3 million loading cycles. The fatigue stress level is defined as the ratio between the maximum fatigue stress from load (P_{max}) and maximum static flexural strength from static tests. For example, if the static flexural strength is 10 MPa, the Pmax that generates 8 MPa flexural stress would be used in fatigue tests when the stress level *S* is 0.8. The stress levels and the number of specimens for each stress level are listed in Table 2-3.

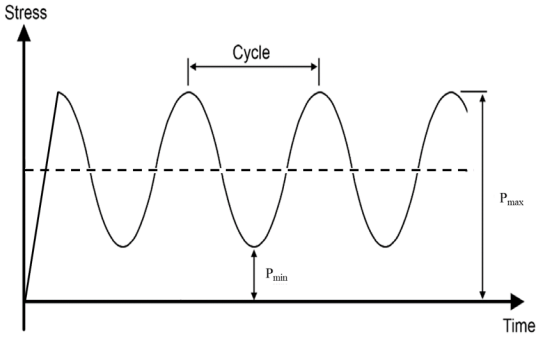

Figure 2-4 Load pattern for flexural fatigue test.

Table 2-3 Number of specimens at each fatigue stress level.

Material	Stress level (%)	85	80	70	60	50	45
Carbonation-cured ECC (M45)	Number of specimens	3	3	3	3	3	-
Air-cured ECC (M45)		3	3	3	3	3	3

2.2.3.3 Single fiber pull-out test

Figure 2-5(a) shows how the single fiber pull-out test specimens were made. The small pull-out specimens for both carbonation-cured and air-cured ECC were sawn out from thin cast

plates along the cutting line shown in Figure 2-5(a) [32,33] with around 1.5 mm embedded length. The experimental system is shown in Figure 2-5(a). An Instron Model 8000 test system was used in the pull-out tests. PVA fibers were glued on the steel plate and connected to actuator. Pull-out curves can be obtained after the fibers pull out. Furthermore, the chemical debonding energy, chemical bond G_d, can be calculated according to the single fiber pull-out curves as shown in Equation (2-2). Frictional bond strength, τ_0, can also be determined [32,34] by Equation (2-3).

$$G_d = \frac{2(P_a - P_b)^2}{\pi^2 E_f d_f^3} \tag{2-2}$$

$$\tau_0 = \frac{P_b}{\pi d_f l_e} \tag{2-3}$$

where P_a and P_b are the fiber pullout load P before and after the sudden drop for the fiber debonding, E_f, d_f, and l_e is the Yong's modulus, fiber diameter, and fiber embedded length for PVA fibers.

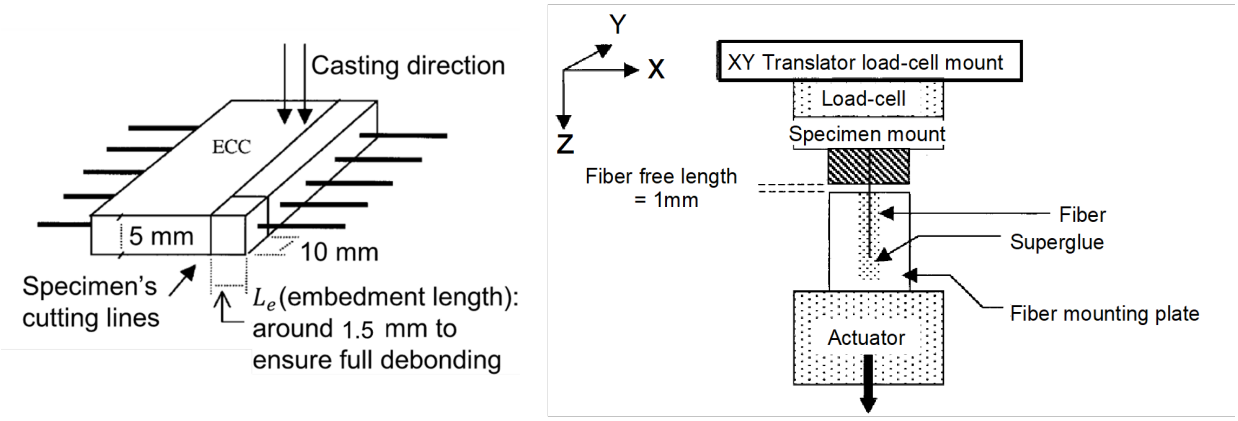

(a) (b)

Figure 2-5 (a) Single fiber pullout specimens [32], (b) single fiber pullout test system [32].

2.3. Results and discussion

2.3.1 CO_2 uptake

Table 2-4 provides the CO_2 carbonation efficiency of ECC specimens following the carbonation curing process described in section 2.2.2 where CO_2 uptake is the mass of sequestrated CO_2 divided by the dry cement mass in the sample using mass gain method [8]. The beam, cube, and dogbone specimens achieved 14.5%, 21.2%, and 29.6% CO_2 uptake by cement mass with surface/volume ratio of 8.5%, 12%, and 20.6%, respectively, after a 24-hour carbonation cure. Increasing the surface/volume ratio of specimens led to a slight increase in the amount of CO_2 sequestered, as the carbonation process is governed by the diffusion of CO_2 gas through the specimen surface into the cement matrix [35,36]. The carbonation depth of the ECC beam specimen was 11 mm within 24 hours as shown in Figure 2-6. These results indicate that ECC has the potential to sequester CO_2 via carbonation curing. The concern for steel reinforcement corrosion in normal reinforced concrete elements associated with a reduction in pore water pH due to carbonation [37–39] is less of a concern for ECC structural elements since ECC is self-reinforced with microfibers and has lower dependence on steel reinforcement. However, the carbonation of steel reinforcement ECC still requires further research. It should also be noted that the center of the beam specimens was not carbonated.

Table 2-4 CO_2 uptake of carbonation-cured M45 ECC specimens.

Specimen Type	Beam	Cube	Dogbone
Average CO_2 uptake	14.5%	21.2%	29.6%

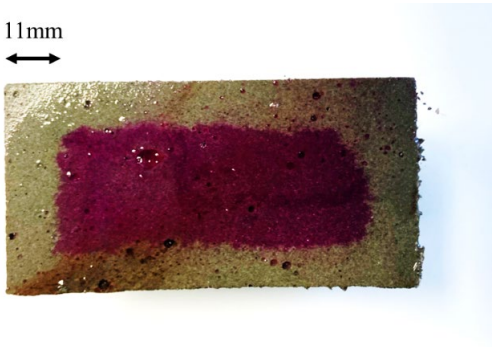

Figure 2-6 Carbonation depth of ECC beam specimen.

2.3.2 Static test results

Figure 2-7 depicts the typical tensile stress-strain curves of carbonation-cured and air-cured ECC. The tensile properties are summarized in Table 2-5, where the peak stress is defined as ultimate tensile strength and the corresponding strain is defined as tensile strain capacity. Carbonation curing increased the first crack strength and ultimate tensile strength from 4.63 to 5.04 MPa (9% increase) and 6.47 to 7.94 MPa (23% increase). Meanwhile, the tensile ductility for carbonation-cured ECC reached 4.46%, which was comparable to those of air-cured M45 ECC specimens in the literature [28].

The first cracking strength σ_{fc} and ultimate flexural strength σ_{fu} of carbonation-cured and air-cured ECC beams under static loading are summarized in Table 2-6. The static flexural strengths were calculated using Equation (2-4), assuming the loading span is half the support span:

$$\sigma_f = \frac{3PL}{4bd^2} \tag{2-4}$$

where b and d denote the width and depth of the beam, and L is the support span. σ_{fc} is calculated based on the load level causing the first crack $P=P_{fc}$, while σ_{fu} is calculated based on the maximum load level $P=P_{max}$. After carbonation, the average σ_{fu} of ECC increased from 10.01 to 13.18 MPa (32% increase), exceeding the results reported in previous studies using the same mix proportions [25,27]. Similarly, the σ_{fc} of carbonation-cured ECC increased from 5.66 to 7.17 MPa (27% increase). The average σ_{fu} was then used to calculate the maximum fatigue stress (σ_{max}) for each stress level, demonstrating that carbonation-cured ECC had a greater σ_{max} than air-cured ECC at the same stress level.

The monotonic flexural behavior for both specimen groups is shown in Figure 2-8 in terms of the flexural stress – midspan displacement diagram. The midspan deflection was averaged from the Optotrak markers following Equation (2-1). The results suggested that the deformation capacity of carbonation-cured ECC was comparable to that of air-cured ECC. After the carbonation-cure, the average midspan deflection of ECC increased from 1.82 to 3.07 mm (69% increase). Unlike traditional concrete where long term carbonation could be harmful due to embrittlement, the early age carbonation process used in the present study does not appear to negatively impact the high tensile ductility of ECC at the age of 28 days, while long-term characteristics may need further research. Both the carbonation-cured and air-cured ECC showed

high deformation capacities under flexural load due to multiple cracking and followed the same failure mechanism. In the beginning, the first crack initiated after the load exceeded first crack strength (stage A in Figure 2-8). Multiple cracks then formed on the tensile surface of the specimen. Deflection-hardening behavior for both ECCs was clearly demonstrated as the flexural load continued increasing (stage B in Figure 2-8) without load drop as is typically the case for FRC beams. Finally, one of the multiple cracks localized and propagated. This was followed by a softening stage when the loading was stopped (at 50-60% of maximum load, stage C in Figure 2-8). Carbonation-cured ECC is thus anticipated to have better fatigue performance due to the higher flexural first crack strength, ultimate flexural strength, and midspan deflection capacity compared with air-cured ECC.

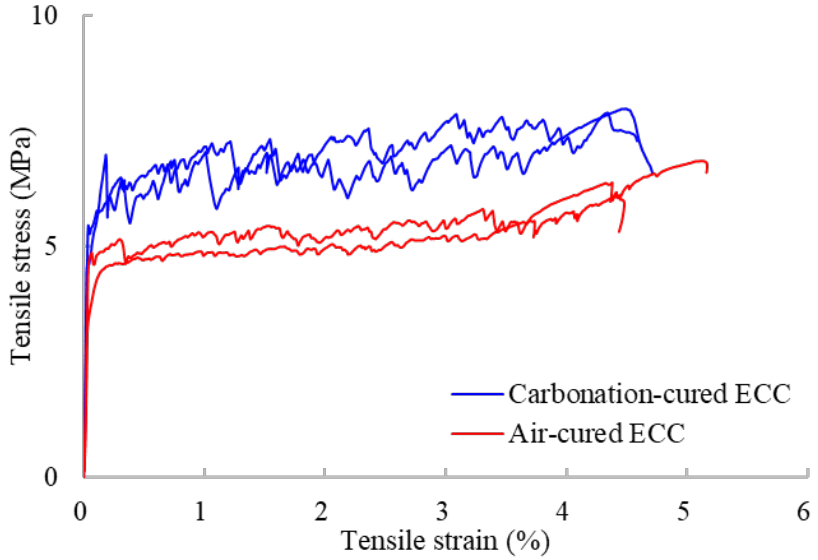

Figure 2-7 Tensile stress-strain relationship.

Table 2-5 Tensile properties for carbonation-cured and air-cured ECC (M45) at 28 days.

Material	First crack strength (MPa)	Ultimate tensile strength (MPa)	Tensile strain capacity (%)
Carbonation-cured ECC	5.04 ± 0.41	7.94 ± 0.05	4.46 ± 0.07
Air-cured ECC	4.63 ± 0.02	6.47 ± 0.38	4.77 ± 0.40

Table 2-6 Results of the static flexural test.

Material	No.	First crack strength σ_{fc} (MPa)	Average first crack strength (MPa)	Ultimate flexural strength σ_{fu} (MPa)	Average flexural strength (MPa)	Midspan deflection (mm) at σ_{fu}	Average midspan deflection (mm) at σ_{fu}
Carbonation-cured ECC	1	7.60	7.17 ± 0.31	13.52	13.18 ± 0.49	3.11	3.07 ± 0.22
	2	6.97		12.49		2.78	
	3	6.93		13.52		3.31	
Air-cured ECC	1	5.66	5.66 ± 0.40	10.32	10.01 ± 0.45	1.87	1.82 ± 0.24
	2	5.17		9.38		1.51	
	3	6.14		10.33		2.08	

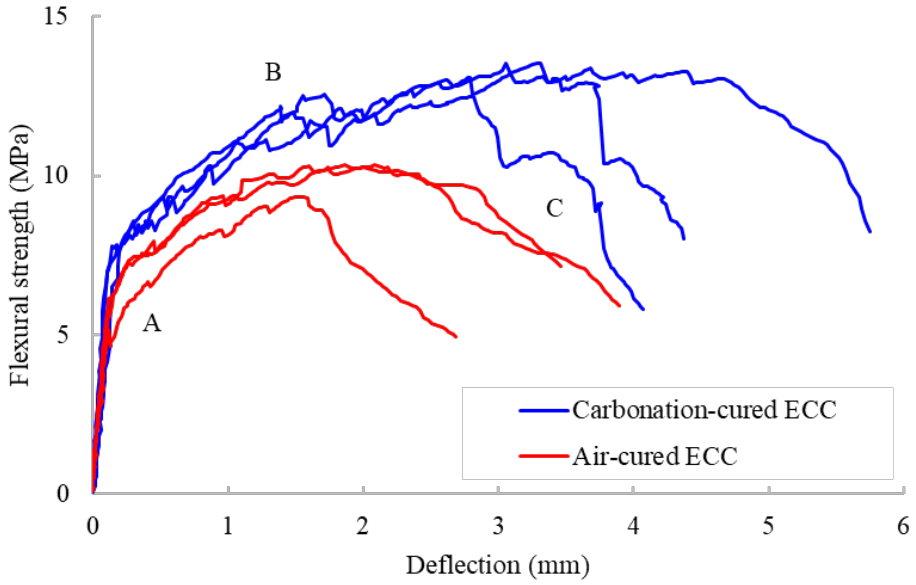

Figure 2-8 Results of static flexural test.

2.3.3 Fatigue test results

2.3.3.1 Fatigue stress-life relationships and fatigue life

The fatigue life (i.e., maximum loading cycle) is shown as a function of stress level (σ_{max} /σ_{fu}) in Figure 2-9 and of flexural stress (MPa) in Figure 2-10. The arrows in the figures indicate the termination of the fatigue loading program (i.e., 3 million cycles) when all testing groups were stopped intentionally. As shown in Figure 2-9, the fatigue performance for ECC specimens in this study was comparable to those of ECC specimens in the literature [25,40]. These PVA-ECC in Figure 2-9 showed the typical bilinear S-N relation on a semi-logarithmic scale, similar to metallic materials [41]. ECC retained this bilinear relation after carbonation curing. This contrasts with other cementitious composites (e.g., polymer cement mortar (PCM)) that usually show a linear S-N relation on a semi-logarithmic scale [27]. Compared to non-carbonated ECC, carbonation-cured ECC showed similar fatigue life performance when considered at the same stress level (% of ultimate strength) but showed an improved fatigue life performance at the same flexural stress (MPa), due to the higher ultimate flexural strength after carbonation.

The results suggest that carbonation curing had a minimal impact on ECC's fatigue behavior at low stress (< 8 MPa), but significantly enhanced the fatigue life when subjected to higher flexural stress (see Figure 2-10). Also, carbonation-cured ECC passed 3 million life cycles at higher fatigue stress than the air-cured ECC. This is attributed to the higher first cracking strength (7.17 MPa) for carbonation-cured ECC compared to that of the air-cured reference (5.66 MPa). As shown in Figure 2-10, when fatigue stress was less than 7.17 MPa, below the first crack strength of the carbonation-cured ECC, almost all carbonation-cured specimens reached 3 million cycles since there was no crack initialized under the fatigue load. While 7.17 MPa exceeds the first cracking strength of the air-cured ECC, cracks initiated at an early stage and localized before 3 million cycles. These data demonstrate that ECC experiences a longer fatigue life when the fatigue load is kept below the first cracking strength, and the enhanced first-cracking strength by carbonation curing is conducive to the material's fatigue resistance.

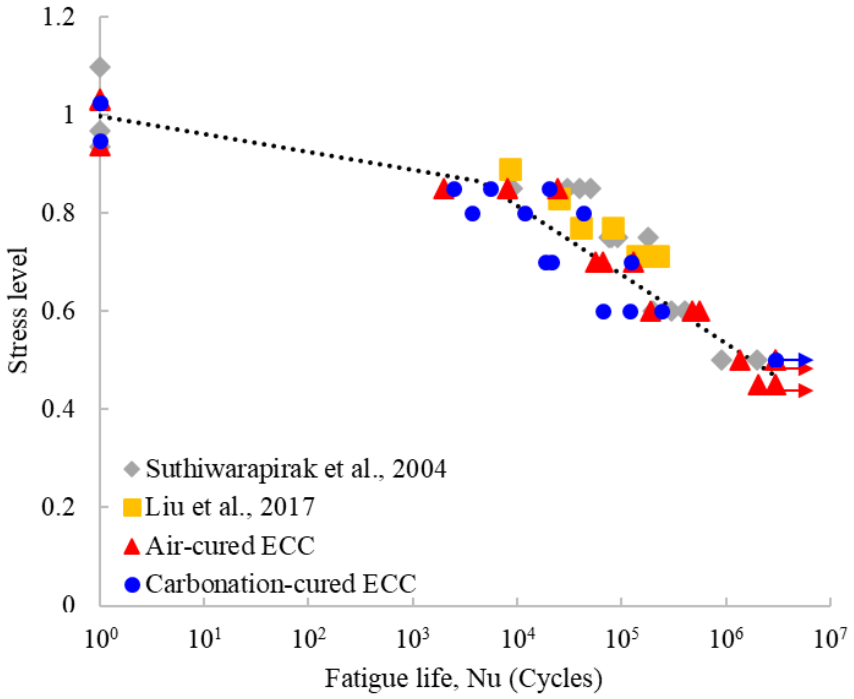

Figure 2-9 Fatigue stress level-life relationships for air-cured ECC.

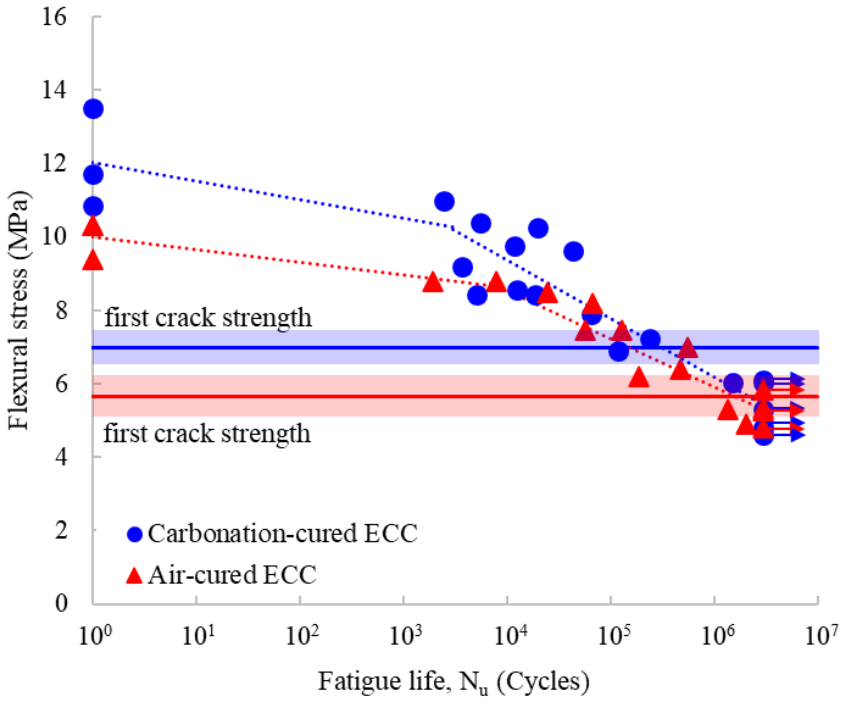

Figure 2-10 Fatigue stress-life relationships. Shaded areas represent the range of experimental variability.

2.3.3.2 Midspan deflection evolution

Figure 2-11 shows the evolution of ECC's midspan deflection as a function of stress for specimens with different testing cycle/maximum cycles (N/N_u = 0.98, 0.85, 0.65, 0.50, 0.35, and 0.05). All ECC specimens have high R-squared values for the linear regressions shown in Figure 2-11 (R^2 over 0.9), which indicates good consistency of the linear relationships. The results illustrate that air-cured ECC developed a higher midspan deflection and more damage compared to the carbonation-cured ECC under the same fatigue stress, during the fatigue loading. The evolution of midspan deflection depended on the fatigue stress. As shown in Figure 2-11 (a) to (f), midspan deflection for low stress (i.e., 5 MPa) remained equivalent, midspan deflection was 0.1 mm for carbonation-cured ECC and 0.5 mm for air-cured ECC, while midspan deflection increased by over 5 times for carbonation-cured ECC and 2 times for air-cured ECC from 0.05 N/Nu to 0.98 N/Nu when the fatigue stress increased. The midspan deflection was found to decrease after carbonation curing under the same stress, with all N/N_u, indicating an enhanced structural stiffness of the ECC due to carbonation curing.

Figure 2-12(a) shows the typical fatigue failure evolution for both carbonation-cured and air-cured ECC when fatigue stress is above the first crack strength of the specimen. As discussed previously, the failure progress of concrete can be divided into three phases: (1) crack initiation; (2) slow, steady crack propagation; (3) crack localization and widening, which leads to final fatigue failure. The first crack flexural strength of carbonation-cured ECC increased from 5.66 to 7.17 MPa (27% increase), which slightly delays the first phase of fatigue failure as shown in Figure 2-12(a). Moreover, carbonation curing increased the fatigue life of ECC in the second phase drastically (i.e., fatigue life increases from 6801, 35000, and 20241 cycles [25,40] to nearly 220000 cycles under similar fatigue stress). Samples from both Liu et al. [40] and Suthiwarapirak et al. [25] also showed similar typical 3 phases fatigue failure evolution for their air-cured PVA ECC with ceased new cracks formations, while existing cracks propagated gradually in second phase. The reason for improved second phase fatigue life of carbonation-cured ECC is that carbonation curing improves the crack width control of ECC, thus slowing down the evolution of cracks and extending the fatigue cycles in the carbonation-cured ECC (Figure 2-11). The increased duration of the first and second phases finally result in a longer fatigue life for the carbonation-cured ECC at a high fatigue stress. However, when fatigue stress is below the first crack strength, the fatigue failure evolution is different as shown in Figure 2-12(b). The fatigue cycles for both ECC remain

the same during the first phase since there is no crack initiation and both ECC passed the 3 million cycles without failure. Figure 2-12(b) also indicates that carbonation curing can enhance the material stiffness and decrease the midspan deflection led by the fatigue loading.

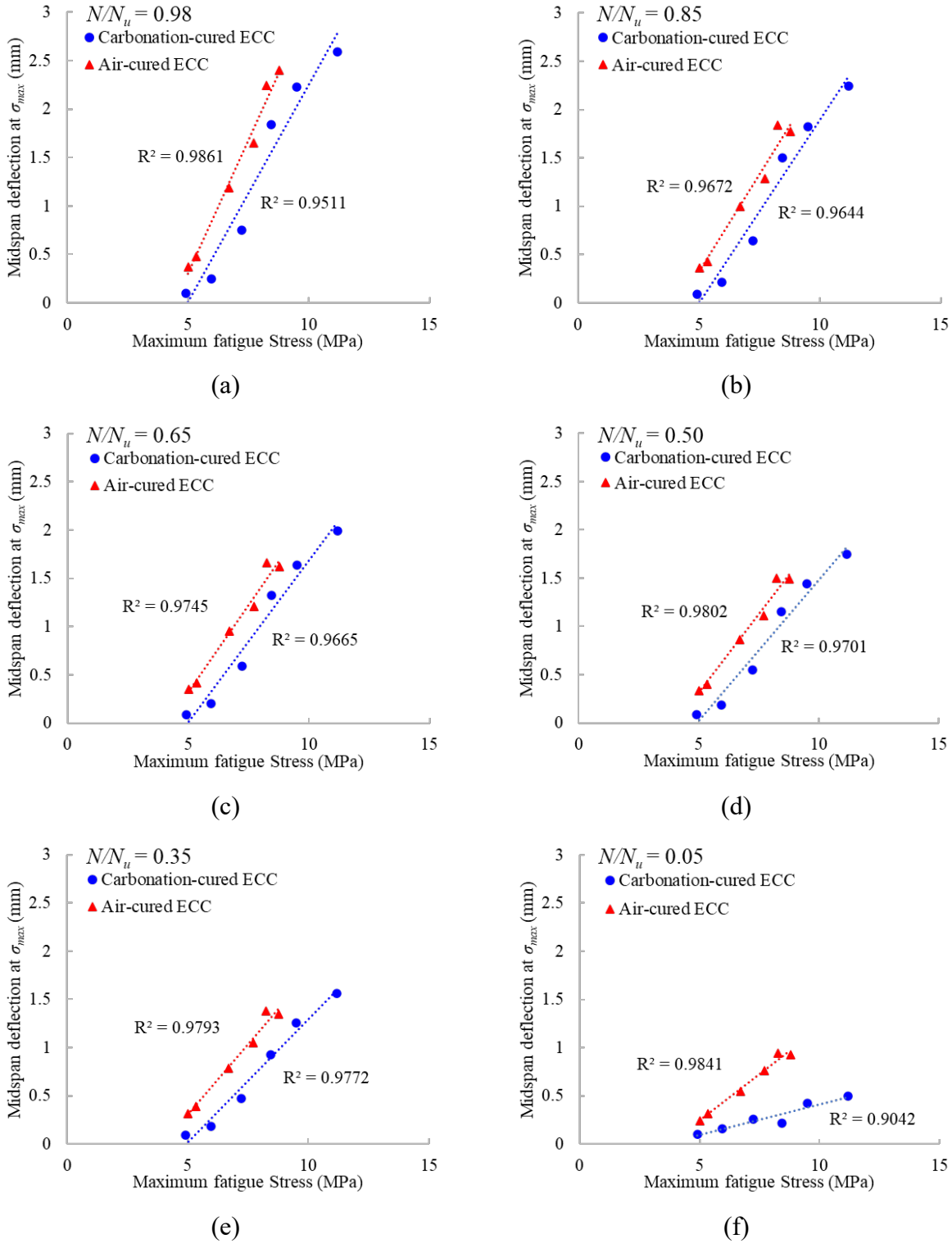

Figure 2-11 Midspan deflection of carbonation-cured and air-cured M45 under different testing cycle/maximum cycle (N/N_u): (a) N/N_u = 0.95, (b) N/N_u = 0.80, (c) N/N_u = 0.65, (d) N/N_u = 0.50, (e) N/N_u = 0.35, (f) N/N_u = 0.05

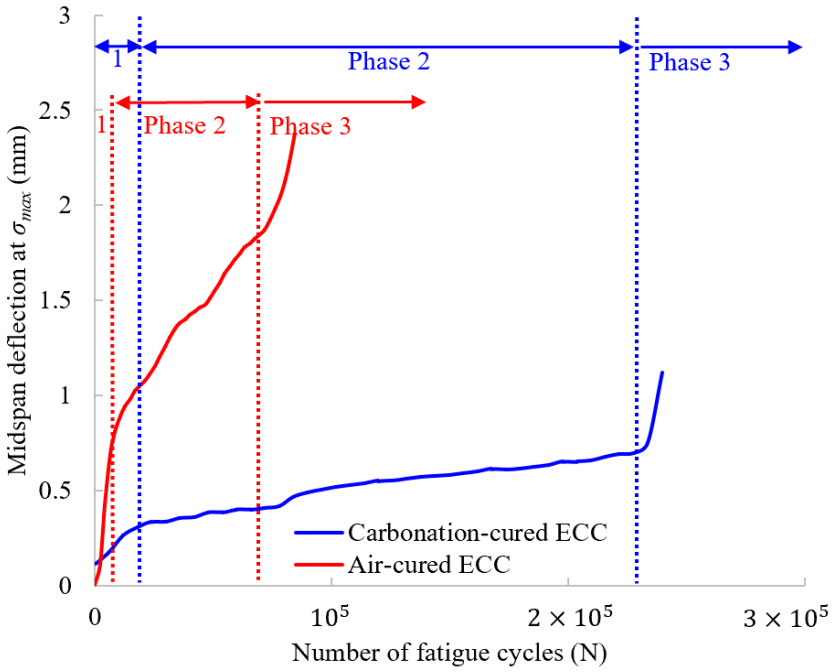

(a)

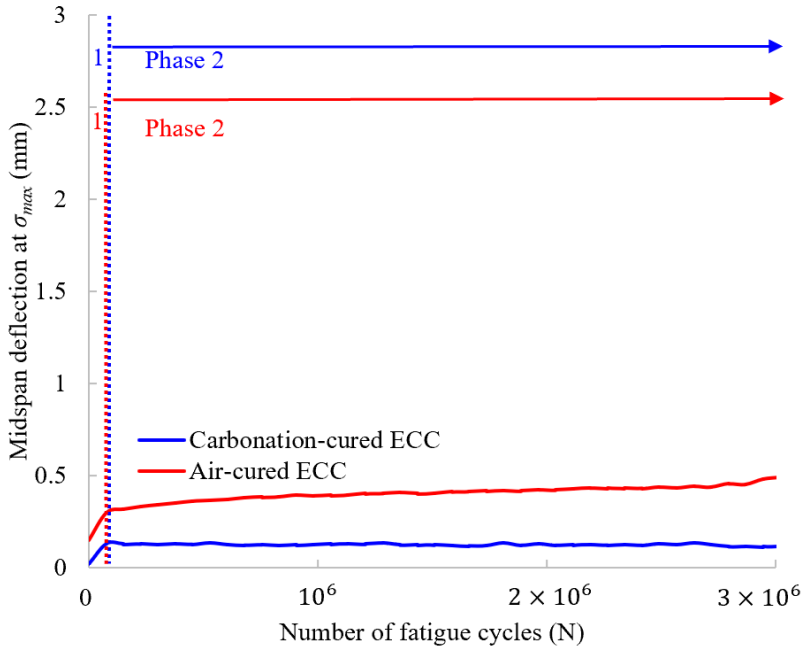

(b)

Figure 2-12 Typical fatigue failure evolution for (a) carbonation-cured and air-cured ECC above their first crack strength, (b) carbonation-cured and air-cured ECC below their first crack strength.

2.3.3.3 Crack patterns and crack width distribution

Figure 2-13 shows the crack patterns on the bottom surface of the ECC beam specimens. Typical specimens were selected to represent the crack patterns for fatigue tests at 80% and 60% stress level. The load span, with a length of 127 mm, is also shown in Figure 2-13. The results indicate that both carbonation-cured and air-cured ECC exhibited multiple cracking behavior under fatigue loading and that the cracking patterns depended on the level of fatigue stress. That is to say, an increasing amount of cracks was observed when the stress level was high (S = 0.8 as shown in Figure 2-13 (a) and Figure 2-13 (b)). In Figure 2-13 (c) and Figure 2-13 (d), at a relatively lower stress level (0.6), less than 3 cracks were formed, indicating that the ECC behaves more similar to FRC with only a single crack under low fatigue stress.

To understand the crack pattern under various fatigue loads, crack widths were measured at the bottom side of all specimens. As shown in Figure 2-14, the carbonation-cured ECC exhibited a maximum crack opening of 76 μm, whereas the air-cured ECC showed a broad range of crack widths up to 148 μm. The average crack width decreased from 62 μm to 30 μm after carbonation curing. Figure 2-15 shows the typical images of the post-fatigue cracks for carbonation-cured and air-cured specimens. The results show that carbonation curing strengthened ECC's crack width control capability under fatigue conditions.

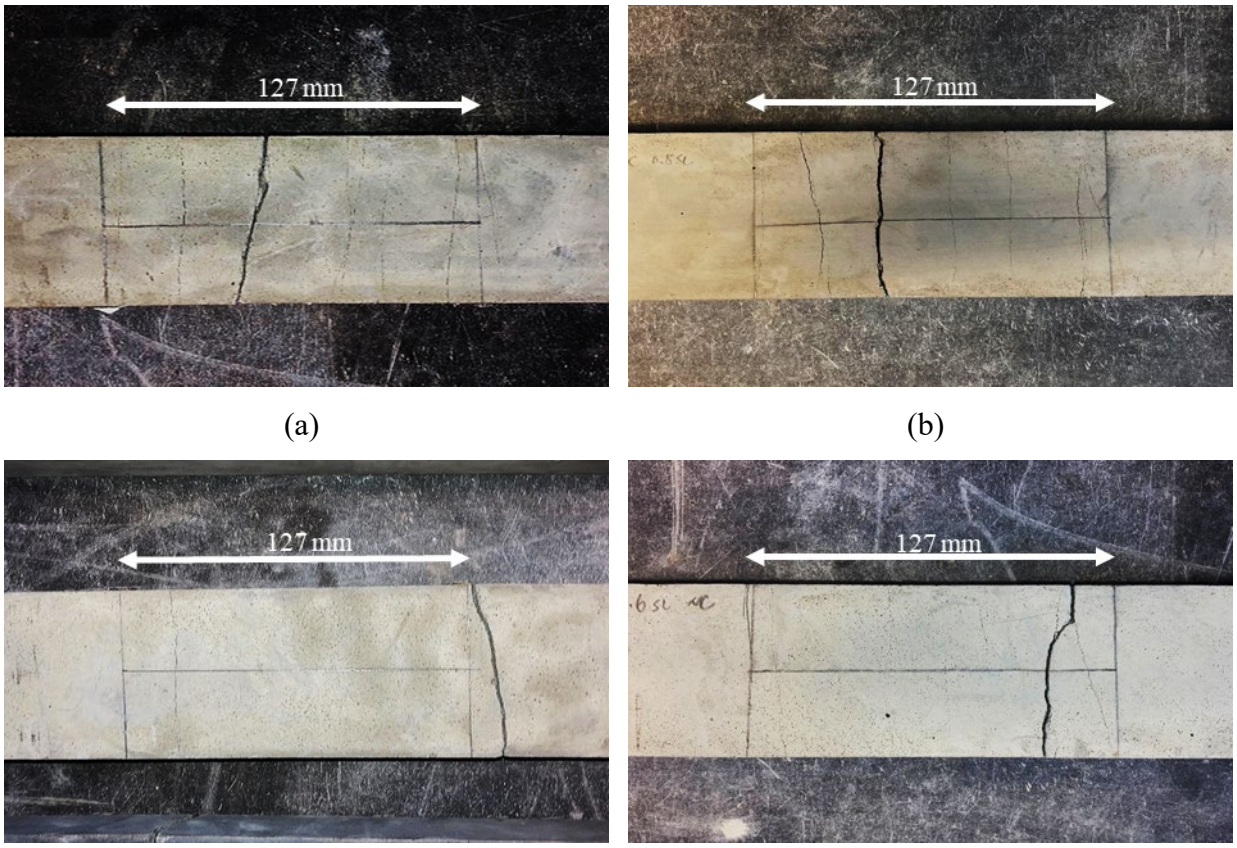

(a) (b)

(c) (d)

Figure 2-13 Post-fatigue crack patterns on the bottom surface: (a) carbonation-cured specimen at 80% stress level, (b) air-cured specimen at 80% stress level, (c) carbonation-cured specimen at 60% stress level, (d) air-cured specimen at 60% stress level.

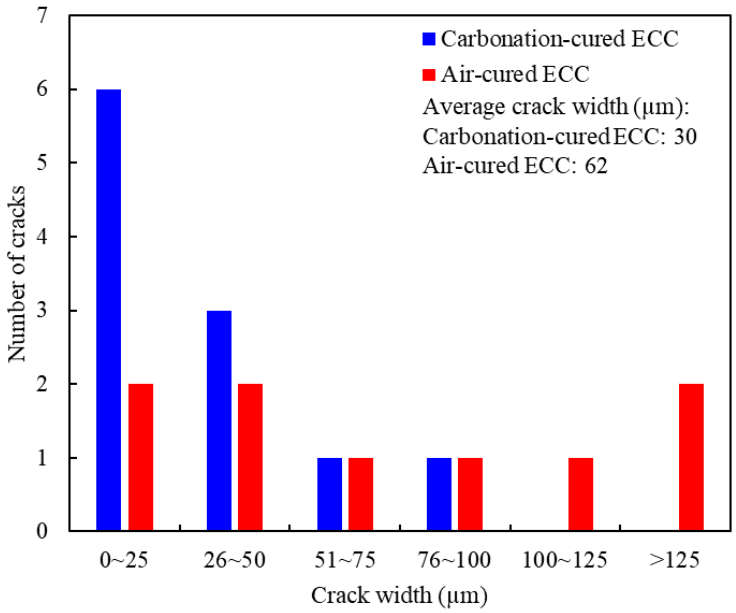

Figure 2-14 Crack width distribution for carbonation-cured and air-cured ECC under 80% stress level.

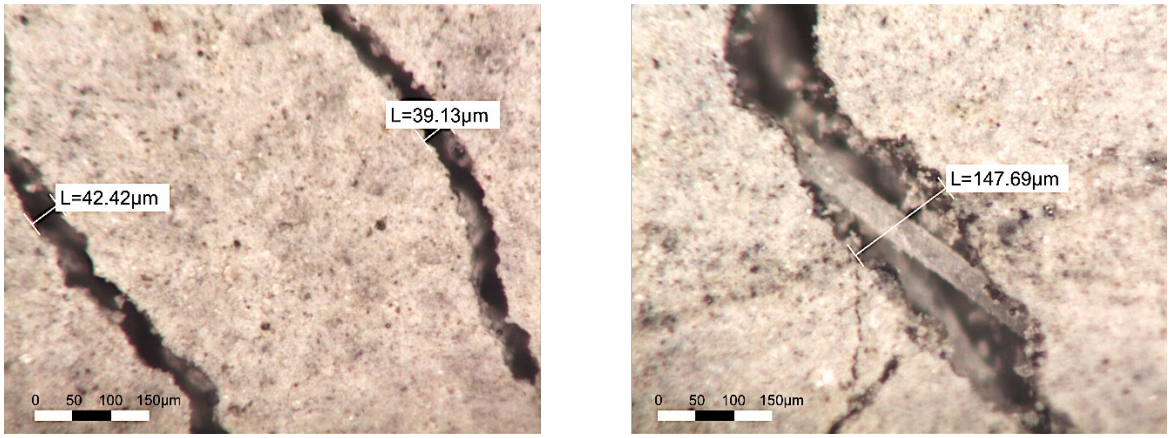

(a) (b)

Figure 2-15 Typical cracks for (a) carbonation-cured and (b) air-cured ECC.

2.3.3.4 Fiber bridging degradation (fiber rupture and pull-out)

Fiber bridging degradation promotes crack propagation and results in the failure of ECC specimens under fatigue load [42]. From a mechanics-based viewpoint, fiber bridging deterioration is related to fiber/matrix interfacial debonding and the damage and potential rupture of the fibers [25,42]. The loss of bond strength or damage at the fiber/matrix interface leads to fiber pull-out

[43]. Fiber fatigue under the cyclic fatigue loading results in fiber fracture. Thus, it is important to examine the fiber tips at the fractured cross section to determine the mechanism leading to the failure of ECC.

The failure type for both carbonation-cured and air-cured ECC fibers is shown in Figure 2-16, where PVA fiber was (a) ruptured and (b) pulled out. The bottom side of the localized fracture is shown. For each specimen, three random areas were selected and a total of 40 fibers in each section were investigated. The number of ruptured and pulled-out fibers were counted separately with the result given in Table 2-7. The results show that for both the carbonation-cured and air-cured ECC sample the dominant failure mode is fiber rupture under all loading conditions including static and fatigue loading at different stress levels. This may be the reason that both PVA ECC specimens exhibited a bilinear *S-N* curve relationship similar to that of metal since metallic materials are typically dominated by rupture failure [41].

The carbonation-cured ECC had a higher percentage of ruptured fibers compared to the air-cured reference specimen. The ratio between the number of ruptured fibers and pulled-out fibers increased by 15% after carbonation curing. This could be attributed to the increased interfacial bond between PVA fibers and the matrix after carbonation curing by depositing $CaCO_3$ along the PVA fiber/matrix interface as evidenced from backscattered electron images [8], which was verified by the single-fiber pullout test. The average values of the chemical bond G_d and the frictional bond τ_0 were calculated and reported in Table 2-8. The detailed single-fiber pullout load and displacement curve can be found in Figure 2-17. The G_d and τ_0 of the air-cured ECC were comparable with literature [32,44], while the G_d and τ_0 values of the carbonation-cured ECC increased drastically from 0.37 J/m^2 to 2.42 J/m^2 and from 1.32 MPa to 2.24 MPa, indicating a stronger resistance to fiber debonding and slippage. This confirmed the strengthening of the interfacial bond between PVA fibers and carbonation-cured ECC matrix, leading to better crack width control capability than the air-cured ECC, which further improved the fatigue performance of the carbonation-cured ECC.

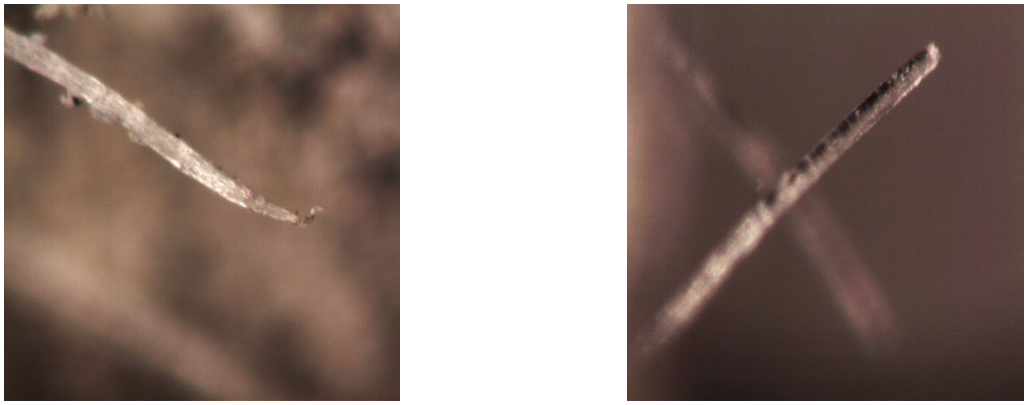

(a) (b)

Figure 2-16 Optical microscopy image for PVA fibers that was (a) ruptured, (b) pulled out from the specimens.

Table 2-7 Ratio between ruptured fibers and pulled-out fibers for carbonation-cured and air-cured ECC (% of ruptured fibers).

Material	Static	Fatigue stress level	
		0.85	0.6
Carbonation-cured ECC (M45)	30:10 (75%)	32:8 (80.0%)	31:9 (77.5%)
Air-cured ECC (M45)	24:16 (60.0%)	25:15 (62.5%)	29:11 (72.5%)

Table 2-8 PVA fiber/matrix interfacial bond for carbonation-cured and air-cured ECC (M45) at 28 days.

Material	No.	P_a (N)	P_b (N)	Average Chemical bond G_d (J/m^2)	Average Frictional bond τ_0 (MPa)
Carbonation-cured ECC (M45)	1	0.43	0.27	2.42 ± 0.75	2.24 ± 0.83
	2	0.57	0.43		
	3	0.59	0.39		
	4	0.62	0.47		
	5	1.14	0.93		
Air-cured ECC (M45)	1	0.26	0.20	0.37 ± 0.32	1.32 ± 0.64
	2	0.25	0.14		
	3	0.47	0.41		
	4	0.46	0.40		
	5	0.35	0.33		

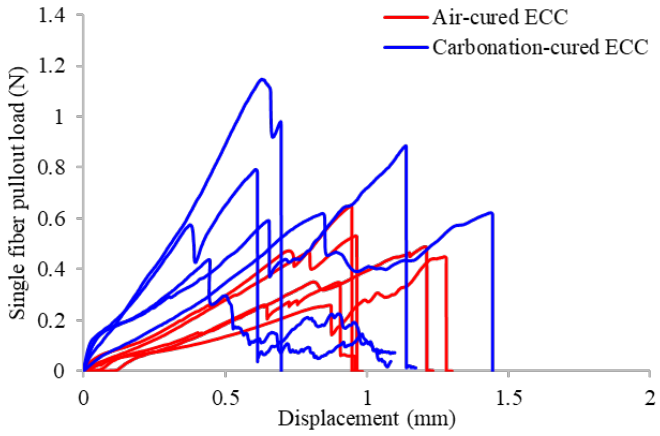

Figure 2-17 Single fiber pullout load-displacement curve for both air-cured and carbonation-cured ECC

2.4. CO_2 footprint and cost evaluation

To evaluate the CO_2 footprint and cost for the ECC after carbonation curing, the carbon emission and material cost for ingredients for ECC production are summarized in Table 2-9. The fly ash in this study was assumed to be IWMs with a zero CO_2 footprint. It should be noted that the costs were the price of each ingredient ranging from 2018 to 2020, likely to fluctuate due to inflation in the future.

Typical M45-ECC and conventional concrete were used as a benchmark to quantify the effectiveness of carbonation curing on the CO_2 emissions and costs, as shown in Figure 2-18. The result suggests that carbonation curing decreased the embodied carbon footprint of carbonation-cured M45-ECC by 22% compared to typical M45-ECC (from 606 kg CO_2/m^3 to 474 kg CO_2/m^3). However, this value is still higher than that of conventional concrete (341 kg CO_2/m^3) since the high cement and fiber usage was not reduced, indicating the incorporation of IWMs to reduce ECC's embodied carbon footprint further is necessary. More detailed contributions of embodied carbon footprint by ingredients are shown in Figure 2-19.

Table 2-9. The carbon emission and material cost for ingredients for ECC production.

Component	CO_2 emission (kg/t)	Cost (USD/t)
OPC type 1	870-940[a]	48[b]
FA	0	25.6[b]
Silica sand[b]	23.3	63.9
WR[b]	1667	1211
PVA fiber[c]	1710-3400	3000

[a] Data from [45,46].

[b] Data from [47-49] and cost range from 2018 to 2020.

[c] Data from [50-51], and cost in 2020.

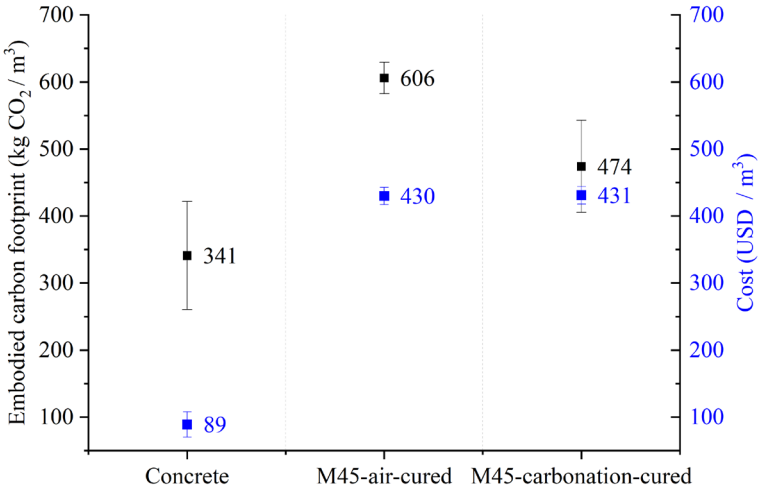

Figure 2-18. The embodied carbon footprint and material costs of conventional concrete and M45 ECC

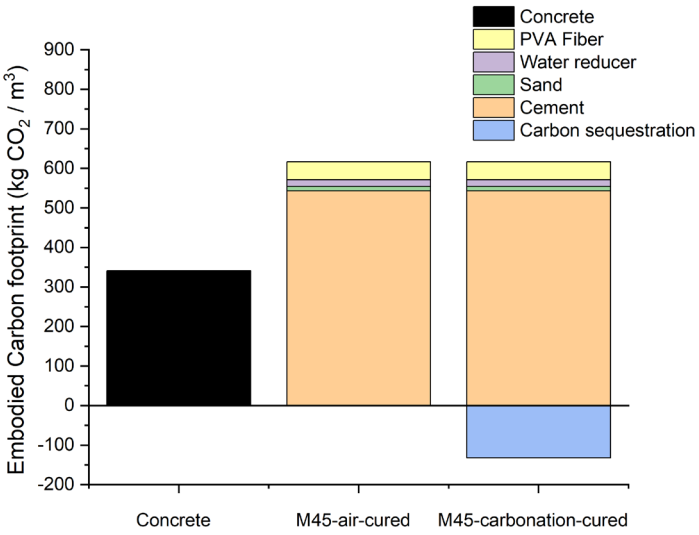

Figure 2-19. Contributions of embodied carbon footprint by ingredients

2.5. Field applications

The carbon sequestration mentioned above is limited to laboratory-scale materials. When scaling up to field-scale dimensions, i.e., real-size railway ties or in-situ pavements, the amount of CO_2 sequestered per cement mass through carbonation curing will significantly decrease due to diffusion limitations of CO_2 into larger volume materials.

2.5.1 Optimizing carbonation curing for large-scale applications

Following the carbonation process in Figure 1-3, carbonation depth (obtained by phenolphthalein test) and CO_2 uptake per cement mass can achieve 11 mm and 14.5% for beam specimens in Figure 2-6 and Table 2-4. However, the cross-section area for the field-scale specimen is usually ten to twenty times that of the beam specimen. To maximize the CO_2 uptake of the ECC rail tie, a 10 inches cube has been fabricated within the carbonation reactor, as shown in Figure 2-20, under various drying and CO_2 exposure duration. Under the same conditions for which 14.5% CO_2 uptake was achieved in the beam specimen, the 10 inches cube reached a carbonation depth of only 5 mm (6 mm decrease compared to the beam specimen), and the CO_2 uptake also decreased to 3.2 % (11.3% decrease compared to beam specimen). It is thus necessary to modify the carbonation process to improve the carbonation depth and CO_2 uptake for real-size railway ties.

Figure 2-20. Large-scale reactor for carbonation curing.

Drying time (i.e., 8 hours and 32 hours) and carbonation time (i.e., 24 hours, 48 hours, and 144 hours) were investigated to find a suitable duration for large-scale CO_2-curing. With 32 hours of drying and 48 hours of carbonation, the 10-inch cubic specimen can achieve approximately 8.4 % CO_2 uptake. More detailed results of carbonation depth for different carbonation processes and the CO_2 uptake are demonstrated in Figure 2-21 to 2-22 and Table 2-10. The CO_2 uptake for the carbonated area (gray area) is uniform, while in the non-carbonated area (purple area), the CO_2

uptake has a logarithmic distribution (see Figure 2-23 (a)). XRD analysis also confirmed this by observing the 2 theta of Calcite, as shown in Figure 2-23 (b).

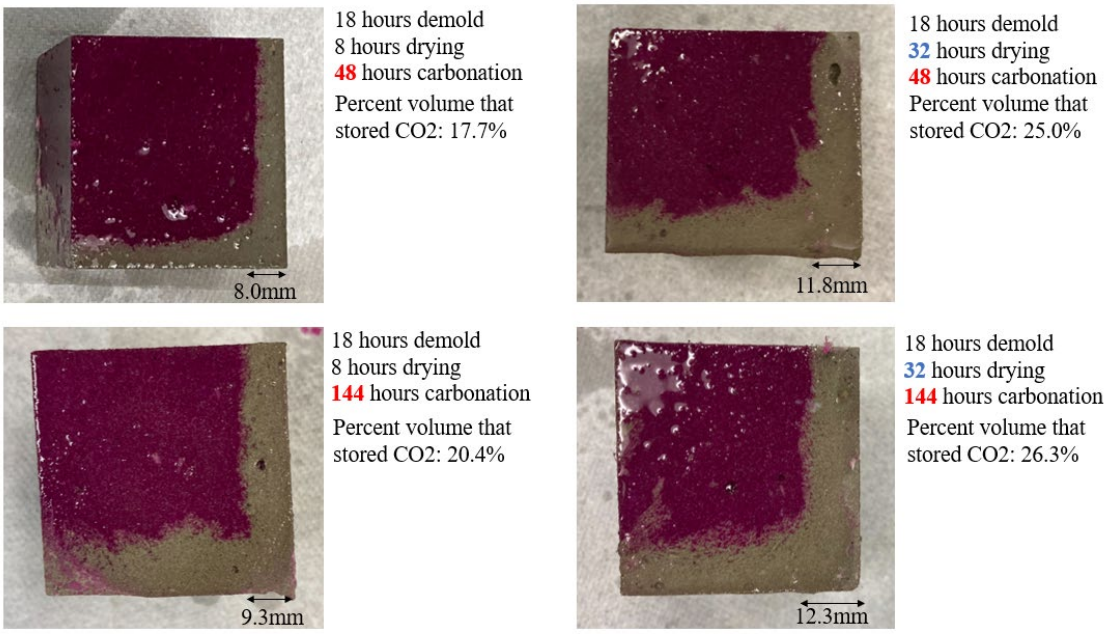

Figure 2-21. Carbonation depth of 10 inches cube specimens under different carbonation processes.

Table 2-10. CO_2 uptake (per cement mass) of 10 inches cube under different carbonation processes

Drying time (h)	Carbonation time (h)	CO2 uptake (g)	CO2 uptake (%)
8	24	302	3.2%
8	48	512	5.4%
8	144	586	6.2%
32	48	779	8.4%
32	144	806	8.6%

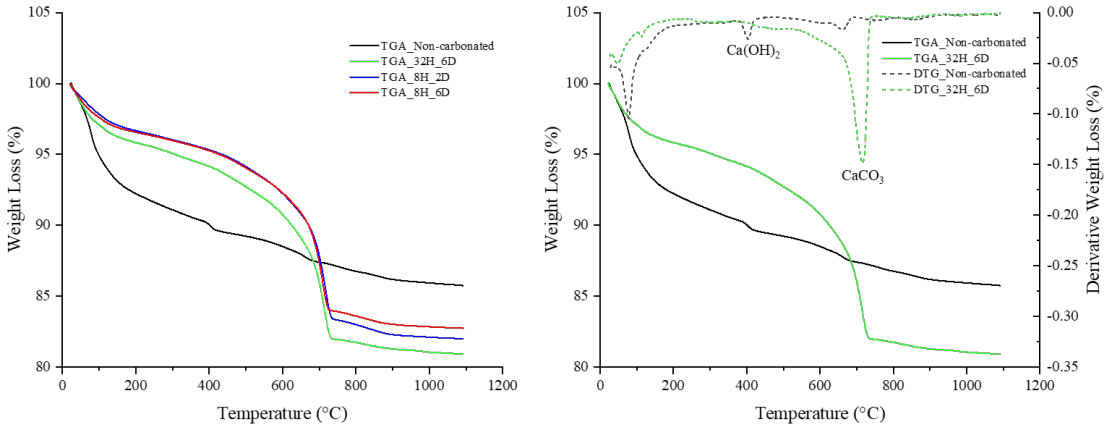

Figure 2-22. TGA and DTG for 10 inches cube under different carbonation process.

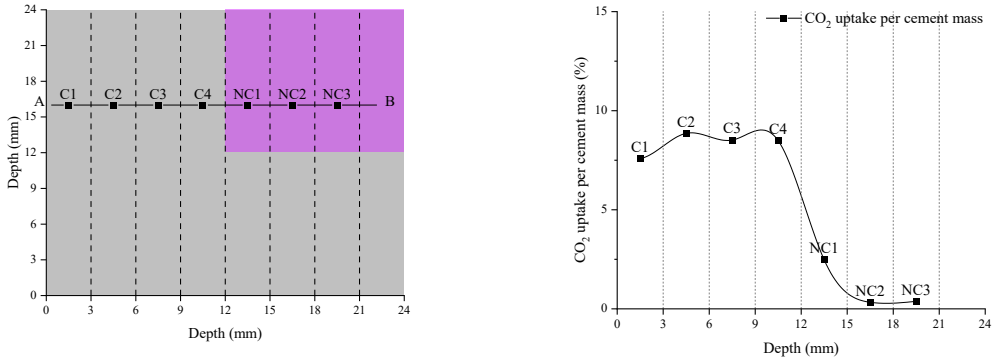

(a)

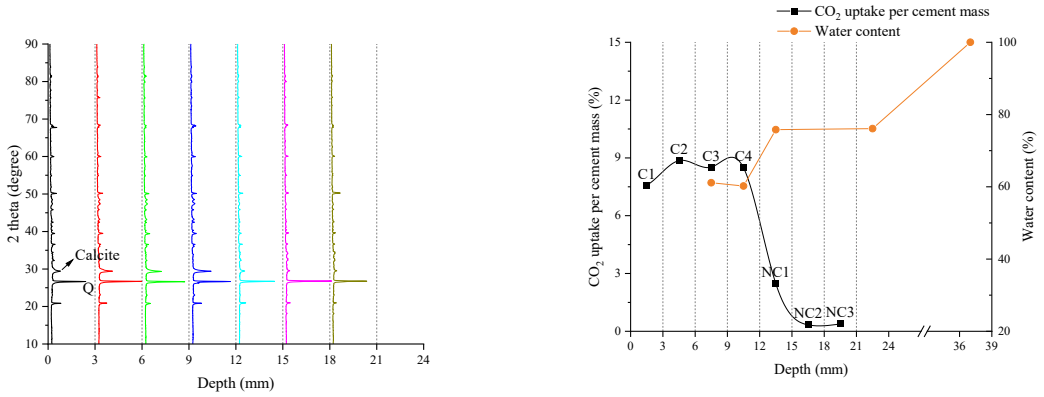

(b) (c)

Figure 2-23. (a) CO_2 uptake for different layers of cube, (b) XRD analysis for different layers of cube, (c) CO_2 uptake and water content for different layers of cube.

The results suggest that if the carbonation time is enough (i.e., 48 hours), the drying time will be the main factor impacting CO_2 uptake for large-scale specimens. The reason is that the carbonation of the ECC is highly dependent on the mixture's water content, as shown in Figure 2-23 (c). According to T.C. Power's empirical formula for components, volume changes during cement hydration in Figure 2-24 [52][53]. A longer drying time allows more water in capillary pores to evaporate from the mixture. Therefore, the mixture and CO_2 gas have more contact surface area to react, resulting in more CO_2 uptake and carbonation depth. Since there is no significant CO_2 uptake increase by extending the carbonation time from 48 hours to 144 hours, we chose 32 hours of drying and 48 hours of carbonation time as recommended for large-scale specimens' carbonation process (see Figure 2-25).

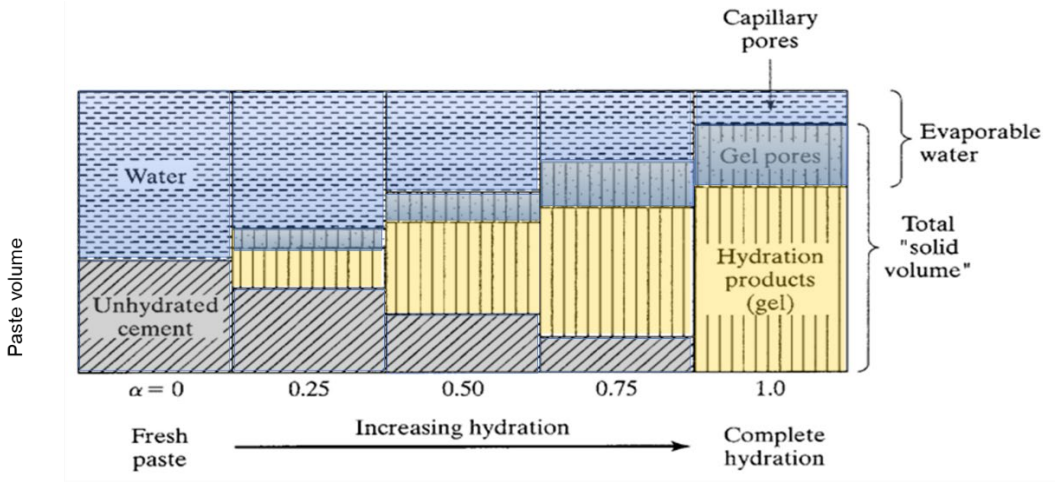

Figure 2-24. T.C. Power's empirical formula for component volume changes during cement hydration [53].

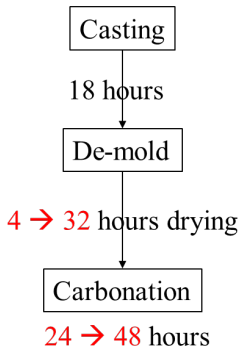

Figure 2-25. The recommended carbon curing process for larger-scale specimens.

2.5.2 Railway ties

Railway ties are chosen as field-scale products in this research based on several considerations. The rail industry is transitioning from wood ties to prestressed concrete railway ties due to the lack of quality wood. Conventional concrete railway ties use many prestressed wires to meet the American Railroad Engineering and Maintenance-of-Way Association (AREMA) standards. However, traditional prestressed concrete railway ties still fail prematurely due to the development of cracks (in the rail seat area and center binding), prestress losses, corrosion, and bond failure of prestressing wires [54][55][56]. Without any prestressing, ECC is considered a more durable material for railway ties that meet the AREMA standards.

The dimension of the real-size rail tie for this research is around 7'9"x12"x10", which meets the American Railway Engineering and Maintenance-of-Way Association (AREMA) standard for concrete railway ties [57]. The relevant equipment necessary for full-size rail tie construction includes (but is not limited to) a rail fastener system, cast-in shoulders, concrete/ECC molds, and vibration tools. Based on the literature review and iterations of communication with industrial specialists, we chose the E-Clip fastener from *Pandrol*. This fastener system has been widely adopted in North America and can be easily installed and removed without special tools [58][59]. The detailed e-clip and dimensions of large-scale carbonation-cured ECC railway ties can be found in Figure 2-26. *Helser Industry* built a custom mold due to the unique design of our railway ties (no prestressed wires). The rail will be used for the qualification lab tests before in-track testing of the carbonated ties is AREMA 141 RE rail [57].

(a)

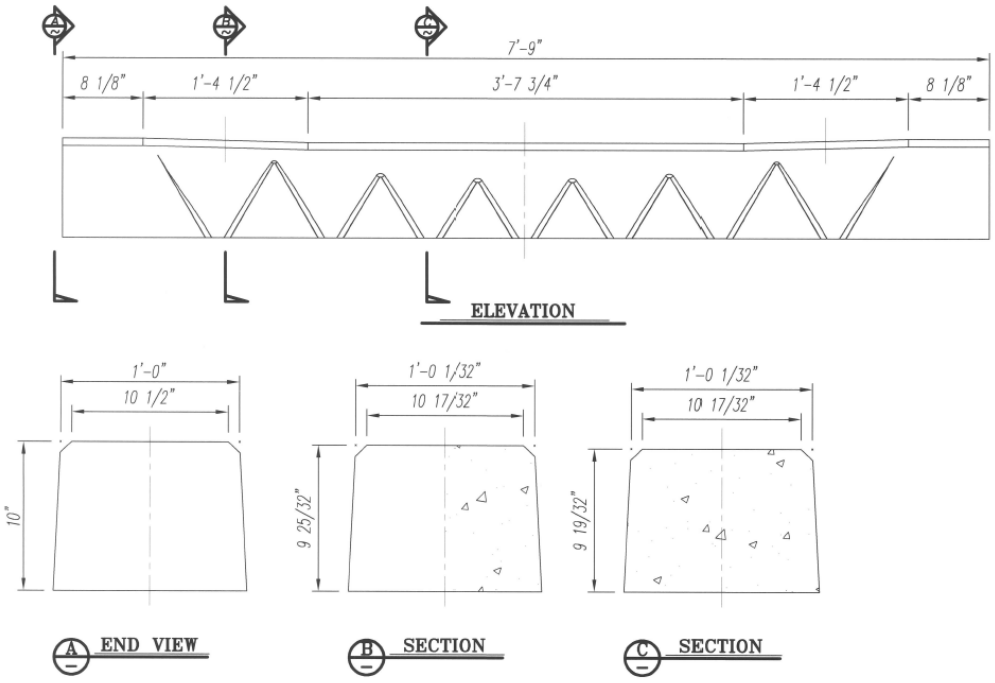

(b)

Figure 2-26. (a) *Pandrol* e-clip fastener systems, (b) dimensions of full-size carbonation-cured ECC railway ties.

Sixteen carbonation-cured ECC railway ties are prepared. Before Transportation Technology Center, Inc. (MxV Rai, TTCI) provided the single tie push test (STPT), the following prerequisite laboratory tests were conducted according to AREMA standards for a preliminary assess the railway tie's performance before installation in track. Three of the sixteen real-size ECC railway ties were prepared and examined following the AREMA standards [57]:

1. Test 1A: Bending-Rail seat Positive
2. Test 1C: Bending-Center Negative

3. Test 5A: Fastener Uplift Test
4. Test 6: Tie and Fastener System Wear/Deterioration Test
5. Test 7: Fastener Electrical Impedance Test

Detailed test setup can be found in Figure 2-27 to Figure 2-30. According to AREMA standards, the ECC railway ties passed tests 1A and 1C since no crack was observed after MTS held the required load P for 3 minutes. For test 5A, ECC railway ties passed the standard that no inserts were pulled out or loosened in the tie, and no fastening system components were fractured. The post-test condition for the fastening system is shown in Figure 2-31, which also achieves the requirement from AREMA. Finally, for test 7, the railway ties will meet the criteria if a minimum impedance value of 20,000 ohms has been measured. The impedance value for carbonation-cured ECC railway ties exceeded 200,000 ohms. The main reason is that no prestressed wires exist in ECC railway ties. Carbonation-cured ECC also passed Test 6. Only 1 marker reached 0.203” at 2.7 million cycles which is acceptable for the wear/deterioration test, showing promising wear resistance. All laboratory test results were also reviewed and accepted by MxV Rail engineers.

Figure 2-27. Test 6 setup for wear/deterioration test

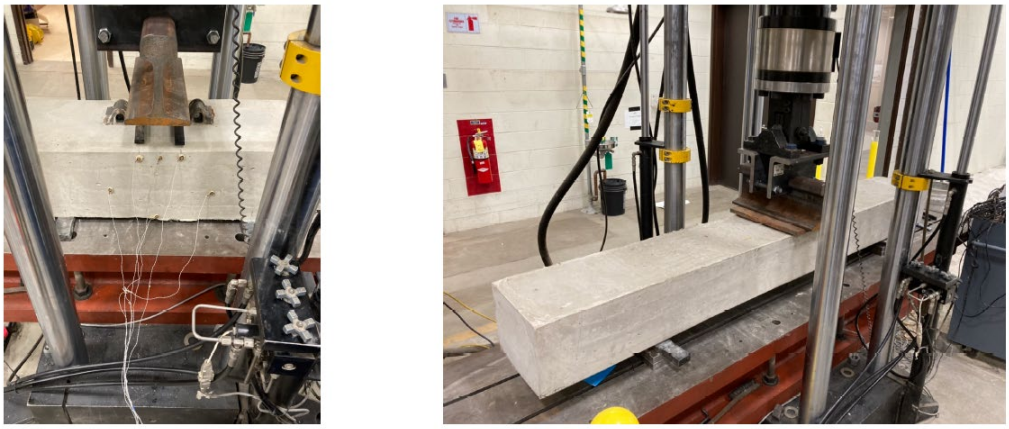

(a) (b)

Figure 2-28. Test setup for test (a) 1A, (b) 1C

Figure 2-29. Test 5A setup for fastener uplift test

Figure 2-30. Test 7A setup for impedance test

Figure 2-31. Post-test condition for fastener system

After passing all the prerequisite laboratory tests, a total of the remaining 13 carbonation-cured ECC railway ties were sent to TTCI to conduct STPT on the High Tonnage Loop (HTL) at the Facility for Accelerated Service Testing (FAST) located in Pueblo, Colorado, and included the following activities:

1. A test section with 13 concrete ties was established on the HTL at FAST.
2. Single tie push testing at 0 million gross tons (MGT) was conducted to characterize the track lateral stability of the concrete ties.
3. Inspections during and after the train operation were performed to document the conditions of the concrete tie section.

After the ties arrived, they were unloaded and visually inspected. The visual inspection showed the ties were intact and in good physical condition. A hydraulic tie inserter was used to install the ties in the track. The claw of the tie inserter caused the tie surface indentation/damage. Therefore, the installation method was changed to push the tie ends laterally using a rail crane to avoid tie damage. One tie experienced breakage during the rail crane push. Based on the observations made during the installation, one tie was selected to conduct AREMA bending tests 1A and 1C at the MxV Rail's Component Testing Laboratory to ensure the ties' in-track performance. Both tests met the AREMA test recommendations, and the tie section remained installed in the track for the duration of the testing.

After installing the 13 ties in the test zone, STP testing per the AREMA Manual for Railway Engineering, Chapter 30, Part 2, Test 8 – Single Tie Lateral Push Test1 was performed at 0 MGT [57]. In the test, the force required to push the tie laterally through the ballast section was measured as a function of the tie's lateral displacement. The hydraulic piston was attached to the tie and then pushed against the rail. Figure 2-32 shows the ties' STP test setup (conceptual schematic and actual setup). The STP tests were conducted for 0 MGT only. Every other tie in the 13-tie section was pushed for a total of six pushed ties. The push forces and tie lateral displacement for each of the six ties were recorded during tie pushing. Generally, the peak forces between 0 and 0.25 inch of the tie lateral displacement are tracked and evaluated at FAST. The average value of the peak forces was 2.76 kips, an amount above the required tie lateral resistance of 2 kips for FAST.

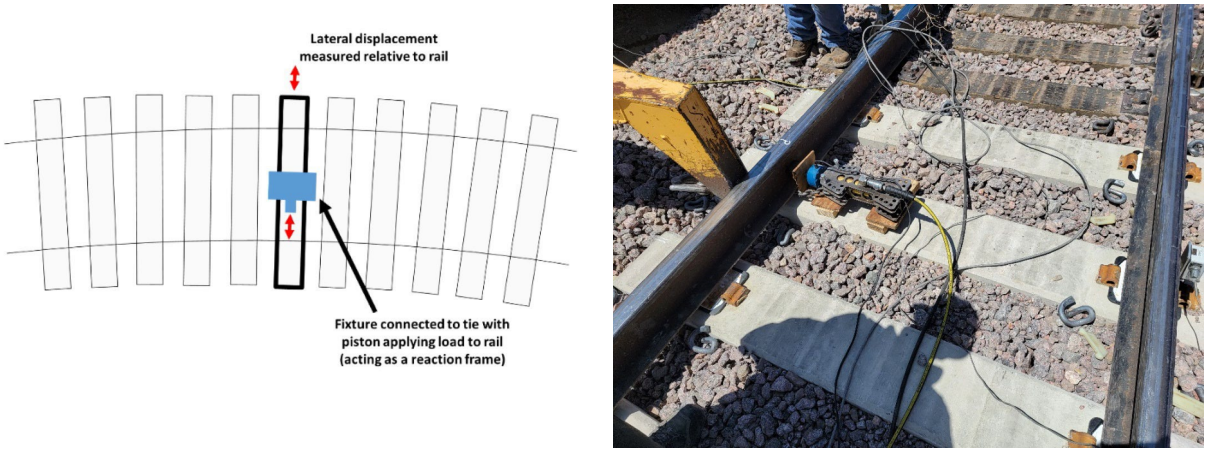

Figure 2-32. STP test setup for conceptual schematic and actual test setup on concrete ties

The train operation started after verifying that the carbonated ECC railway ties passed the STP standard. The track condition, including tie surface condition and track gauge, was monitored, especially the first 40 laps. Several observations were made during the inspection: Hairline cracks were detected near the rail seat and center of ties in Figure 2-33(a) and (b). Cracks grew broader as tonnage accumulated, as shown in Figure 2-33 (c) and (d). One tie pad and insulator were broken in the first 10 laps Figure 2-33 (e) and (f). The track gauge was monitored during the entire operation. The track gauge was maintained within 56.5–57.0 inches in the test section. Thirteen concrete ties were able to hold the track for the first night. However, after the first night of operation, 12 of the 13 ties had cracks, 8 of the 12 were fully cracked, and 4 of the 12 were half-cracked. Due to the safety concerns from these cracks, the entire test section had to be removed from the track, and the STP test at 10 MGT was canceled. Upon its removal, the tie section had accumulated 2.5 MGT.

Pre-carbonated ECC railway ties met the test requirements of the AREMA laboratory design tests for prestressed concrete ties. Based on the test results, the AREMA tests for prestressed concrete ties do not indicate ECC railway ties' in-track performance. Therefore, post-test observations were made to clarify the problems for carbonation-cured ECC railway ties. The cross-sectional area of the critical crack shows that unexpected non-uniform fiber dispersion was found, as shown in Figure 2-34. The fiber aligned in the same direction as the casting, which limited the performance of the real-size railway ties. When scaled up to the larger structural elements, this remains a technical challenge that needs to be solved.

Also, when scaling up to field-scale dimensions, the amount of CO_2 sequestrated per cement mass will likely be lower. Though we can achieve 8.4 % CO_2 uptake for full-size railway ties (i.e., 9 kg of CO_2 capture) by adjusting the carbonation process, there is still a need to find a way to enhance the carbon sequestration further to decrease the CO_2 footprint for larger field scale elements.

(a) Hairline crack around rail seat

(b) Hairline crack in tie center

(c) Crack after first lap

(d) Same crack after 120 laps

(e) Tie pad breakage

(f) Insulator crack

Figure 2-33. Tie condition inspection: (a) Hairline crack around rail seat; (b) Hairline crack in tie center; (c) Crack after first lap; (d) Same crack after 120 laps; (e) Tie pad breakage; (f) Insulator crack

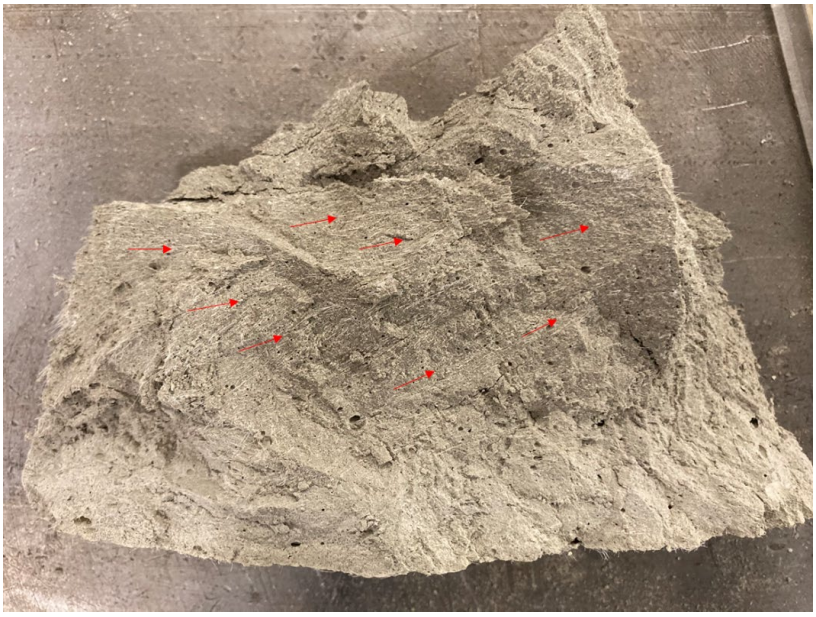

Figure 2-34. 11. Fiber dispersion at the failure section of carbonation-cured ECC railway ties

To substantiate the hypothesis that fiber dispersion impacts the high ductility of large-scale ECC railway ties through the formation of multiple cracks, a 10" by 5" by 22" deep beam sample was meticulously fabricated. This deep beam sample, half the width of the railway ties, was cast using a single batch of materials. Employing the same testing arrangement as Test 1A depicted in Figure 2-28(a), the deep beam samples exhibited the desired formation of multiple cracks (see Figure 2-35), thus validating that proper casting techniques can effectively address fiber dispersion issues and maintain performance in large-scale ECC specimens.

Figure 2-35. Test setup for deep beam and the multiple cracks formation at failure

2.6. Conclusions

This study examined the impact of carbonation curing on the fatigue resistance of ECC. The results demonstrated that carbonation-cured ECC is more durable and more ductile under fatigue loading conditions, compared to air-cured ECC. This research establishes evidence at the laboratory scale that carbonation curing of ECC leads to a lowering of embodied carbon in precast structural elements and of the operational carbon during structural use.

Specifically, ECC can achieve 20% CO_2 uptake by cement mass after a 24-hour carbonation curing period. This direct sequestration of CO_2 lowers the CO_2 footprint of precast ECC elements. Carbonation curing leads to improvements in ECC's mechanical properties including increased first cracking flexural strength (27% increase), ultimate flexural strength (32% increase), and deformation capacity (69% increase of midspan deflection).

Carbonation curing was also shown to enhance the chemical bond, G_d, and frictional bond, τ_0, between the PVA fiber/matrix interface, which improves the composite crack width control and fiber bridging capacity. Consequently, the average crack width decreased from 62 to 30 μm after carbonation curing, and the maximum crack width also decreased from 148 μm to 76 μm after carbonation curing.

Finally, carbonation curing improves the fatigue life of ECC at high-stress levels and maintains comparable fatigue life when the stress is low. This is attributed to ECC's enhanced crack width control ability from increasing fiber/matrix interface bond after carbonation curing, which slows down crack propagation and extends the fatigue life of ECC.

When scaling up to field-scale dimensions, the amount of CO_2 sequestered per cement mass through carbonation curing is lower than indicated here due to diffusion limitations of CO_2 into larger volume materials, as demonstrated in the railway ties application. Further, the performance of structural elements at field scales is impacted by an increase in material non-uniformity, especially related to non-uniform fiber dispersion when ECC is processed in large batches. Though this problem can be solved with proper mixing and casting methods, there is a need to extend this research to verify the conclusions further and to understand the limitations of carbonation-cured ECC performance in actual structural elements. Indeed, large scale structures (bridge deck slab, building frames, one-ton dampers, …) built with ECC (without carbonation-curing) have been successfully cast and tested [60-63]. In addition, the durability of carbonation-

cured ECC elements exposed to typical environmental conditions should be evaluated at laboratory and field scales.

2.7. References

[1] Y.C. Díaz, S.S. Berriel, U. Heierli, A.R. Favier, I.R.S. Sánchez Machado, K.L. Scrivener, J.F. Martirena Hernández, G. Habert, Limestone calcined clay cement as a low-carbon solution to meet expanding cement demand in emerging economies, Dev Eng. 2 (2017) 82–91. https://doi.org/10.1016/j.deveng.2017.06.001.

[2] H. Ritchie, M. Roser, P. Rosado, CO_2 and Greenhouse Gas Emissions, OurWorldInData. (2020). https://ourworldindata.org/co2-and-greenhouse-gas-emissions (accessed March 10, 2023).

[3] M.D. Valérie, P. Zhai, H.O. Pörtner, D. Roberts, J. Skea, P.R. Shukla, A. Pirani, IPCC report Global warming of 1.5°C, IPCC. (2018). www.environmentalgraphiti.org.

[4] V.C. Li, Engineered Cementitious Composites – Bendable Concrete for Sustainable and Resilient Infrastructure, Springer, Germany, 2019. https://doi.org/10.1007/978-3-662-58438-5.

[5] V.C. Li, S. Wang, C. Wu, Tensile strain-hardening behavior or polyvinyl alcohol engineered cementitious composite (PVA-ECC), ACI Mater J. 98 (2001) 483–492. https://doi.org/10.14359/10851.

[6] M.D. Lepech, V.C. Li, R.E. Robertson, G.A. Keoleian, Design of green engineered cementitious composites for improved sustainability, ACI Mater J. 105 (2008) 567–575. https://doi.org/10.14359/20198.

[7] D. Shoji, Z. He, D. Zhang, V.C. Li, The greening of engineered cementitious composites (ECC): A review, Constr Build Mater. 327 (2022). https://doi.org/10.1016/j.conbuildmat.2022.126701.

[8] D. Zhang, B.R. Ellis, B. Jaworska, W.H. Hu, V.C. Li, Carbonation curing for precast Engineered Cementitious Composites, Constr Build Mater. 313 (2021). https://doi.org/10.1016/j.conbuildmat.2021.125502.

[9] V. Rostami, Y. Shao, A.J. Boyd, Z. He, Microstructure of cement paste subject to early carbonation curing, Cem Concr Res. 42 (2012) 186–193. https://doi.org/10.1016/j.cemconres.2011.09.010.

[10] D. Zhang, T. Liu, Y. Shao, Weathering Carbonation Behavior of Concrete Subject to Early-Age Carbonation Curing, Journal of Materials in Civil Engineering. 32 (2020) 04020038. https://doi.org/10.1061/(asce)mt.1943-5533.0003087.

[11] V. Rostami, Y. Shao, A.J. Boyd, Durability of concrete pipes subjected to combined steam and carbonation curing, Constr Build Mater. 25 (2011) 3345–3355. https://doi.org/10.1016/j.conbuildmat.2011.03.025.

[12] D. Zhang, B. Jaworska, Effect of Carbonation Curing on Portland Cement MgSO4 Attack: Laboratory Characterization at 900 Days, Journal of Materials in Civil Engineering. 33 (2021) 04021032. https://doi.org/10.1061/(asce)mt.1943-5533.0003647.

[13] D. Zhang, Y. Shao, Surface scaling of CO2-cured concrete exposed to freeze-thaw cycles, Journal of CO2 Utilization. 27 (2018) 137–144. https://doi.org/10.1016/j.jcou.2018.07.012.

[14] D. Zhang, Y. Shao, Enhancing chloride corrosion resistance of precast reinforced concrete by carbonation curing, ACI Mater J. 116 (2019) 3–12. https://doi.org/10.14359/51714461.

[15] AREMA, Manual for Railway Engineering Chapter 30 - Ties, American Railway Engineering and Maintenance-of-Way Association. (2021).

[16] V. Ramakrishnan, G.Y. Wu, G. Hosalli, Flexural fatigue strength, endurance limit, and impact strength of fiber reinforced concretes, Transp Res Rec. (1989) 17–24.

[17] G.P. Tilly, Fatigue of Steel Reinforcement Bars in Concrete: a Review, Fatigue Fract Eng Mater Struct. 2 (1979) 251–268. https://doi.org/10.1111/j.1460-2695.1979.tb01084.x.

[18] S. V. Kolluru, E.F. O'Neil, J.S. Popovics, S.P. Shah, Crack Propagation in Flexural Fatigue of Concrete, J Eng Mech. 126 (2000) 891–898. https://doi.org/10.1061/(asce)0733-9399(2000)126:9(891).

[19] M.K. Lee, B.I.G. Barr, An overview of the fatigue behaviour of plain and fibre reinforced concrete, Cem Concr Compos. 26 (2004) 299–305. https://doi.org/10.1016/S0958-9465(02)00139-7.

[20] G. Batson, C. Ball, L. Bailey, E. Landers, J. Hooks, Flexural Fatigue Strength of Steel Fiber Reinforced Concrete Beams., Journal of American Concrete Institute. 69 (1972) 673–677. https://doi.org/10.14359/11275.

[21] B. Isojeh, M. El-Zeghayar, F.J. Vecchio, Fatigue resistance of steel fiber-reinforced concrete deep beams, ACI Struct J. 114 (2017) 1215–1226. https://doi.org/10.14359/51700792.

[22] Z. Jun, H. Stang, Fatigue performance in flexure of fiber reinforced concrete, ACI Mater J. 95 (1998) 58–67. https://doi.org/10.14359/351.

[23] L. Xiaopeng, M. Li, G. Song, Energy-dissipating and self-repairing SMA-ECC composite material system, Smart Mater Struct. 24 (2015). https://doi.org/10.1088/0964-1726/24/2/025024.

[24] T. Matsumoto, P. Suthiwarapirak, T. Kanda, Mechanisms of Multiple Cracking and Fracture of DFRCC under Fatigue Flexure, Journal of Advanced Concrete Technology. 1 (2003) 299–306. https://doi.org/10.3151/jact.1.299.

[25] P. Suthiwarapirak, T. Matsumoto, T. Kanda, Multiple cracking and fiber bridging characteristics of engineered cementitious composites under fatigue flexure, Journal of Materials in Civil Engineering. 16 (2004) 433–443. https://doi.org/10.1061/(ASCE)0899-1561(2004)16:5(497).

[26] B. Huang, Fatigue performance of strain-hardening fiber-reinforced cementitious composite and its functionally-graded structures, 2018. https://doi.org/10.13140/RG.2.2.31165.31204.

[27] P. Suthiwarapirak, T. Matsumoto, T. Kanda, Flexural fatigue failure characteristics of an engineered cementitious composite and polymer cement mortars., Doboku Gakkai Ronbunshu. (2002) 121–134. https://doi.org/10.2208/jscej.2002.718_121.

[28] M.D. Lepech, V.C. Li, Large-scale processing of engineered cementitious composites, ACI Mater J. 105 (2008) 358–366. https://doi.org/10.14359/19897.

[29] ASTM, Standard Specification for Portland Cement, American Society for Testing and Materials. (2015) 1–11. https://doi.org/10.1520/C0150.

[30] H. Yokota, K. Rokugo, N. Sakata, Recommendations for Design and Construction of High Performance Fiber Reinforced Cement Composite with Multiple Fine Cracks, Japan Society of Civil Engineers. (2008).

[31] J. Zhang, V.C. Li, Monotonic and fatigue performance in bending of fiber-reinforced engineered cementitious composite in overlay system, Cem Concr Res. 32 (2002) 415–423. https://doi.org/10.1016/S0008-8846(01)00695-0.

[32] C. Redon, V.C. Li, C. Wu, H. Hoshiro, T. Saito, A. Ogawa, Measuring and Modifying Interface Properties of PVA Fibers in ECC Matrix, Journal of Materials in Civil Engineering. 13 (2001) 399–406. https://doi.org/10.1061/(asce)0899-1561(2001)13:6(399).

[33] A. Katz, V.C. Li, A special technique for determining the bond strength of micro-fibres in cement matrix by pullout test, J Mater Sci Lett. 15 (1996) 1821–1823. https://doi.org/10.1007/BF00275353.

[34] T. Kanda, V.C. Li, Interface Property and Apparent Strength of High-Strength Hydrophilic Fiber in Cement Matrix, Journal of Materials in Civil Engineering. 10 (1998) 5–13. https://doi.org/10.1061/(asce)0899-1561(1998)10:1(5).

[35] I. Monteiro, F.A. Branco, J. De Brito, R. Neves, Statistical analysis of the carbonation coefficient in open air concrete structures, Constr Build Mater. 29 (2012) 263–269. https://doi.org/10.1016/j.conbuildmat.2011.10.028.

[36] E. Possan, W.A. Thomaz, G.A. Aleandri, E.F. Felix, A.C.P. dos Santos, CO2 uptake potential due to concrete carbonation: A case study, Case Studies in Construction Materials. 6 (2017) 147–161. https://doi.org/10.1016/j.cscm.2017.01.007.

[37] M. Otieno, J. Ikotun, Y. Ballim, Experimental investigations on the influence of cover depth and concrete quality on time to cover cracking due to carbonation-induced corrosion of steel in RC structures in an urban, inland environment, Constr Build Mater. 198 (2019) 172–181. https://doi.org/10.1016/j.conbuildmat.2018.11.215.

[38] P.F. Marques, A. Costa, Service life of RC structures: Carbonation induced corrosion. Prescriptive vs. performance-based methodologies, Constr Build Mater. 24 (2010) 258–265. https://doi.org/10.1016/j.conbuildmat.2009.08.039.

[39] P.F. Marques, C. Chastre, Â. Nunes, Carbonation service life modelling of RC structures for concrete with Portland and blended cements, Cem Concr Compos. 37 (2013) 171–184. https://doi.org/10.1016/j.cemconcomp.2012.10.007.

[40] W. Liu, S. Xu, P. Feng, Fatigue damage propagation models for ductile fracture of ultrahigh toughness cementitious composites, International Journal of Damage Mechanics. 26 (2017) 919–932. https://doi.org/10.1177/1056789516635727.

[41] M.M. Pedersen, Introduction To Metal Fatigue, Aarhus University Technical Report ME-TR-11. (2018).

[42] P. Suthiwarapirak, T. Matsumoto, Fiber Bridging Degradation Based Fatigue Analysis of ECC under Flexure, J Appl Mech. 6 (2003) 1179–1188. https://doi.org/10.2208/journalam.6.1179.

[43] J. Zhang, H. Stang, V.C. Li, Crack bridging model for fibre reinforced concrete under fatigue tension, Int J Fatigue. 23 (2001) 655–670. https://doi.org/10.1016/S0142-1123(01)00041-X.

[44] J.D. Rathod, Effect of Single Fiber Pull Out Test Result on Flexural Performance of ECC, Journal of Civil & Environmental Engineering. 04 (2014) 2–7. https://doi.org/10.4172/2165-784x.1000140.

[45] J.S. Damtoft, J. Lukasik, D. Herfort, D. Sorrentino, E.M. Gartner, Sustainable development and climate change initiatives, Cem Concr Res. 38 (2008) 115–127. https://doi.org/10.1016/j.cemconres.2007.09.008.

[46] F. Pacheco-Torgal, Z. Abdollahnejad, S. Miraldo, M. Kheradmand, Alkali-Activated Cement-Based Binders (AACBs) as Durable and Cost-Competitive Low-CO2 Binder Materials: Some Shortcomings That Need to be Addressed, in: Handbook of Low Carbon Concrete, Elsevier Inc., 2017: pp. 195–216. https://doi.org/10.1016/B978-0-12-804524-4.00009-9.

[47] H. Zhu, D. Zhang, T. Wang, H. Wu, V.C. Li, Mechanical and self-healing behavior of low carbon engineered cementitious composites reinforced with PP-fibers, Constr Build Mater. 259 (2020) 119805. https://doi.org/10.1016/j.conbuildmat.2020.119805.

[48] D. Zhang, B. Jaworska, H. Zhu, K. Dahlquist, V.C. Li, Engineered Cementitious Composites (ECC) with limestone calcined clay cement (LC3), Cem Concr Compos. 114 (2020). https://doi.org/10.1016/j.cemconcomp.2020.103766.

[49] H.L. Wu, D. Zhang, B.R. Ellis, V.C. Li, Development of reactive MgO-based Engineered Cementitious Composite (ECC) through accelerated carbonation curing, Constr Build Mater. 191 (2018) 23–31. https://doi.org/10.1016/j.conbuildmat.2018.09.196.

[50] D. Zhang, J. Yu, H. Wu, B. Jaworska, B.R. Ellis, V.C. Li, Discontinuous micro-fibers as intrinsic reinforcement for ductile Engineered Cementitious Composites (ECC), Compos B Eng. (2020). https://doi.org/10.1016/j.compositesb.2020.107741.

[51] Z. Qi, W. Chen, L. Zhang, Z. Huang, An integrated design method for functional cementitious composites (FCC), Constr Build Mater. 249 (2020). https://doi.org/10.1016/j.conbuildmat.2020.118698.

[52] C.Cement, Limestone fillers conserve cement, Concr. Int. (2009). http://concrete.nist.gov/~bentz/ci3111bentzreadonly.pdf.

[53] T.C., Powers, T.L.Brownyard, Studies of the Physical Properties of Hardened Portland Cement Paste, ACI Journal, Proceedings V. 43, (1946).

[54] R.H.Lutch, D.K.Harris, T.M.Ahlborn, Causes and preventative methods for rail seat abrasion in North America's railroads, Proc. Int. Conf. Cold Reg. Eng. 41072 (2009) 455–466. https://doi.org/10.1061/41072(359)44.

[55] R.H.Lutch, D.K.Harris, T.M.Ahlborn, Prestressed Concrete Ties in North America, AREMA Annu. Conf. (2009) 1–39.

[56] N., Peters, CN 60E Concrete Tie Development AREMA: 25. (2003)

[57] AREMA Manual for Railway Engineering, Chapter 30 Ties, (2021).

[58] A.Hasap, P.Paitekul, N.Noraphaiphipaksa, C.Kanchanomai, Analysis of the fatigue performance of elastic rail clip, Eng. Fail. Anal. 92 (2018) 195–204. https://doi.org/10.1016/j.engfailanal.2018.05.013.

[59] J.Sadeghi, M.Fesharaki, A.Khajehdezfuly, Influences of train speed and axle loads on life cycle of rail fastening clips, Trans. Can. Soc. Mech. Eng. 39 (2015) 1–11.

[60] H.Fukuyama, Y.Sato, V.C.Li, Y.Matsuzaki, H.Mihashi, Ductile Engineered Cementitious Composite Elements for Seismic Structural Application, 12WCEE, (2000).

[61] M.D. Lepech, V.C. Li, Application of ECC for bridge deck link slabs, in: Materials and Structures/Materiaux et Constructions, 2009: pp. 1185–1195. https://doi.org/10.1617/s11527-009-9544-5.

[62] M. Maruta, T. Kanda, S. Nagai, Y. Yamamoto, New High-rise RC Structure Using Pre-cast ECC Coupling Beam, Concrete Journal. 43 (2005) 11.

[63] H. Fukuyama, H. Suwada, Experimental Response of HPFRCC Dampers for Structural Control, Journal of Advanced Concrete Technology. 1 (2003) 317–326.

Chapter 3. Utilization of Industrial Waste Materials (IWMs)

While carbonation curing, as discussed in Chapter 2, can effectively reduce the embodied carbon footprint of ECC by 22% at the laboratory scale, it is noteworthy that the CO_2 emissions associated with ECC remain 1.5 times higher than those of conventional concrete. Moreover, when ECC is applied in field-scale applications, the embodied carbon footprint tends to increase due to reduced CO_2 sequestration efficiency. Consequently, there is a pressing need to explore additional strategies for further decarbonizing ECC. This chapter integrates the findings on carbonation curing from Chapter 2 with the utilization of various innovative waste materials (IWMs), presenting a novel approach for developing a low-carbon and cost-effective ECC.

3.1. Introduction

Ocean plastic pollution has become a major environmental challenge [1]. The annual marine plastic debris that flows into ocean are expected to be 9-23 million tons and will continuously increase without any action [2,3]. Specifically, abandoned, lost and discarded fishing gear (ALDFG) is recognized as the most harmful waste of marine plastic pollution, which enters ocean 1.9-2.3 million tons annually [3,4]. The ALDFG seriously impacts aquatic ecosystem and threatens fish stocks, causing approximately 3300-33000 USD per tons economic costs annually [5]. It requires a significant reduction in plastic debris to solve this crisis by recycling the gear that is recovered or at end of life in accordance with the Global Ghost Gear Initiative (GGGI) [4] and find alternative applications for the recycled plastic waste materials.

Mitigating CO_2 emissions is one of the most critical challenges for our society. If all countries in the world meet their current targets set within the Paris climate agreement, the estimated warming will be around 2.6-3.2 degree Celsius in 2100 [6]. The production of Portland cement accounts for 8% of global CO_2 emissions, which makes concrete a significant CO_2 emitter [6]. As the global construction market continuously expands, effective strategies for mitigating concrete CO_2 footprint are much needed. Repurposing the waste ALDFG, i.e., waste fishing nets into fibers for reinforcement of concrete may be a potential solution by substituting the

conventional synthetic fiber with the recycled waste fishing nets. [7] pioneered the study of concrete reinforcement with fibers from waste fishing nets.

ECC is a fiber-reinforced cementitious composite that has high tensile ductility several hundred times that of normal concrete [8]. It has been proven that the intrinsic tight crack width of ECC even when highly strained retains a lower water permeability [9] and chloride diffusivity [10], leading to enhanced infrastructure durability [11]. This implies the feasibility of developing low maintenance civil infrastructure with low operational carbon. ECC is now deployed in the building, transportation, and energy infrastructures for enhanced resilience and durability [8].

Despite the advantages, the high amount of cement in ECC due to eliminating the coarse aggregate led to a high embodied CO_2 footprint for ECC. For example, M45 ECC, a most studied ECC mix composition, possesses an embodied carbon footprint twice that of conventional concrete [12]. The development of a truly low-carbon ECC remains an open challenge. In recent research, industrial waste materials (IWMs) were used as substitutes for raw materials in typical ECC mixtures to reduce the CO_2 footprint of ECC [13] such as limestone calcined clay cement (LC3) ECC. LC3 improves the tensile ductility and crack width control capacity of ECC [14–16], reduce the cement carbon emissions and costs by up to 35% [17] and 15-25% [18] compared to ordinary Portland cement (OPC), although the compressive strength of LC3-ECC is lowered by 12-30% compared to OPC-ECC [14]. By substituting OPC with LC3, ECC's CO_2 footprint and costs can be significantly reduced [12].

Polyvinyl alcohol (PVA), polypropylene (PP), and polyethylene (PE) fibers are common fibers for reinforcing ECC. Specifically, PVA fiber has been tailored with a surface coating for optimal reinforcement performance in ECC [19]. PE fiber has been widely applied to high-performance ECC due to its high strength, high aspect ratio, and high complimentary energy for multiple steady-state cracking, which positively affects ECC’s performance [20,21]. However, PVA and PE fibers have high embodied carbon footprint, energy, and costs while PP fibers have limited reinforcement performance [22]. It Is essential to find a substitute fiber for PVA and PE fibers that lowers the costs and carbon footprint of ECC to make it more competitive to conventional concrete. Waste polyethylene rope fiber (WPE) is an industrial waste fiber from the fishing industry, i.e., fishing nets. The waste fishing nets discard each year is about 10% of global marine plastic waste (by volume) [23,24]. Repurposing WPE for ECC has the potential to reduce

marine waste while greening ECC. Specifically, WPE meets all the requirements for fiber in ECC: a minimum tensile strength of 1000 MPa, an inelastic failure strain greater than 5%, and a suitable diameter between 30-50 μm [25], making it a potential substitute fiber for virgin PE or PVA fibers in low-carbon ECC.

Carbonation curing lowers concrete carbon footprint by sequestering CO_2 through its early-age curing process. During carbonation curing of a precast element, CO_2 reacts with calcium silicates and their hydration products and is converted into calcium carbonate ($CaCO_3$) [26]. Meanwhile, [26–29] studied the carbonation curing effect on the tensile, flexural, and fatigue performance of ECC which were found to be improved due to the accelerated cement reaction and denser microstructure by $CaCO_3$ precipitation. This also enhanced the fiber/matrix interface bonding to control crack width, which lowered the water permeability and promoted the self-healing of ECC (Lepech and Li, 2009; Li and Herbert, 2013). However, denser microstructure also limited CO_2 sequestration since it became harder for CO_2 to diffuse into the inner matrix. Therefore, finding a way to help CO_2 sequestrate deeper into a precast product is needed.

Sisal fiber has been used as a natural fiber reinforcement in cement and geopolymer composites for its low energy consumption and greenhouse gas emissions [32]. Sisal fiber is one of the most produced fibers globally and accounts for 2% of the world's plant fiber production with at least 300 thousand tons of annual production [33,34]. Compared to PE and glass fibers, sisal fiber lowers the embodied CO_2 footprint by 75-95% of and the embodied energy by 85-95% [35]. The geometry of sisal fiber is a tubular pillar [36,37], which may serve as a conduit to promote CO_2 diffusion in a cementitious matrix, thus enhancing CO_2 sequestration. The reduced alkalinity by carbonation curing [38] will also solve the well-known degradation problem of sisal fiber in a cementitious matrix [32]. In this study, sisal fibers were adopted for the sole purpose of channeling CO_2 deeper into the precast element, taking advantage of their hollow nature. Their mechanical reinforcement effect is assumed negligible when compared with that from the WPE fibers. Hence, any degradation of sisal fiber in an alkaline environment is unlikely to affect the composite's long-term properties.

By combining a low-carbon binder, CO_2 sequestration, and waste fiber utilization, this research develops a sustainable ECC with comparable cost and CO_2 footprint to conventional concrete while recycling the plastic marine waste. By using LC3, WPE, waste foundry sand (WFS),

sisal fiber, and carbonation curing (see Figure 3-1), a comprehensive experimental program including compressive strength, uniaxial tensile strength, crack patterns, interfacial bonding strength, cost, embodied carbon footprint and energy evaluation was initiated. To identify the effects of adding sisal fiber on ECC's mechanical properties and carbonation efficiency, four different amounts of sisal fiber were considered for both carbonation curing and air curing conditions for OPC-ECC. For the one with the best performance, OPC was substituted by LC3 or WFS to minimize the cost and embodied carbon footprint. Thermogravimetric analysis (TGA) was used to evaluate the CO_2 uptake of ECC mix proportions. Single fiber pull-out tests were conducted on WPE and Sisal fiber to determine the interfacial bond between the fiber and cementitious matrix.

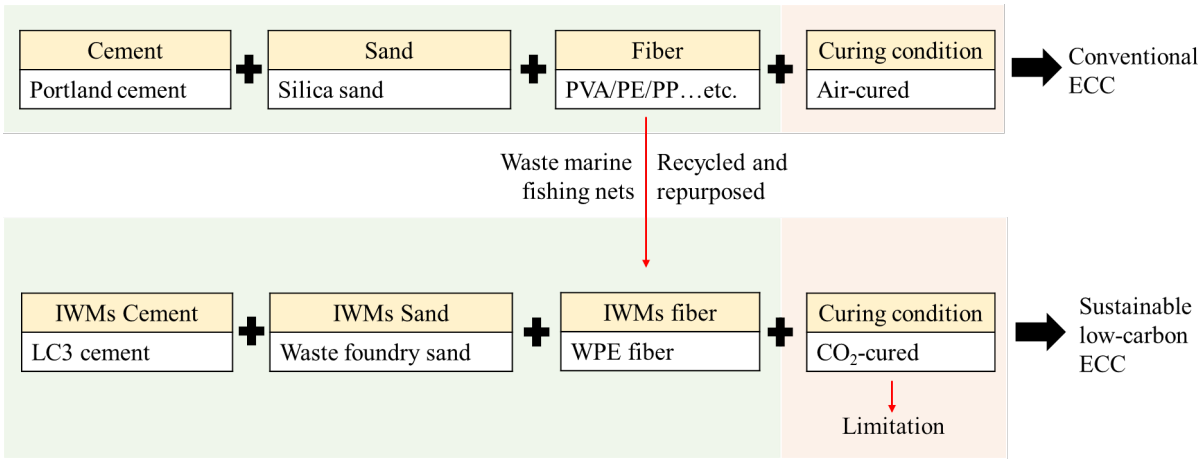

Figure 3-1. Research framework for sustainable low-carbon ECC development

3.2. Experimental program

3.2.1 Materials and mix proportions

Seven mix proportions were designed (Table 3-1). The materials for these mixtures include type 1L ordinary Portland cement (OPC) from Lafarge Holcim cement, metakaolin (MK, Sikacrete®M-100) from Sika Corporation, limestone (LS, Snowhite®12-PT) from Omya Canada Inc., F-75 whole-grain silica sand from U.S. Silica Holdings Inc., waste foundry sand (WFS) with 270 μm mean particle size from Aero Metals Inc., Class F fly ash (FA) from Boral Material Technologies Inc. The high-range water reducer (WR, MasterGlenium 7920) from BASF. The particle size distribution for silica sand and WFS was measured according to ASTM C136 [39]

corresponding distribution curves for WFS from the literature [40–42] are also shown in Figure 3-2. The chemical compositions of FA, MK, and LS are listed in Table 3-2.

The waste polyethylene rope fiber (WPE) is from discarded fishing gears, cut into 12mm length filaments by laser. The sisal fiber is from Carriage House Paper. More detailed dimension and mechanical characteristics of WPE and sisal fiber can be found in Table 3-3.

Table 3-1 Mix proportion of ECC (kg/m^3).

Mixture	OPC	LS	MK	Sand		FA	Water	Fiber[a]		WR
				Silica sand	WFS			WPE	Sisal	
OPC-0S20	570	0	0	400	0	760	367.2	0%	2%	0.5
OPC-2S00	570	0	0	400	0	760	367.2	2%	0%	0.5
OPC-2S05	570	0	0	400	0	760	367.2	2%	0.5%	0.5
OPC-2S10	570	0	0	400	0	760	367.2	2%	1%	0.5
OPC-2S15	570	0	0	400	0	760	367.2	2%	1.5%	0.5
LC3-2S10[b]	314	171	85.5	400	0	760	367.2	2%	1%	0.5
WFS-2S10	570	0	0	200	162.3	760	367.2	2%	1%	1.0

[a]Volume fraction.

[b]55% OPC, 30% MK, and 15% LS for LC3 binder [14].

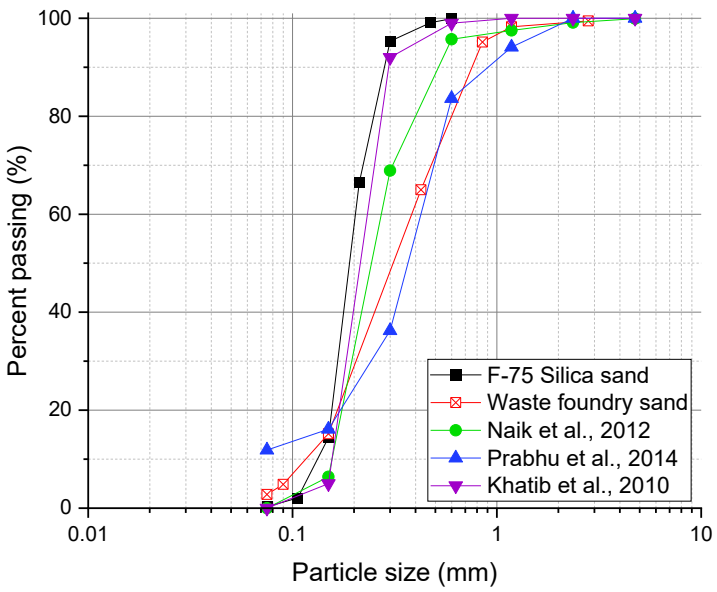

Figure 3-2. Particle size distribution for F-75 silica sand and WFS [40–42].

Table 3-2. Chemical compositions of FA, MK, and LS (%).

Material	SiO_2	Al_2O_3	Fe_2O_3	CaO	K_2O	SO_3	MgO	TiO_2	P_2O_5	$CaCO_3$
FA	52.2	22.2	13.5	3.4	2.6	2.2	0.9	1.0	0.1	0.0
MK	50.8	46.6	0.5	0.0	0.3	0.1	0.0	1.7	0.0	0.0
LS	2.3	0.0	0.0	0.0	0.0	0.0	0.0	0.0	0.0	97.7

Table 3-3. Properties of fiber.

Fiber type	Length (mm)	Diameter (μm)	Fiber aspect ratio	Tensile strength (MPa)	Young's modulus (GPa)	Density (g/cm^3)
WPE	12[a]	42[a]	285	1550[b]	100.3[b]	0.97[b]
Sisal fiber[c]	8	150	53	490	21.5	1.45

[a] Measured by optical microscope.

[b] Measured according to ASTM 3822 and ASTM D3800 [43,44].

[c] Provided by manufacturer.

3.2.2 Sample preparation and CO_2 curing process

Dogbone-shape specimens (Figure 3-3) were cast for the uniaxial-tension test, the 50x50x50 mm^3 cubes for the compression test, and 305x76x38 mm^3 beams for the matrix toughness test. Single fiber pull-out specimens were also fabricated (Figure 3-4). There were two curing conditions for each mix proportions: air curing of normal hydration process for non-carbonated reference and carbonation curing for carbonated specimens. All samples under both curing conditions were de-molded after 18 hours until hardened. Air-cured specimens were cured in normal room conditions with $23 \pm 2^{\circ}C$ temperatures and $60 \pm 5\%$ relative humidity. Carbonation-cured specimens were subjected to 4 hours fan drying process to remove the pore water in the mixtures to enhance the CO_2 diffusion [45]. Then, fan-dried specimens were cured under 5 bar bone dry CO_2 (99.8% purity) at room conditions ($23 \pm 2^{\circ}C$) for 24 hours [26]. Additional cube specimens were cut to measure the carbonation depth and CO_2 uptake right after the carbonation-curing process, i.e., at the age of 48 hours. The mechanical testing for all the other specimens, both air-cured and carbonation-cured, was conducted at 7 days and 28 days.

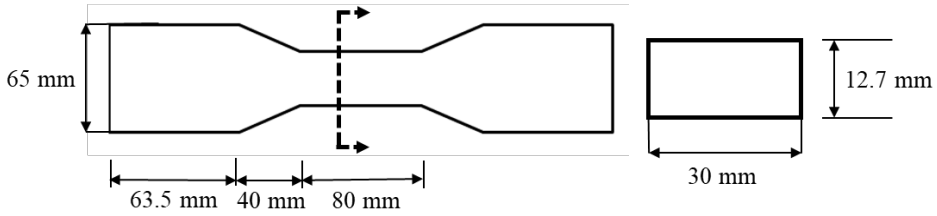

Figure 3-3. Dimension of the dogbone-shape specimens for the uniaxial tension test.

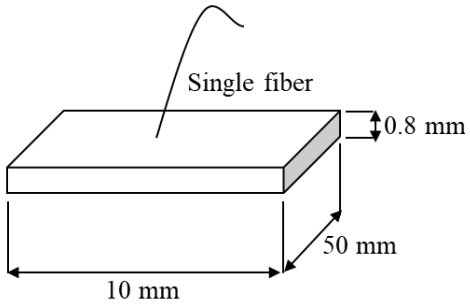

Figure 3-4. Dimension of single fiber pull-out specimens.

3.3. Test methods

3.3.1 Carbonation depth and CO_2 uptake

Phenolphthalein indicator was used to determine the carbonation depth for the carbonation-cured samples. The specimens were saw-cut after carbonation, and the phenolphthalein solution was sprayed to measure the uncolored thickness as carbonation depth.

CO_2 uptake was measured from specimens' mass loss during the decarbonation process of heating, i.e., TGA. The cube specimens were sliced into 5 mm thick layers and ground into powder. TGA was conducted from room temperature to 1100 ˚C. The decomposition temperature for calcite ($CaCO_3$) ranges from $550 - 950^{\circ}C$ [46–48]. Hence, the mass difference between $550 - 950^{\circ}C$ is the mass loss from the release of CO_2 and can be calculated using Equation (3-1) [26]. Each 5 mm thick piece was measured, and the CO_2 uptake per cement mass throughout the cross-section can be obtained, as shown in Figure 3-5.

$$\text{CO}_2 \text{ uptake } (\%) = \frac{(m_{550} - m_{950}) - (M_{550} - M_{950})}{m_{cement}} \times 100\% \quad (3\text{-}1)$$

where m_{550} and m_{950} are the masses of carbonation-cured samples at 550 and 950 ˚C, M_{550} and M_{950} are the masses of air-cured samples at 550 and 950 ˚C, and m_{cement} is the mass of the cement sample. Besides the CO_2 uptake estimation, to investigate the effect of introducing sisal fiber into the mixture, water loss during the enforced drying process was also considered and can be estimated by Equation (3-2):

$$\text{Water loss } (\%) = \frac{m_w - m_d}{m_{cement}} \times 100\% \quad (3\text{-}2)$$

where m_w and m_d are the masses of samples before and after 4 hours drying process.

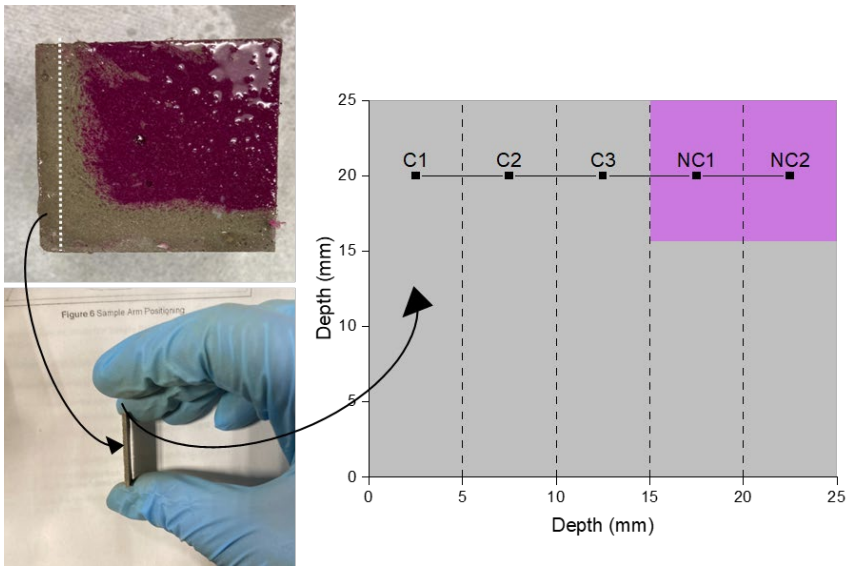

Figure 3-5. Typical sample preparation of TGA for CO_2 uptake estimation.

3.3.2 Mechanical tests

Uniaxial tension test and compression test were conducted after 7 days and 28 days of curing. A 100 KN capacity Material Testing Systems (MTS) loading frame was used for the uniaxial tension test in this study. Dogbone specimens were loaded under displacement control at a rate of 0.5 mm/min following JSCE [49]. Two linear variable displacement transducers (LVDT) were placed on the samples with a gauge length of 80 mm. A Forney loading machine was used for the compression test. 50x50x50 mm^3 cubes were conducted with a 0.5 MPa/s loading rate according to ASTM C109 [50].

Matrix toughness (K_m) of the ECC matrix was measured following the ASTM E399 [51], with a pre-notch (notch to height ratio = 0.4, i.e., 15.2 mm in this study) 305x76x38 mm^3 beam specimen. The experiment was conducted under displacement control at a rate of 0.5 mm/min. Detailed matrix toughness test setup and dimensions are shown in Figure 3-6.

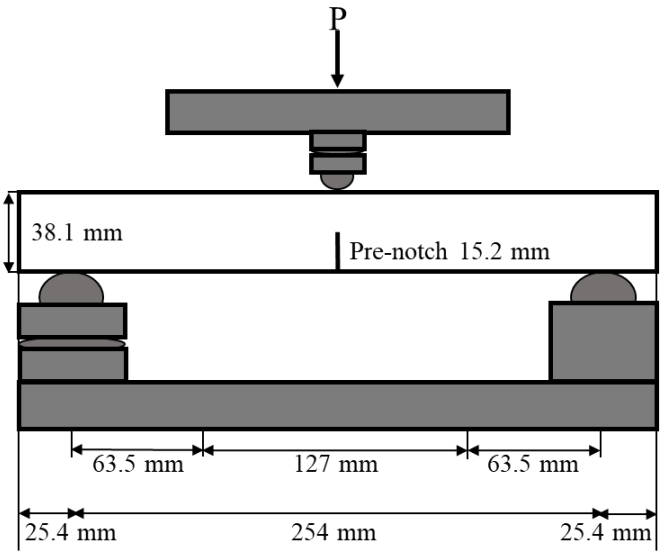

Figure 3-6. Matrix toughness test setup.

3.3.3 Single fiber pull out test

An Instron Model 8000 test system with a 5 N load cell was used for the single fiber pull out test to evaluate the fiber/matrix bridging and interfacial bond between fibers and cementitious matrix. WPS/sisal fibers were glued on the steel plate, connected to the actuator, and pulled at a constant loading rate of 0.5 mm/min, as shown in Figure 3-7 [52]. The load-displacement curves

for the single fiber, chemical debonding energy, G_d, frictional bond strength, τ_0, and slip-hardening coefficient β were determined following the method of [53,54].

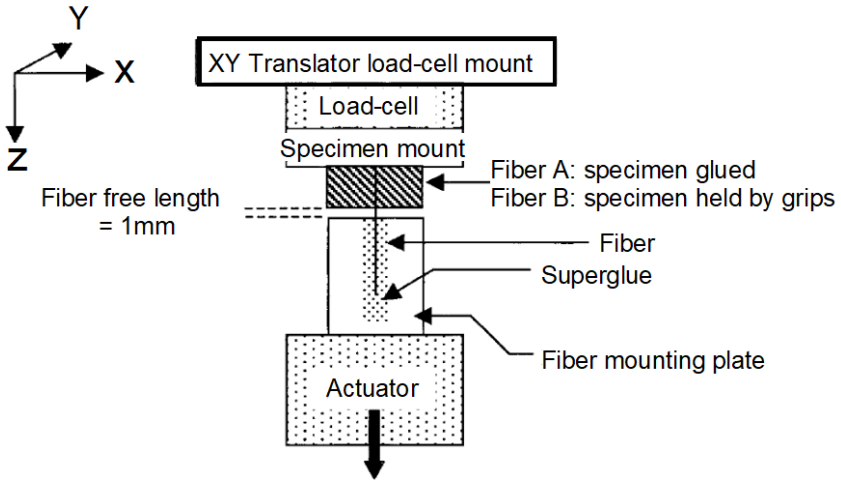

Figure 3-7. Single fiber pull-out test setup [52].

3.3.4 Pseudo-strain-hardening (PSH) indices from micromechanical modeling

The fiber bridging capacity and complementary energy J_b' can be determined using fiber/matrix interfacial bond and matrix properties obtained from 3.3.2 as inputs based on the ECC micromechanical model [8,55]. Then, PSH indices can be determined by Equation (3-3) and Equation (3-4), which can be used to evaluate the strain-hardening performance of ECC.

$$PSH_{energy} = \frac{J_b'}{J_{tip}} \tag{1-3}$$

$$J_{tip} = \frac{K_m^2}{E_m} \tag{3-4}$$

where E_m is the Young's modulus of the matrix, and K_m is the matrix toughness.

3.4. Results and discussion

3.4.1 Water loss and CO_2 uptake estimation

Sisal fibers serve as conduits for water and CO_2 during the enforced drying and carbonation curing process. Figure 3-8 and Figure 3-9 show the water loss and CO_2 uptake for the OPC cube specimens with sisal fiber content of 0.0% to 1.5%, i.e., OPC-2S00 to 2S15, for various sisal fiber contents. The average water loss without any sisal fiber is around 20.42%, and up to 25.68% for 1.0% of sisal fiber added (26% increase). The average CO_2 uptake (Figure 3-9), obtained from the TGA curves (Figure 3-10), increased from 17.75% to 18.23%, 20.67%, and 21.25% (3%, 16%, and 20% increase, respectively) when 0.5%, 1.0%, and 1.5% of sisal fiber were added. This finding validates the hypothesis that hollow sisal fiber can be effective as conduits for CO_2 penetration into the precast product during carbonation process.

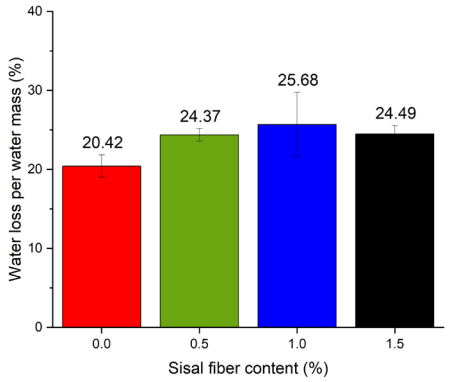

Figure 3-8. Water loss for OPC-WPE-sisal fiber ECC by mass loss.

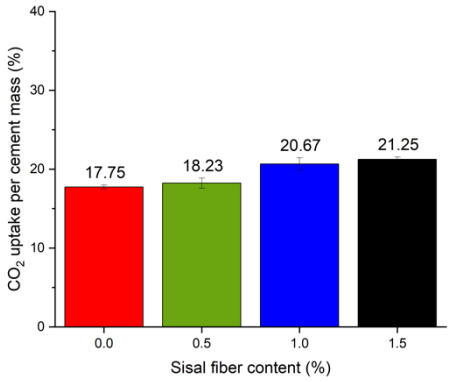

Figure 3-9. CO_2 uptake per cement mass for OPC-PE-Sisal fiber ECC by TGA.

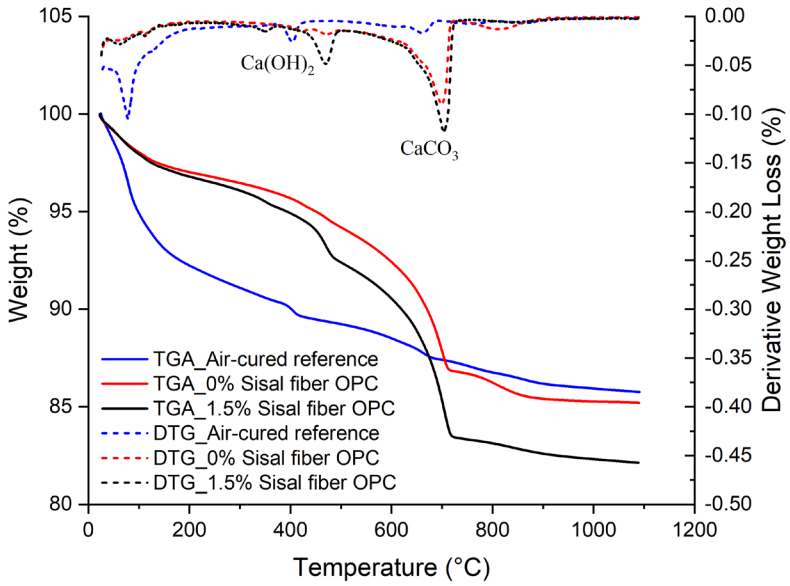

Figure 3-10. Typical TGA &DTG for OPC-PE-sisal fiber ECC

To further investigate the role of sisal fiber during carbonation curing, CO_2 uptake from the surface to core was measured for both air-cured and carbonation-cured samples (Figure 3-11). There is a drastic decrease of CO_2 uptake when the depth exceeds 15 mm for the 0% sisal fiber sample, while the samples with sisal fibers can still maintain around 3.31% of CO_2 uptake at 25-30 mm depth. It is reasonable that there is an upper limit for CO_2 uptake for the 0% sisal fiber sample since the carbonation process is governed by the diffusion of CO_2 through the surface into the matrix [56,57]. The formation of $CaCO_3$ during the carbonation process densifies the matrix, which makes it harder for CO_2 to further penetrate thorough the sample [26]. The tubular pillar geometry of sisal fiber channels the ingress of CO_2 through the densified cement matrix and lets CO_2 diffuse deeper, leading to a 16% increase of CO_2 uptake for 1.0% sisal fiber ECC. The carbonation patterns for the cross-section of the specimens, as revealed by the phenolphthalein indicator, also support this observation. As shown in Figure 3-12 (c) and (f), where the transparent color was observed between the interface of sisal fiber and cement matrix, indicating the formation of precipitates ($CaCO_3$) along the sisal fiber for the carbonation-cured specimens. With higher sisal fiber content, the transparent color area increases more (Fig. 1(f)). This phenomenon could not be found in the air-cured samples (see Figure 3-12(b) and (c)).

Figure 3-13(a) shows the CO_2 uptake for the LC3-ECC, i.e., LC3-2S10. The average CO_2 uptake increased from 16.25% to 19.43% (20% increase) when the sisal fiber content was increased from 0% to 1%. Also, Figure 3-13(b) indicates the average CO_2 uptake for WFS-ECC, i.e., WFS-2S10, is comparable to normal silica sand ECC. The slightly increased CO_2 uptake from 20.67% to 21.14% (2% increase) may be caused by the larger particle size of the WFS, as shown in Figure 3-2.

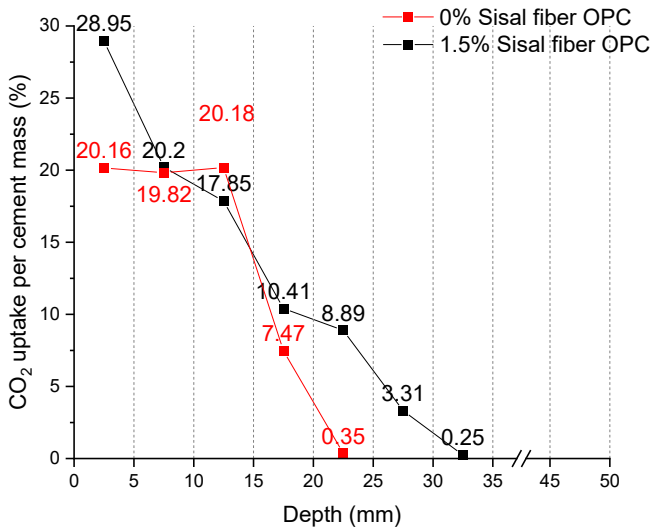

Figure 3-11. CO_2 uptake for OPC-PE-sisal fiber ECC among different depth

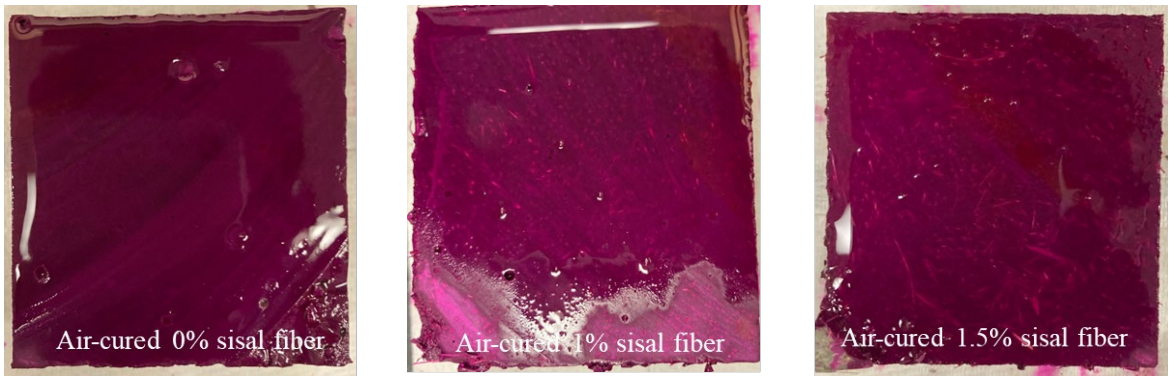

Figure 3-12. Carbonation depths and patterns as revealed by the phenolphthalein indicator, for air-cured (a) 0% sisal fiber, (b) 1% sisal fiber, (c) 1.5% sisal fiber; and carbonation-cured (d) 0% sisal fiber, (e) 1% sisal fiber, (f) 1.5% sisal fiber ECC.

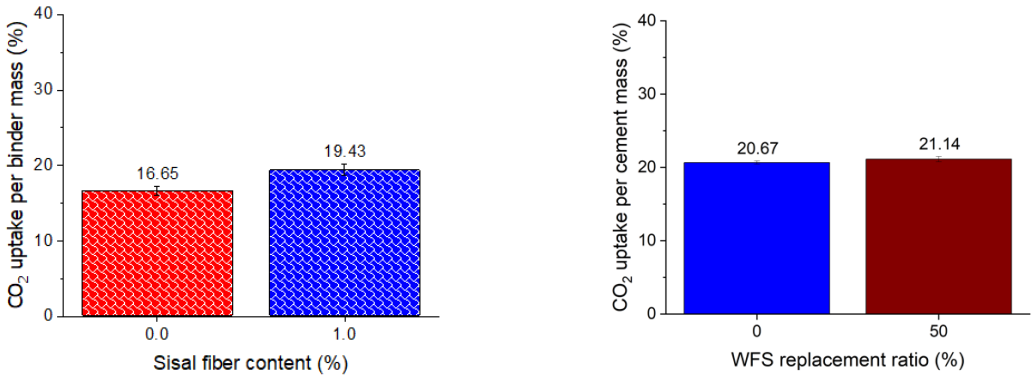

Figure 3-13. CO_2 uptake for (a) LC3-PE-sisal fiber ECC, (b) OPC-PE-sisal fiber WFS ECC by TGA.

3.4.2 Micromechanical properties

3.4.2.1 Matrix properties

Table 3-4 illustrates the matrix properties for OPC-PE-sisal fiber ECC, including Young's modulus E_m and fracture toughness K_m. Carbonation curing increased E_m from 22.2 GPa to 25.8 GPa (16% increase). Carbonation curing makes the matrix stiffer by microstructural densification [58] through the $CaCO_3$ precipitation. A similar densification effect has been reported for conventional cement paste [59,60] and ECC after carbonation curing [26]. In contrast, K_m diminished from 0.45 to 0.41 (9% reduction) for the carbonation-cured sample. The reduction suggests a slight increase in the brittleness of the matrix following carbonation curing. This matrix embrittlement effect is beneficial to enhancement of the PSH indices (see Equation (3-3) and (3-4)).

Table 3-4. Matrix properties for OPC-PE-sisal fiber ECC.

Curing condition	E_m (GPa)	K_m (MPa$\sqrt{m}$)
Air-cured	22.2 ± 1.31	0.45 ± 0.01
Carbonation-cured	25.8 ± 0.72	0.41 ± 0.01

3.4.2.2 Fiber/matrix interface

From a micromechanics-based viewpoint, excessively low resistance to fiber pull out and excessively high resistance that led to fiber rupture are the primary factors that limit the performance of ECC [61,62]. Therefore, it is crucial to understand the effect of carbonation curing on the fiber/matrix interface properties.

Table 3-5 lists the WPE fiber/matrix interfacial bond, including chemical bond G_d, frictional bond τ_0, and slip hardening coefficient β for air-cured and carbonation-cured ECC. Five single fiber pull-out specimens for each air-cured and carbonation-cured were measured. Carbonation curing increased the average G_d from 0.39 J/m^2 to 0.68 J/m^2 (74% increase) and the average τ_0 from 0.98 MPa to 1.45 MPa (48% increase), suggesting a more substantial fiber bridging capacity. The strengthening between fiber and matrix by carbonation curing makes the hydrophobic WPE fibers more resistant to debonding and pullout failure under tensile loading,

leading to higher strength and ductility than air-cured ECC. The carbonation-induced increase of interfacial bond between fiber and matrix was also reported in a previous PVA ECC study [26] and is attributed to the deposition of $CaCO_3$ along the fiber/matrix interface. Carbonation curing marginally increased β from 0.5 to 0.53 (6% increase), indicating the strain hardening process was not considerably influenced. In contrast, the average G_d and τ_0 increased from 0.01 to 0.05 J/m^2 and 0.49 to 0.92 MPa, respectively for sisal fiber/matrix interface (Table 3-6). Nevertheless, the interfacial bond after carbonation curing remained low. It can be anticipated that sisal fiber will encounter severe slippage and pull-out problems during tensile loading. This statement will be verified in later section 3.4.3.2.

Table 3-5. PE fiber/matrix interfacial bond for carbonation-cured and air-cured ECC.

Curing condition	Chemical bond G_d (J/m^2)	Frictional bond τ_0 (MPa)	Slip hardening coefficient β
Air-cured	0.39 ± 0.16	0.98 ± 0.20	0.50 ± 0.09
Carbonation-cured	0.68 ± 0.14	1.45 ± 0.26	0.53 ± 0.22

Table 3-6. Sisal fiber/matrix interfacial bond for carbonation-cured and air-cured ECC.

Curing condition	Chemical bond G_d (J/m^2)	Frictional bond τ_0 (MPa)
Air-cured	0.01 ± 0.00	0.49 ± 0.14
Carbonation-cured	0.05 ± 0.04	0.92 ± 0.11

Strain hardening indices for both air-cured and carbonation-cured ECC are greater than 1 (Table 3-7), indicating that strain hardening criteria are satisfied for both curing conditions [8]. However, the PSH_{energy} decreased from 37.31 to 21.21 (43% decrease) after carbonation curing, which may lead to a reduced strain-hardening potential for ECC and need to be further confirmed.

Table 3-7. Strain-hardening indices for OPC-ECC.

Curing condition	J_b'(J/m^2)	J_{tip}(J/m^2)	PSH_{energy}
Air-cured	340.33 ± 28.7	9.12 ± 0.77	37.31 ± 6.32
Carbonation-cured	138.19 ± 24.7	6.52 ± 0.41	21.21 ± 5.13

3.4.3 Mechanical performance

3.4.3.1 Compressive strength

The compressive strength of the air-cured and carbonation-cured OPC-ECC are presented in Figure 3-14. With increasing amount of sisal fiber from 0% to 1%, the compressive strength of the air-cured OPC-ECC decreased from 34.3 MPa to 27.7 MPa (19% decrease) at 7 days and from 44.3 MPa to 40.9 MPa (8% decrease) at 28 days due to the artificial flaws induced by adding the sisal fiber. Similarly, the compressive strength of the carbonation-cured ECC decreased when the sisal fiber was increased from 0% to 1%; from 38.9 MPa to 38.5MPa (1% decrease) and 52.8 MPa to 47.6 MPa (10% decrease) at 7 days and 28 days, respectively. However, there is a significant compressive strength drop for 1.5 % sisal fiber ECC (OPC-2S15). The compressive strength decreased from 38.9 MPa to 30.7 MPa (21% decrease) and 52.8 MPa to 36.4 MPa (31% decrease) at 7 days and 28 days. The high amount of fiber usage (2% WPE + 1.5% sisal fiber for a total 3.5% of volume fraction) led to the compressive strength reduction for 1.5% sisal fiber ECC, suggesting a problem with fiber dispersion difficulty.

Carbonation curing increased OPC-ECC's compressive strength from 34.3 MPa to 38.9 MPa (13% increase) for 0% sisal fiber added and 27.7 MPa to 38.5 MPa (39% increase) for 1% sisal fiber added at 7days. Similarly, the compressive strength increased from 44.3 MPa to 52.8 MPa (19% increase) and 40.9 MPa to 47.6 MPa (14%) for 0% and 1% sisal fiber ECC at 28 days. The increased compressive strength is due to the microstructural densification by the $CaCO_3$ precipitation for the carbonation-cured OPC-ECC. The strength gain by carbonation curing compensates for the strength loss by the addition of sisal fiber, suggesting a comparable compressive strength for carbonation-cured 1% sisal fiber to air-cured 0% sisal fiber OPC-ECC (47.6 MPa and 44.3 MPa).

Distinct from the strength gain of OPC-ECC after carbonation curing, the compressive strength of carbonation-cured LC3-ECC slightly decreased, as shown in Figure 3-15 (a) from 32.9 MPa to 31.6 MPa (4 % decrease). This could be attributed to the lower OPC content in addition to the calcium hydroxide (CH) competition between carbonation curing and the pozzolanic effect of MK for LC3 (comprising 55% OPC, 30% MK, 30% LS) [63]. Even without carbonation curing, LC3 consumes nearly all of CH after 3 days of hydration [16] Meanwhile, carbonation curing requires CH to react with CO_2, leading to lesser CH content and resulting in a lack of pozzolanic effect. Figure 3-15 (b) shows that compressive strength decreased for WFS-ECC, which is caused by the larger particle size and impurities intrinsic in WFS [64].

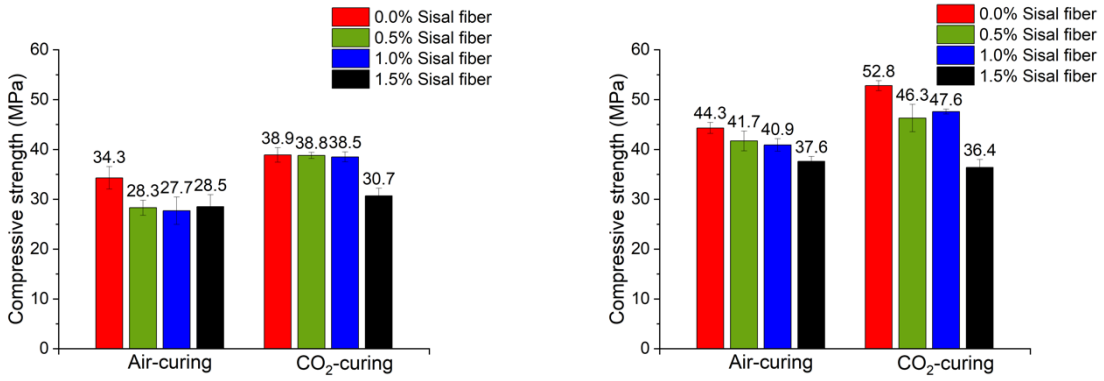

(a) (b)

Figure 3-14. Compressive strength for 2% WPE OPC-ECC at (a) 7 days, and (b) 28 days.

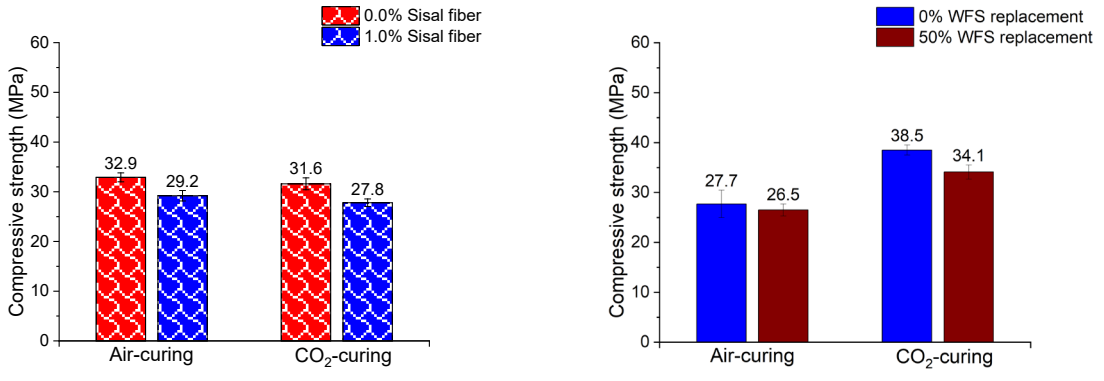

(a) (b)

Figure 3-15. Compressive strength of 1% sisal fiber (a) LC3-ECC, and (b) WFS-ECC.

3.4.3.2 Tensile performance

Figure 3-16 shows the tensile stress-strain curves for 0% WPE with 2% sisal fiber ECC, i.e., OPC-0S20. There is no strain-hardening behavior, and the specimen fails with a single crack. All sisal fibers were pulled out rather than ruptured during the tensile test, indicating low interfacial bond between the sisal fiber and the matrix, consistent with the results in section 3.4.2.2.

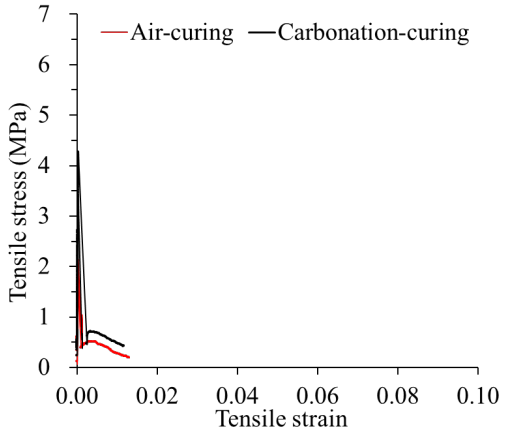

Figure 3-16. Tensile stress-strain relationship for OPC-0S20, 0% WPE and 2% sisal fiber, ECC.

The representative tensile stress-strain relationships for OPC-ECC are shown in Figure 3-17., and the more detailed curves are shown in Figure 3-18 and Figure 3-19. The key tensile parameters, including average first crack strength, average ultimate strength, and average tensile strain, are summarized in Table 3-8 and Table 3-9. The 1st crack strength of OPC-ECC decreased with the increase of sisal fiber content due to the sisal fiber-induced artificial defects. Specifically, the 1% sisal fiber OPC-ECC reduced the 1st crack strength of 0% sisal fiber OPC-ECC from 2.61 MPa to 2.52 MPa (3% decrease), 4.00 MPa to 3.72 MPa (7% decrease) for air-cured and carbonation-cured samples at 7 days, respectively. The reduction of 1st crack strength benefits the multiple crack initiation, leading to more multiple crack formations and higher ultimate tensile strain by 81% increase and 13% increase for air-cured and carbonation-cured OPC-ECC. However, when the content of sisal fiber exceeded 1%, i.e., 1.5% of sisal fiber, the ultimate tensile strain decreased drastically from 8.98% to 3.68% (59% decrease) for air-cured and 7.47% to 5.06% (32% decrease) for carbonation-cured, as a result of poor fiber dispersion.

Carbonation curing increased the 1st crack strength of the specimens due to the densification of the matrix, which impeded the crack initiation and reduced the tensile ductility of

ECC. However, as shown in section 3.4.2.2, the fiber/matrix interfacial bond increased significantly after carbonation curing, i.e., 74% for G_d and 48% for τ_0, compensating for the disadvantage of 1st crack strength gain after carbonation curing. Therefore, the average ultimate strain was still enhanced for carbonation-cured 1% sisal fiber OPC-ECC by 13% and 47% at 7 and 28 days. The maximum strength also increased by 17%. The improved tensile performance of carbonation-cured ECC is consistent with the results in [16,26]. The addition of sisal fiber and carbonation curing results in a tradeoff of artificial flaws, increased interfacial bond, and fiber dispersion.

In contrast, carbonation curing decreased the ultimate strength and tensile strain of LC3-ECC (Figure 3-20(a)). The lack of pozzolanic effect due to the competition of CH in the early ages of hydration during the carbonation curing process led to the ultimate strength decrease. The average ultimate strength and strain for 1% sisal fiber LC3-ECC still exceeded 3.98 MPa and 6.05%, showing a promising tensile performance comparable to previous LC3-ECC studied [14,16]. Figure 3-20(b) presents the similar ultimate strength and increased tensile strain of WFS-ECC compared to silica sand ECC. The ultimate strain for air-cured and carbonation-cured 1% sisal fiber WFS-ECC is 9.95% and 10.73%, respectively, exceeding 8.98% and 7.47% of strain for silica sand ECC.

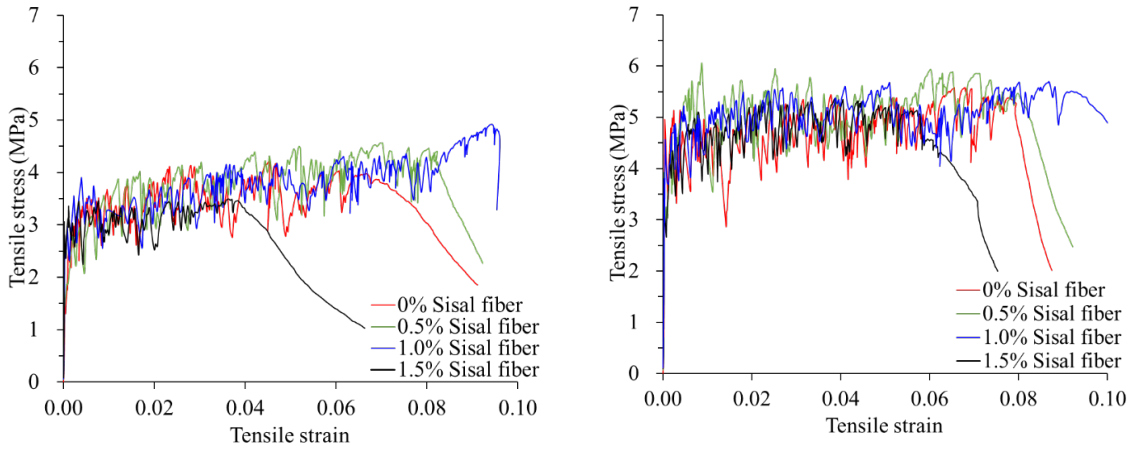

Figure 3-17. Representative tensile stress-strain relationship for 2% WPE (a) air-cured, (b) CO_2-cured OPC-ECC at 7 days.

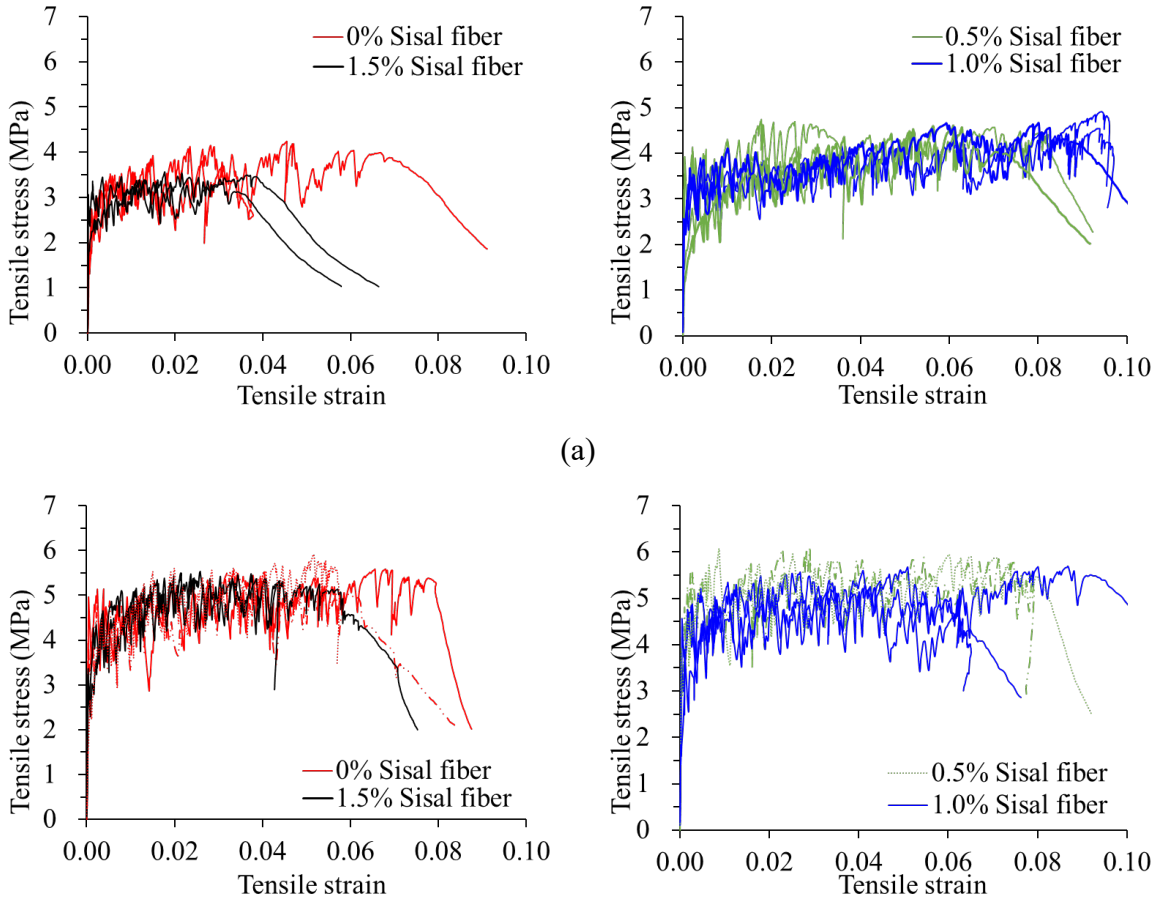

(a)

(b)

Figure 3-18. Tensile stress-strain relationship for 2% WPE (a) air-cured, (b) CO_2-cured OPC-ECC at 7 days with different contents of sisal fiber.

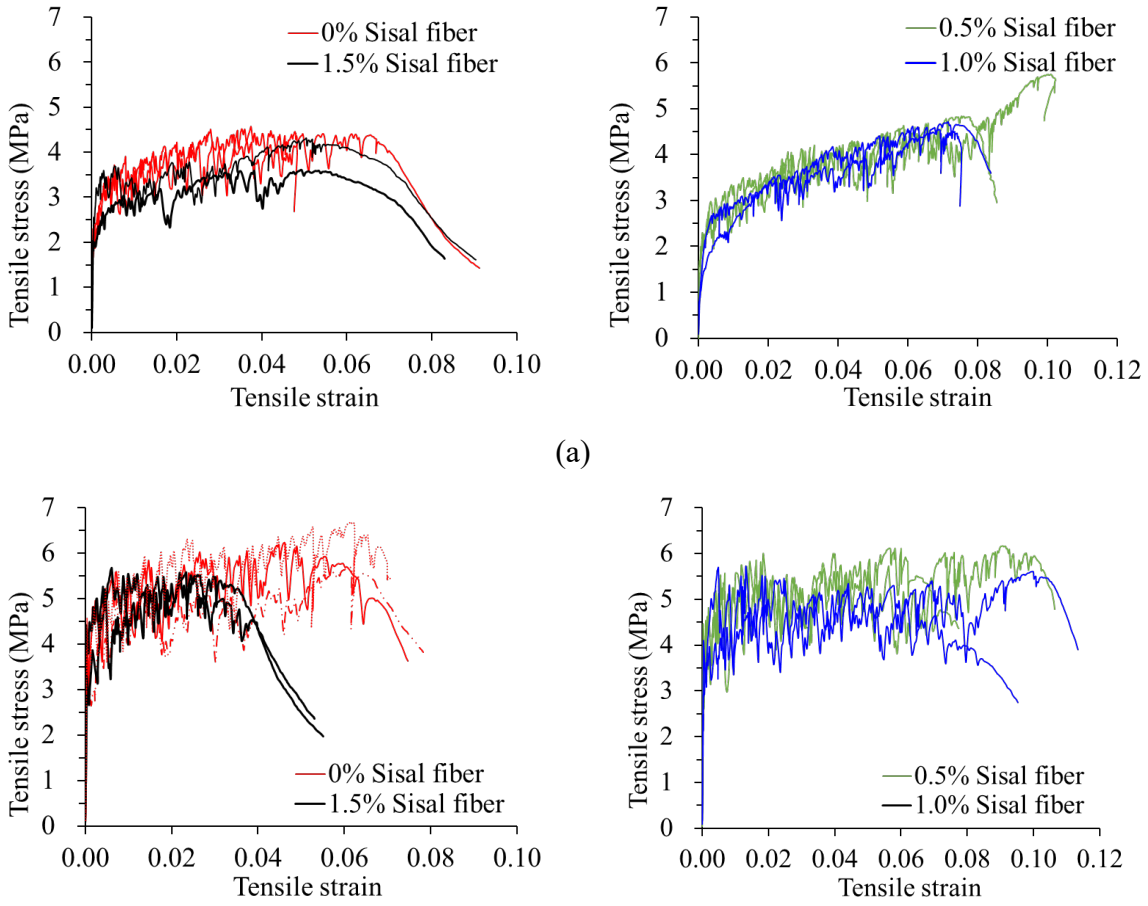

Figure 3-19. Tensile stress-strain relationship for 2% WPE (a) air-cured, (b) CO_2-cured OPC-ECC at 28 days with different contents of sisal fiber.

Table 3-8. Tensile properties of OPC-ECC at 7 days.

Sisal fiber content	Curing condition	Average 1st crack strength	Average ultimate strength	Average ultimate strain
0%	Air-cured	2.61 ± 0.13	4.03 ± 0.17	$4.95 \pm 0.19\%$
0.5%		2.58 ± 0.28	4.63 ± 0.08	$7.23 \pm 1.92\%$
1.0%		2.52 ± 0.03	4.71 ± 0.15	$8.98 \pm 0.68\%$
1.5%		2.47 ± 0.04	3.47 ± 0.02	$3.68 \pm 0.12\%$
0%	Carbonation-cured	4.00 ± 0.16	5.69 ± 0.16	$6.64 \pm 0.98\%$
0.5%		3.68 ± 0.24	6.09 ± 0.26	$7.31 \pm 0.18\%$
1.0%		3.72 ± 0.34	5.53 ± 0.19	$7.47 \pm 1.23\%$
1.5%		2.79 ± 0.43	5.45 ± 0.08	$5.06 \pm 0.73\%$

Table 3-9. Tensile properties of OPC-ECC at 28 days.

Sisal fiber content	Curing condition	Average 1st crack strength	Average ultimate strength	Average ultimate strain
0%	Air-cured	2.72 ± 0.09	4.48 ± 0.08	$5.63 \pm 0.90\%$
0.5%		2.45 ± 0.14	5.29 ± 0.46	$8.95 \pm 1.15\%$
1.0%		2.47 ± 0.20	4.63 ± 0.08	$7.56 \pm 0.04\%$
1.5%		2.39 ± 0.03	3.96 ± 0.36	$5.41 \pm 0.22\%$
0%	Carbonation-cured	3.83 ± 0.17	6.19 ± 0.40	$6.12 \pm 0.41\%$
0.5%		3.87 ± 0.15	6.14 ± 0.02	$8.62 \pm 1.28\%$
1.0%		3.53 ± 0.08	5.72 ± 0.02	$8.98 \pm 1.33\%$
1.5%		3.37 ± 0.09	5.62 ± 0.05	$3.74 \pm 0.17\%$

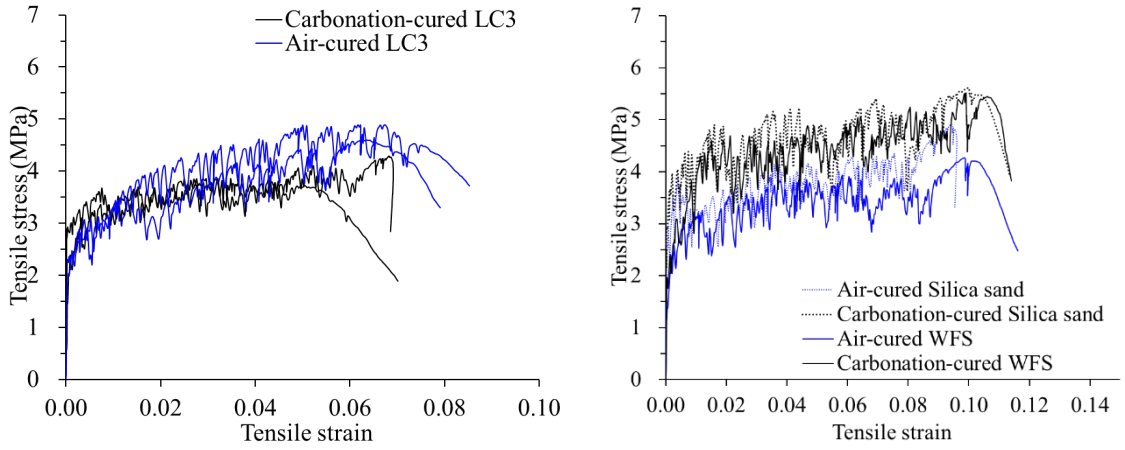

(a) (b)

Figure 3-20. Tensile stress-strain relationship for 1% sisal fiber (a) LC3-ECC, and (b) WFS-ECC.

3.4.4 Crack patterns and crack width distribution

The 0% WPE 2% sisal fiber sample, i.e., OPC-0S20, shows only one localized failure crack, as shown in Figure 3-21 and Figure 3-22. Shows the representative crack patterns for 0% and 1% sisal fiber OPC-ECC under both curing conditions at failure. All OPC-ECC with 2%WPE present multiple cracks irrespective of the contents of sisal fiber. Adding more sisal fiber contributed to more crack numbers at failure with comparable crack width, suggesting the benefits of adding sisal fiber that enhance the ECC's tensile ductility.

Carbonation curing also improved the crack control capacity of ECC. Figure 3-23 presents the crack width distribution for 1% sisal fiber carbonation-cured and air-cured OPC-ECC with silica sand and WFS. Carbonation curing leads to more crack formations and smaller crack width. The average cracks width for 1% sisal OPC-ECC and WPS-ECC decreased from 101.5 μm to 69.7 μm (31% decrease) and 92.6 μm to 69.0 μm (25% decrease), respectively. More tiny cracks below 80 μm was observed and there were no cracks larger than 160 μm for carbonation-cured specimens.

Figure 3-21. Representative crack patterns for OPC-0S20, 0% WPE and 2% sisal fiber, ECC under ultimate tensile strain.

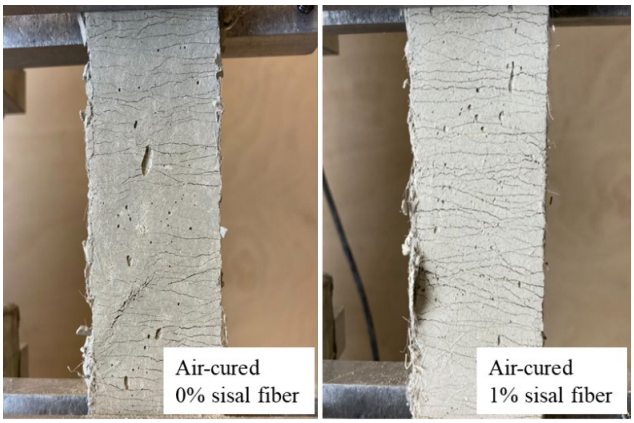

(a)

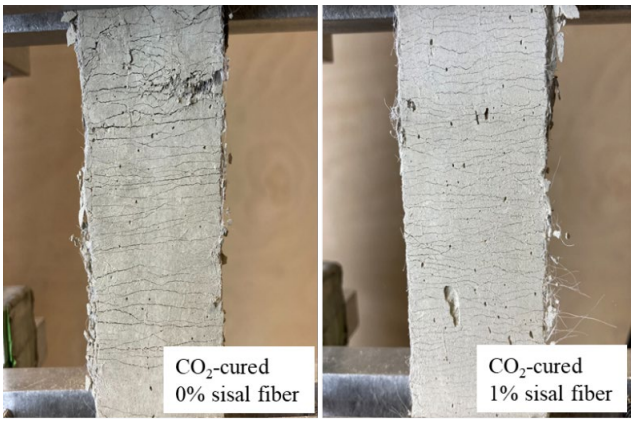

(b)

Figure 3-22. Representative crack patterns for 0% and 1% sisal fiber of (a) air-cured and (b) carbonation-cured OPC-ECC under ultimate tensile strain.

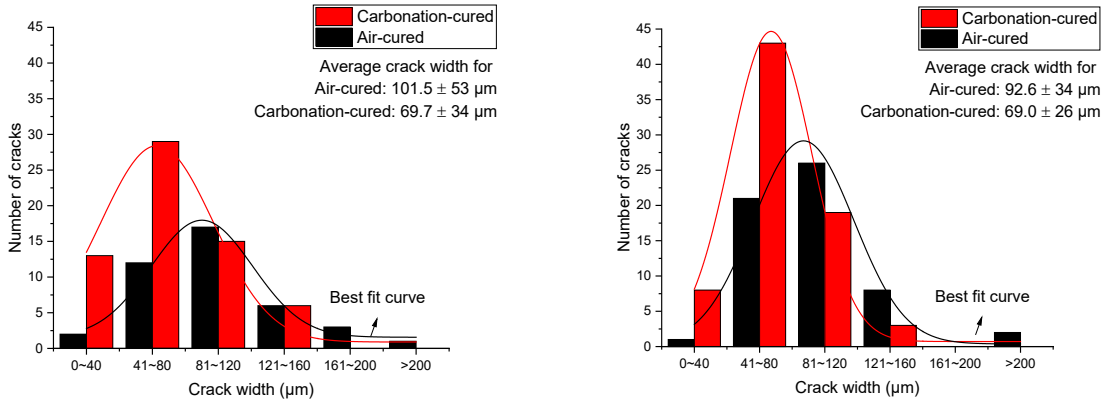

(a) (b)

Figure 3-23. Crack width distribution for 1% sisal fiber carbonation-cured and air-cured OPC-ECC with (a) silica sand and (b) WFS.

3.4.5 Sustainability of WPE-sisal fiber ECC

To evaluate the sustainability of the ECC, the embodied energy, embodied carbon footprint, and material costs, representing the total energy consumption, CO_2 emission, and costs during the manufacturing process of the materials, were assessed as Material Sustainability Indicators (MSIs) [11]. Table 3-10 lists the MSIs, including all the major ingredients for producing ECC. It should be noted that the material cost may fluctuate. The OPC type 1L used in this study results in up to 10% reduction in carbon footprint compared to OPC type 1 listed in Table 3-10. According to Michigan Concrete Association and literature [65]. The fly ash, WPE, and WFS in this study were assumed to be industrial waste streams with a net zero embodied energy consumption and CO_2 footprint. It should be noted that the costs were the price of each ingredient ranging from 2018 to 2020, likely to fluctuate due to inflation in the future.

Conventional concrete, typical M45-ECC, MgO-based ECC, high volume fly ash (HVFA) ECC, and LC3-PP-ECC were used as a benchmark to evaluate the MSIs of low-carbon ECC in this study as shown in Figure 3-24 and Figure 3-25, which also illustrates the CO_2 analysis for each ingredient based on the lower bounds of the variation, i.e., symbol A and symbol B in Fig. 5 represents the lower bounds of embodied carbon footprint of traditional concrete and LC3-2S10 in Fig. 4, respectively. By carbonation-curing and replacing conventional PE fiber by WPE, the

embodied energy and carbon footprint (3.23 GJ/m^3 and 368 kg CO_2/m^3) of OPC-2S10 were found to decrease compared to M45-ECC (6.37 GJ/m^3 and 606 kg CO_2/m^3), while still higher than concrete (2.61 GJ/m^3 and 341 kg CO_2/m^3). Further replacing the OPC with LC3, i.e., LC3-2S10, significantly lowered the embodied CO_2 footprint for ECC. The average embodied CO_2 footprint of LC3-2S10 decreased to 169 kg CO_2/m^3 compared to concrete (341kg CO_2/m^3) and M45-ECC (606 kg CO_2/m^3) with a 50% and 72% reduction, respectively, since cement contributed to the primary CO_2 emissions of ECC. The costs of LC3-2S10 and OPC-2S10 decreased to 76 and 80 USD/m^3 compared to M45-ECC (430 USD/m^3) since the main costs of ECC is from fiber (see Figure 3-25), i.e., PVA fiber in M45 (345 USD/m^3) and PP fiber in LC3-PP mixture (115 USD/m^3). Substituting conventional PE (675 USD/m^3) with WPE reduces the fiber cost drastically to 9.6 USD/m^3, leading LC3-2S10 and OPC-2S10 ECC (76 and 80 USD/m^3 respectively) to be competitive with traditional concrete (89 USD/m^3). The costs of WFS-2S10 further decreased to 60 USD/m^3, which is 33% lower than traditional concrete. However, the embodied energy and carbon footprint of WFS-2S10 remained higher than concrete.

Taking the pavements construction as an example, among the total of 2.9 million miles of paved road in U.S., about 5% is paved with concrete [66] consuming 22 million tons of concrete pavements [67]. If all concrete pavements were replaced with LC3-ECC in this study, the consumption of the WPE is 0.2 million tons, which is about 10% of annual ALDFG waste. Meanwhile, the embodied carbon footprint and costs will remain comparable with the conventional concrete and contribute to mitigating the environmental and economic impacts caused by marine waste. However, it should be noted that this WPE-sisal fiber ECC is only applicable to pre-cast pavements for which carbonation curing is suitable.

Table 3-10.The embodied energy, carbon emission, and material cost for ingredients ECC production.

Component	Embodied energy (GJ/t)	CO_2 emission (kg/t)	Cost (USD/t)
OPC type 1	4.8-5.5[a]	870-940[b]	48[c]
LC3[c]	4	550	40.3
FA	0	0	25.6[c]
Silica sand[c]	0.067	23.3	63.9
WR[c]	35	1667	1211
PE fiber	73-116[d]	2000[d]	35200[e]
Sisal fiber	18[f]	170[f]	682

[a] Data from [68].

[b] Data from [69,70].

[c] Data from [14,16,71], where CO_2 emission of LC3 can also be presented in 1344-1562 kg/m^3.

[d] Data from [12,22].

[e] Data from [72].

[f] Data from [35].

(a)

(b)

(c)

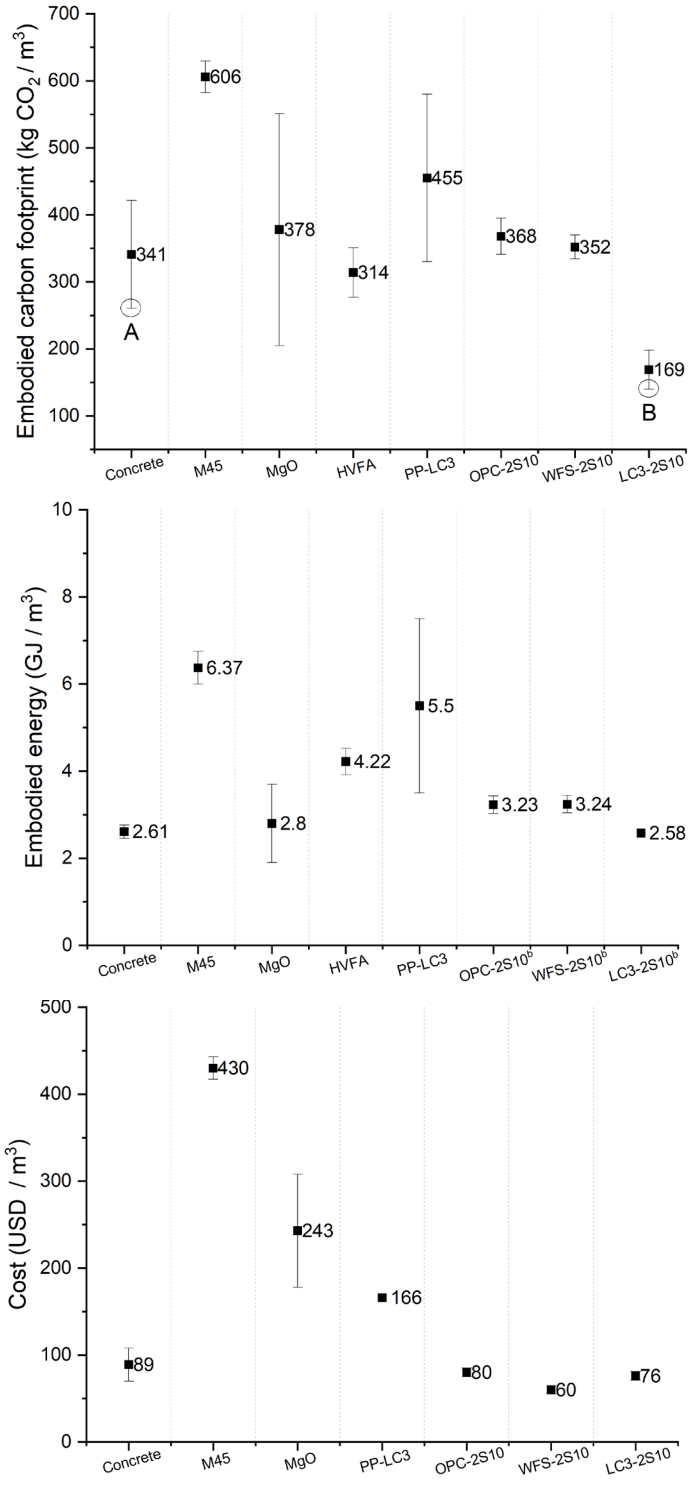

Figure 3-24. The (a) embodied carbon footprint, (b) material embodied energy, and (c) material costs of conventional concrete, OPC-2S10, LC3-2S10, WFS-2S10, and other common ECC [12].

(a)

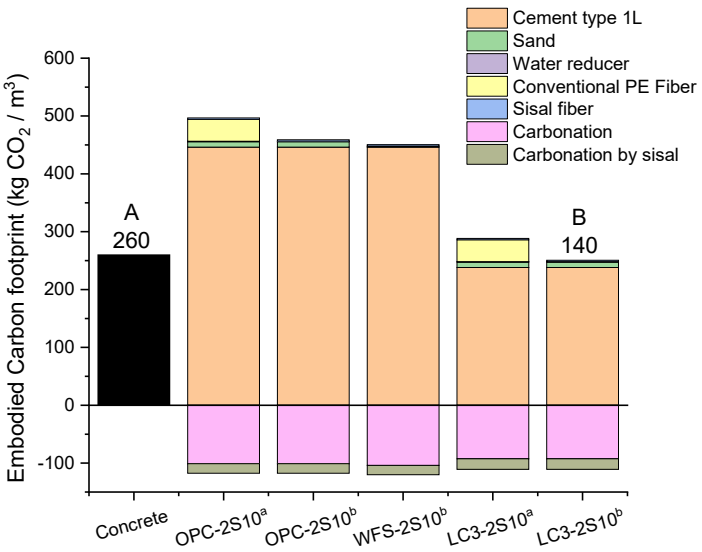

(b)

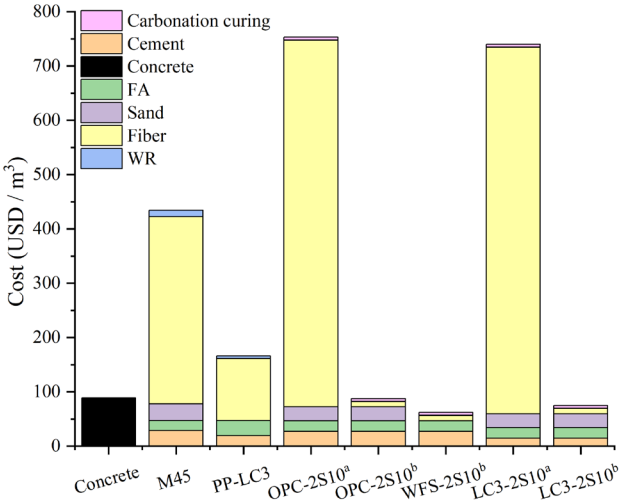

Figure 3-25. Contributions of (a) embodied carbon footprint and (b) costs by ingredients of OPC-2S10[ab], LC3-2S10[ab], and WFS-2S10[b]. [a] with conventional PE fiber, [b] with WPE

3.5. Conclusions

A sustainable low-carbon ECC is developed using industrial waste, renewable plant fiber, and carbonation curing. The repurposed materials include waste high modulus polyethylene (WPE) fiber from the marine industry and waste foundry sand. The developed carbonation-cured WPE-sisal fiber ECC has lower embodied energy, carbon, and cost than concrete and other grades of ECC while maintaining the unique high tensile ductility of the ECC family of composite materials. Meanwhile, the repurposing of WPE also serves as a potential solution for reducing marine plastic waste.

Specifically, the embodied carbon of the developed ECC was found to reduce up to 50% that of traditional concrete with the incorporation of low-carbon LC3 binder, CO_2 sequestration, and waste polyethylene fiber and waste foundry sand utilization. Additionally, the cost of this ECC is only 67% that of traditional concrete. The resulting low-carbon ECC has a compressive strength of at least 30 MPa and the tensile strength of 4 MPa with a 6% tensile ductility. Furthermore, the developed ECC exhibits improved autogenous crack width control with an average crack width of 69 mm.

The addition of sisal fiber in the low carbon ECC was found to serve multiple purposes. From a sustainability point of view, renewable sisal fiber was found to enhance carbon sequestration by 10% by serving as conduits allowing deeper diffusion transport of CO_2 into the precast element during carbonation curing. From a mechanical performance point of view, sisal fibers were found to enhance the tensile ductility of the ECC by serving as artificial flaws and triggering a larger number of microcracks in the composite during tensile strain-hardening.

The developed ECC offers compelling advantages of low carbon footprint, cost-effectiveness, and ductile performance, thus positioning it as a competitive alternative to conventional concrete in both economic, environmental and technical performance terms.

This research opens a feasible pathway of creating civil infrastructure that has low embodied carbon in the material production phase as well as low operational carbon in the infrastructure use phase. Future research is needed to quantify the cost and carbon footprint savings in the life cycle of civil infrastructure using such low carbon ECC materials.

3.6. References

[1] H. Ritchie, M. Roser, Plastic Pollution, Published Online at OurWorldInData.Org. (n.d.).

[2] The PEW Charitable Trusts and SystemIQ, Breaking the Plastic Wave: A Comprehensive Assessment of Pathways Towards Stopping Ocean Plastic Pollution, 2020. https://www.pewtrusts.org/en.

[3] S.B. Borrelle, J. Ringma, K.L. Law, C.C. Monnahan, L. Lebreton, A. Mcgivern, E. Murphy, J. Jambeck, G.H. Leonard, M.A. Hilleary, M. Eriksen, H.P. Possingham, H. de Frond, L.R. Gerber, B. Polidoro, A. Tahir, M. Bernard, N. Mallos, M. Barnes, C.M. Rochman, Predicted growth in plastic waste exceeds efforts to mitigate plastic pollution, Science (1979). 369 (2020) 1515–1518. https://doi.org/10.1126/science.aba3656 (accessed January 24, 2023).

[4] Global Ghost Gear Initiative, GGGI 2021 Annual Report, 2022.

[5] N.J. Beaumont, M. Aanesen, M.C. Austen, T. Börger, J.R. Clark, M. Cole, T. Hooper, P.K. Lindeque, C. Pascoe, K.J. Wyles, Global ecological, social and economic impacts of marine plastic, Mar Pollut Bull. 142 (2019) 189–195. https://doi.org/10.1016/j.marpolbul.2019.03.022.

[6] H. Ritchie, M. Roser, P. Rosado, CO_2 and Greenhouse Gas Emissions, OurWorldInData. (2020). https://ourworldindata.org/co2-and-greenhouse-gas-emissions (accessed March 10, 2023).

[7] N.M. Nguyen, T.H. Han, J.K. Park, J.J. Kim, Strength and Toughness of Waste Fishing Net Fiber-Reinforced Concrete, Materials. 14 (2021). https://doi.org/10.3390/ma14237381 (accessed January 24, 2023).

[8] V.C. Li, Engineered Cementitious Composites – Bendable Concrete for Sustainable and Resilient Infrastructure, Springer, Germany, 2019. https://doi.org/10.1007/978-3-662-58438-5.

[9] M.D. Lepech, V.C. Li, Water permeability of engineered cementitious composites, Cem Concr Compos. 31 (2009) 744–753. https://doi.org/10.1016/j.cemconcomp.2009.07.002.

[10] M. Sahmaran, M. Li, V.C. Li, Transport Properties of Engineered Cementitious Composites Under Chloride Exposure, ACI Mater J. 104 (2007) 604–611.

[11] M.D. Lepech, V.C. Li, R.E. Robertson, G.A. Keoleian, Design of green engineered cementitious composites for improved sustainability, ACI Mater J. 105 (2008) 567–575. https://doi.org/10.14359/20198.

[12] D. Shoji, Z. He, D. Zhang, V.C. Li, The greening of engineered cementitious composites (ECC): A review, Constr Build Mater. 327 (2022). https://doi.org/10.1016/j.conbuildmat.2022.126701.

[13] A.A. Bahraq, M. Maslehuddin, S.U. Al-Dulaijan, Macro- and Micro-Properties of Engineered Cementitious Composites (ECCs) Incorporating Industrial Waste Materials: A Review, Arab J Sci Eng. 45 (2020) 7869–7895. https://doi.org/10.1007/s13369-020-04729-7.

[14] H. Zhu, D. Zhang, T. Wang, H. Wu, V.C. Li, Mechanical and self-healing behavior of low carbon engineered cementitious composites reinforced with PP-fibers, Constr Build Mater. 259 (2020) 119805. https://doi.org/10.1016/j.conbuildmat.2020.119805.

[15] J. Yu, H.L. Wu, C.K.Y. Leung, Feasibility of using ultrahigh-volume limestone-calcined clay blend to develop sustainable medium-strength Engineered Cementitious Composites (ECC), J Clean Prod. 262 (2020). https://doi.org/10.1016/j.jclepro.2020.121343.

[16] D. Zhang, B. Jaworska, H. Zhu, K. Dahlquist, V.C. Li, Engineered Cementitious Composites (ECC) with limestone calcined clay cement (LC3), Cem Concr Compos. 114 (2020). https://doi.org/10.1016/j.cemconcomp.2020.103766.

[17] S. Sánchez Berriel, A. Favier, E. Rosa Domínguez, I.R. Sánchez MacHado, U. Heierli, K. Scrivener, F. Martirena Hernández, G. Habert, Assessing the environmental and economic potential of Limestone Calcined Clay Cement in Cuba, J Clean Prod. 124 (2016) 361–369. https://doi.org/10.1016/j.jclepro.2016.02.125.

[18] Y.C. Díaz, S.S. Berriel, U. Heierli, A.R. Favier, I.R.S. Sánchez Machado, K.L. Scrivener, J.F. Martirena Hernández, G. Habert, Limestone calcined clay cement as a low-carbon solution to meet expanding cement demand in emerging economies, Dev Eng. 2 (2017) 82–91. https://doi.org/10.1016/j.deveng.2017.06.001.

[19] V.C. Li, C. Wu, S. Wang, A. Ogawa, T. Saito, Interface tailoring for strain-hardening polyvinyl alcohol-engineered cementitious composite (PVA-ECC), ACI Mater J. 99 (2002) 463–472. https://www.researchgate.net/publication/279938212.

[20] K.Q. Yu, J.T. Yu, J.G. Dai, Z.D. Lu, S.P. Shah, Development of ultra-high performance engineered cementitious composites using polyethylene (PE) fibers, Constr Build Mater. (2018). https://doi.org/10.1016/j.conbuildmat.2017.10.040.

[21] K.Q. Yu, W.J. Zhu, Y. Ding, Z.D. Lu, J. tao Yu, J.Z. Xiao, Micro-structural and mechanical properties of ultra-high performance engineered cementitious composites (UHP-ECC) incorporation of recycled fine powder (RFP), Cem Concr Res. 124 (2019) 105813. https://doi.org/10.1016/j.cemconres.2019.105813.

[22] D. Zhang, J. Yu, H. Wu, B. Jaworska, B.R. Ellis, V.C. Li, Discontinuous micro-fibers as intrinsic reinforcement for ductile Engineered Cementitious Composites (ECC), Compos B Eng. (2020). https://doi.org/10.1016/j.compositesb.2020.107741.

[23] G. (Graeme) Macfadyen, T. Huntington, Rod. Cappell, Food and Agriculture Organization of the United Nations., United Nations Environment Programme., Abandoned, lost or otherwise discarded fishing gear, United Nations Environment Programme, 2009.

[24] I. Maria, G. Bertelsen, L.M. Ottosen, Engineering properties of fibres from waste fishing nets Materials, Systems and Structures in Civil Engineering Circular Ocean, 2016.

[25] V.C. Li, S. Wang, C. Wu, Tensile strain-hardening behavior or polyvinyl alcohol engineered cementitious composite (PVA-ECC), ACI Mater J. 98 (2001) 483–492. https://doi.org/10.14359/10851.

[26] D. Zhang, B.R. Ellis, B. Jaworska, W.H. Hu, V.C. Li, Carbonation curing for precast Engineered Cementitious Composites, Constr Build Mater. 313 (2021). https://doi.org/10.1016/j.conbuildmat.2021.125502.

[27] P. Suthiwarapirak, T. Matsumoto, T. Kanda, Multiple cracking and fiber bridging characteristics of engineered cementitious composites under fatigue flexure, Journal of Materials in Civil Engineering. 16 (2004) 433–443. https://doi.org/10.1061/(ASCE)0899-1561(2004)16:5(497).

[28] V. Rostami, Y. Shao, A.J. Boyd, Z. He, Microstructure of cement paste subject to early carbonation curing, Cem Concr Res. 42 (2012) 186–193. https://doi.org/10.1016/j.cemconres.2011.09.010.

[29] D. Zhang, T. Liu, Y. Shao, Weathering Carbonation Behavior of Concrete Subject to Early-Age Carbonation Curing, Journal of Materials in Civil Engineering. 32 (2020) 04020038. https://doi.org/10.1061/(asce)mt.1943-5533.0003087.

[30] M.D. Lepech, V.C. Li, Cement & Concrete Composites Water permeability of engineered cementitious composites, Cem Concr Compos. 31 (2009) 744–753. https://doi.org/10.1016/j.cemconcomp.2009.07.002.

[31] V.C. Li, E.N. Herbert, Self-healing of microcracks in engineered cementitious composites (ECC) under a natural environment, Materials. 6 (2013) 2831–2845. https://doi.org/10.3390/ma6072831.

[32] M.M. Camargo, E. Adefrs Taye, J.A. Roether, D.T. Redda, A.R. Boccaccini, A Review on Natural Fiber-Reinforced Geopolymer and Cement-Based Composites, Materials. (2020). https://doi.org/10.3390/ma13204603.

[33] M. Muthangya, A.M. Mshandete, A.K. Kivaisi, Two-stage fungal pre-treatment for improved biogas production from sisal leaf decortication residues, Int J Mol Sci. 10 (2009) 4805–4815. https://doi.org/10.3390/ijms10114805.

[34] M. Saxena, A. Pappu, R. Haque, A. Sharma, Sisal Fiber Based Polymer Composites and Their Applications, Cellulose Fibers: Bio- and Nano-Polymer Composites. (2011).

[35] M.L.M. Broeren, S.N.C. Dellaert, B. Cok, M.K. Patel, E. Worrell, L. Shen, Life cycle assessment of sisal fibre – Exploring how local practices can influence environmental performance, J Clean Prod. 149 (2017) 818–827. https://doi.org/10.1016/j.jclepro.2017.02.073.

[36] J. Wei, C. Meyer, Improving degradation resistance of sisal fiber in concrete through fiber surface treatment, Appl Surf Sci. 289 (2014) 511–523. https://doi.org/10.1016/j.apsusc.2013.11.024.

[37] J. Wei, Degradation behavior and kinetics of sisal fiber in pore solutions of sustainable cementitious composite containing metakaolin, Polym Degrad Stab. 150 (2018) 1–12. https://doi.org/10.1016/j.polymdegradstab.2018.01.027.

[38] D. Zhang, Y. Shao, Early age carbonation curing for precast reinforced concretes, Constr Build Mater. 113 (2016) 134–143. https://doi.org/10.1016/j.conbuildmat.2016.03.048.

[39] ASTM, Standard Test Method for Sieve Analysis of Fine and Coarse Aggregates 1, ASTM. (2022). https://doi.org/10.1520/C0136_C0136M-19.

[40] G. Ganesh Prabhu, J.W. Bang, B.J. Lee, J.H. Hyun, Y.Y. Kim, Mechanical and Durability Properties of Concrete Made with Used Foundry Sand as Fine Aggregate, Advances in Materials Science and Engineering. 2015 (2015). https://doi.org/10.1155/2015/161753.

[41] J.M. Khatib, S. Baig, A. Bougara, C. Booth, Foundry sand utilisation in concrete production, 2nd International Conference on Sustainable Construction Materials and Technologies. (2010) 931–935.

[42] T.R. Naik, F. Asce, R.N. Kraus, B.W. Ramme, M. Asce, F. Canpolat, Effects of Fly Ash and Foundry Sand on Performance of Architectural Precast Concrete, (2012). https://doi.org/10.1061/(ASCE).

[43] ASTM, Standard Test Method for Tensile Properties of Single Textile Fibers, ASTM. (2020). https://doi.org/10.1520/D3822_D3822M-14R20.

[44] ASTM, Standard Test Method for Density of High-Modulus Fibers, American Society for Testing and Materials. (2022). https://doi.org/10.1520/D3800-22.

[45] D. Zhang, X. Cai, Y. Shao, Carbonation Curing of Precast Fly Ash Concrete, Journal of Materials in Civil Engineering. 28 (2016) 04016127. https://doi.org/10.1061/(asce)mt.1943-5533.0001649.

[46] J.M. Valverde, A. Perejon, S. Medina, L.A. Perez-Maqueda, Thermal decomposition of dolomite under CO2: Insights from TGA and in situ XRD analysis, Physical Chemistry Chemical Physics. 17 (2015) 30162–30176. https://doi.org/10.1039/c5cp05596b.

[47] K.S.P. Karunadasa, C.H. Manoratne, H.M.T.G.A. Pitawala, R.M.G. Rajapakse, Thermal decomposition of calcium carbonate (calcite polymorph) as examined by in-situ high-temperature X-ray powder diffraction, Journal of Physics and Chemistry of Solids. 134 (2019) 21–28. https://doi.org/10.1016/j.jpcs.2019.05.023.

[48] D. Mentes, C.E. Tóth, G. Nagy, G. Muránszky, C. Póliska, Investigation of gaseous and solid pollutants emitted from waste tire combustion at different temperatures, Waste Management. 149 (2022) 302–312. https://doi.org/10.1016/j.wasman.2022.06.027.

[49] H. Yokota, K. Rokugo, N. Sakata, Recommendations for Design and Construction of High Performance Fiber Reinforced Cement Composite with Multiple Fine Cracks, Japan Society of Civil Engineers. (2008).

[50] ASTM, Standard Test Method for Compressive Strength of Hydraulic Cement Mortars (Using 2-in. or [50-mm] Cube Specimens) 1, ASTM. (2020). https://doi.org/10.1520/C0109_C0109M-20.

[51] ASTM, Standard Test Method for Linear-Elastic Plane-Strain Fracture Toughness of Metallic Materials 1, ASTM. (2022). https://doi.org/10.1520/E0399-22.

[52] C. Redon, V.C. Li, C. Wu, H. Hoshiro, T. Saito, A. Ogawa, Measuring and Modifying Interface Properties of PVA Fibers in ECC Matrix, Journal of Materials in Civil Engineering. 13 (2001) 399–406. https://doi.org/10.1061/(asce)0899-1561(2001)13:6(399).

[53] A. Katz, V.C. Li, A special technique for determining the bond strength of micro-fibres in cement matrix by pullout test, 1996.

[54] T. Kanda, V.C. Li, Interface Property and Apparent Strength of High-Strength Hydrophilic Fiber in Cement Matrix, Journal of Materials in Civil Engineering. 10 (1998) 5–13. https://doi.org/10.1061/(asce)0899-1561(1998)10:1(5).

[55] E.-H. Yang, S. Wang, Y. Yang, V.C. Li, Fiber-Bridging Constitutive Law of Engineered Cementitious Composites, J. Adv. Concr. Technol. 6 (2008) 181–193.

[56] I. Monteiro, F.A. Branco, J. De Brito, R. Neves, Statistical analysis of the carbonation coefficient in open air concrete structures, Constr Build Mater. 29 (2012) 263–269. https://doi.org/10.1016/j.conbuildmat.2011.10.028.

[57] E. Possan, W.A. Thomaz, G.A. Aleandri, E.F. Felix, A.C.P. dos Santos, CO2 uptake potential due to concrete carbonation: A case study, Case Studies in Construction Materials. 6 (2017) 147–161. https://doi.org/10.1016/j.cscm.2017.01.007.

[58] B. Šavija, M. Luković, Carbonation of cement paste: Understanding, challenges, and opportunities, Constr Build Mater. 117 (2016) 285–301. https://doi.org/10.1016/j.conbuildmat.2016.04.138.

[59] B.Lecampion, J.Vanzo, F.J.Ulm, B.Hue, C.Germa, I.Khalfallah, J.Dirrenberge, Evolution of Portland cement mechanical properties exposed to CO2 rich fluids: investigation at different scales, Mechanics and Physics of Porous Solids (MPPS) - A Tribute to Prof. Olivier Cousssy. (2011). https://www.researchgate.net/publication/258110799.

[60] O. Çopuroğlu, E. Schlangen, Modeling of frost salt scaling, Cem Concr Res. 38 (2008) 27–39. https://doi.org/10.1016/j.cemconres.2007.09.003.

[61] P. Suthiwarapirak, T. Matsumoto, Fiber Bridging Degradation Based Fatigue Analysis of ECC under Flexure, J Appl Mech. 6 (2003) 1179–1188. https://doi.org/10.2208/journalam.6.1179.

[62] J. Zhang, H. Stang, V.C. Li, Crack bridging model for fibre reinforced concrete under fatigue tension, Int J Fatigue. 23 (2001) 655–670. https://doi.org/10.1016/S0142-1123(01)00041-X.

[63] M. Antoni, J. Rossen, F. Martirena, K. Scrivener, Cement substitution by a combination of metakaolin and limestone, Cem Concr Res. 42 (2012) 1579–1589. https://doi.org/10.1016/j.cemconres.2012.09.006.

[64] B. Bhardwaj, P. Kumar, Waste foundry sand in concrete: A review, Constr Build Mater. 156 (2017) 661–674. https://doi.org/10.1016/j.conbuildmat.2017.09.010.

[65] H.W. Chung, T. Subgranon, M. Tia, H. Deford, J. Armenteros, The effects of reduced paste volume in Portland limestone cement concrete, Magazine of Concrete Research. 73 (2021) 958–972. https://doi.org/10.1680/jmacr.19.00541.

[66] U.S. Department of Transportation Federal Highway Administration, Table HM-12 Highway statistics 2020, (2020).

[67] National Asphalt Pavement Association, The Asphalt Pavement Industry Fast Facts, 2020. https://doi.org/10.13140/RG.2.2.21946.82888.

[68] M.L. Marceau, M.A. Nisbet, M.G. Vangeem, Life Cycle Inventory of Portland Cement Concrete, 2006.

[69] F. Pacheco-Torgal, Z. Abdollahnejad, S. Miraldo, M. Kheradmand, Alkali-Activated Cement-Based Binders (AACBs) as Durable and Cost-Competitive Low-CO2 Binder Materials: Some Shortcomings That Need to be Addressed, in: Handbook of Low Carbon Concrete, Elsevier Inc., 2017: pp. 195–216. https://doi.org/10.1016/B978-0-12-804524-4.00009-9.

[70] J.S. Damtoft, J. Lukasik, D. Herfort, D. Sorrentino, E.M. Gartner, Sustainable development and climate change initiatives, Cem Concr Res. 38 (2008) 115–127. https://doi.org/10.1016/j.cemconres.2007.09.008.

[71] H.L. Wu, D. Zhang, B.R. Ellis, V.C. Li, Development of reactive MgO-based Engineered Cementitious Composite (ECC) through accelerated carbonation curing, Constr Build Mater. 191 (2018) 23–31. https://doi.org/10.1016/j.conbuildmat.2018.09.196.

[72] C. Fu, M. Chen, R. Guo, R. Qi, Green-Engineered Cementitious Composite Production with High-Strength Synthetic Fiber and Aggregate Replacement, Materials. 15 (2022). https://doi.org/10.3390/ma15093047.

Chapter 4. Use of Localized Materials

By combining the carbonation curing and the use of IWMs methods proposed in Chapter 2 and Chapter 3, a sustainable low-carbon ECC with 50% reduction in embodied carbon footprint and 33% decrease in costs reduction compared to conventional concrete can be developed. However, the costs of IWMs, especially for FA, and the manufactured silica sands that commonly used in ECC are expected to rise due to the inflation. To address this challenge, this chapter introduces the use of localized materials, such as volcanic ash (VA) and desert sand (DS), as substitutes for FA and silica sand., offering a feasible pathway towards decarbonizing ECC using locally available materials.

4.1. Introduction

Concrete is widely used in modern urban and highway pavement construction due to its capacity to carry heavy loads [1] with lower life cycle cost, enhanced durability, and sustainability compared to asphalt pavement [2]. In 2020, over 0.15 million miles of road in the United States was surfaced with concrete [3], consuming more than 22 million tons of concrete [4]. However, traffic volumes have significantly increased over the past 20 years, leading to an earlier need to reconstruct and rehabilitate concrete pavements [5].

Engineered cementitious composites (ECC) is a strain-hardening fiber-reinforced concrete with high tensile ductility [6]. The intrinsic ability of ECC to tightly control microcrack width and exhibit self-healing capabilities [7,8] results in reduced water permeability [9] and improved fatigue performance [10–12] than those of conventional concrete. Therefore, ECC has been successfully applied in transportation infrastructure, including bridge decks and pavements, to enhance durability and resilience [13,14]. It has been proven that the thickness of ECC pavements can be reduced by more than 50% [15] while maintaining comparable service life to conventional concrete pavements [14]. However, ECC suffers from a high embodied carbon footprint due to high cement usage [16]. Therefore, industrial waste materials (IWMs), also known as industrial

waste streams, have recently been used to reduce the carbon footprint by substituting raw materials in ECC mixtures [17].

Fly ash (FA) is one of the most utilized IWMs in ECC since it can enhance matrix workability and self-consolidating processing due to the spherical shape of fly ash particles. It can also reduce the heat of hydration and drying shrinkage of ECC [18]. However, the price of FA is expected to keep increasing due to the declining supply caused by the diminished coal combustion plants operation in the future [19,20]. Furthermore, in certain regions, particularly in the Middle East, the primary power generation sources are oil and natural gas, with coal contributing only 5% to the power supply in 2016 [21,22]. Importation of FA, while feasible, incurs a high cost and carbon footprint associated with long-distance transportation. Thus, finding a suitable alternative IWMs to substitute FA in ECC is imperative.

Recent research used the Middle East's volcanic ash (VA) to develop low-cost, low-carbon concrete [23,24]. VA-ECC has also been investigated and shown comparable tensile performance with promising tensile ductility (7.4%) and tiny crack width (50 μm at failure) to FA-ECC [25]. Nonetheless, the compressive strength of ECC was reduced up to 40% by substituting FA with VA due to the larger particle size and higher porosity of VA [25]. Despite the presence of a substantial body of literature on the shrinkage behavior of conventional ECC, which has been shown to experience significant shrinkage (reaching up to 1200 με-1800 με at 28 days) due to its high cementitious contents [26–28], the shrinkage characteristics of VA-ECC have not been studied. It is hypothesized that VA-ECC may exhibit more shrinkage than FA-ECC, as previous studies have indicated increased shrinkage in VA concrete [29]. When restrained, the increased shrinkage will cause high tensile stress and may lead to cracking in VA-ECC, thereby limiting its applications with large surface area, such as in pavements.

Methods for mitigating the shrinkage of concrete and ECC has been proposed in previous studies. One practical approach is adding shrinkage-compensating admixture [30], including calcium sulfate and calcium aluminate, which can react with water to form ettringite [31,32]. By incorporating calcium sulphoaluminate cement (CSA), intrinsic self-stressing FA-ECC has been developed, resulting in tiny crack width and high ductility (5.5%) [33]. To achieve self-stressing ECC, increased early-age expansion and lowered long-term expansion loss are required (expansion

loss < 50%) [33]. This provides a potential solution for investigating self-stressing VA-ECC. However, VA-ECC suffers from larger shrinkage compared to FA-ECC. To achieve adequate early-age and long-term expansion for self-stressing VA-ECC, a higher content of CSA is required. This contradicts the idea that only a low content of CSA can be used for VA-ECC, considering the high temperatures prevalent in the Middle East and the rapid setting time of high-dosage CSA cement [34,35]. These factors impose limitations on the working time available for ECC between the mixing and placement operations. The combination of high-temperature environments, limitations on CSA content, and low water-to-binder ratio to achieve a desired strength all hinder the early-age expansion of VA-ECC. Consequently, further research is required in order to mitigate the pronounced shrinkage and develop a self-stressing VA-ECC.

Besides FA, the cost and embodied carbon associated with the manufactured F75 silica sands, commonly employed in ECC, are higher than locally available desert sand (DS) in the Middle East [36]. Considering the cost-effectiveness and abundant availability of DS, DS-ECC, which demonstrates promising strain-hardening behavior, has been investigated [37–39]. Although DS-ECC experiences a decrease in strength and Young's modulus [39], the use of DS results in a lower material cost [36]. Consequently, DS proves to be a favorable fine aggregate choice for VA-ECC. Both VA and DS are locally accessible materials that offer the benefits of low-cost and low-carbon emissions.

This research aims to develop a durable self-stressing ECC utilizing VA, DS, and a low content of CSA, which allows a sufficient construction time window in the summer season. A comprehensive experimental program was conducted to evaluate the tensile performance, compressive strength, flexural strength, crack patterns, shrinkage, cost and embodied carbon footprint of DS-VA-ECC, with water-to-binder ratio (W/B ratio), CSA dosages, and curing conditions, as controlled variables. Specifically, DS-VA-ECC with four different W/B ratios were fabricated to identify the most suitable mix based on mechanical performance and workability. Subsequently, adjustments were made to CSA dosages and curing conditions to achieve optimal working time windows and self-stressing characteristics. X-ray Diffraction (XRD) analysis and optical microscopy were conducted to investigate the microstructural mechanisms behind the observed physical and mechanical properties.

4.2. Experimental programs

4.2.1 Materials and mix proportions

Seven mixtures were designed for DS-VA-ECC, as shown in Table 4-1. Four W/B ratios of 0.18 (W18), 0.20 (W20), 0.22 (W22), and 0.24 (W24) were used to examine the mechanical properties and workability of ECC, with the CSA content fixed at 100 kg/m^3. For the W/B ratio of 0.2, two additional CSA dosages of 70 (W20-C70) and 130 (W20-C130) were investigated. A control mixture W20-F100 using FA instead of VA, served as a benchmark to evaluate the shrinkage effect of FA and VA in this study. All 0.2 W/B ratio mixtures were cured under 5 conditions (see Table 4-2). To obtain the strain-hardening effect and to reduce the material costs and embodied carbon simultaneously, a hybrid 1% PE and 1% PP fibers was adopted for all mixtures. Fiber properties can be found in Table 4-3.

Table 4-1. Mixture design of ECC (kg/m^3).

Mixture	PLC*	CSA	VA	FA	DS	Water	WR	PE**	PP**
W18-C100	500	100	500	0	660	198	40	10	10
W20-C100	500	100	500	0	660	220	32	10	10
W22-C100	500	100	500	0	660	242	23	10	10
W24-C100	500	100	500	0	660	264	14	10	10
W20-C70	530	70	500	0	660	220	30	10	10
W20-C130	470	130	500	0	660	220	34	10	10
W20-F100	500	100	0	500	660	220	7	10	10

*Portland limestone cement (PLC).

**Volume fraction for both PE and PP fibers is 1%.

Table 4-2. Curing conditions of ECC.

Name	Curing method
T20-Air	Samples were cured in the air (20±3 ℃, 40±5% RH).
T20-Wet24	A wet cloth covered samples for 24 h, then cured in the air (20±3 ℃, 40±5% RH).
T20-Wet 72	A wet cloth covered samples for 72 h, then cured in the air (20±3 ℃, 40±5% RH).
T40-Air	Samples were cured in 40 ℃ oven.
T40- Wet72	Samples were cured in 40 ℃ oven, and a wet cloth was covered for the first 72 h.

Table 4-3. Technical parameters of PP and PE fibers.

Fiber type	Diameter (μm)	Length (mm)	Nominal strength (GPa)	Young's modulus (MPa)	Rupture elongation (%)	Density (g/cm^3)
PE	24	12	2.90	116	2.42	0.97
PP	18	12	0.40	-	40	0.91

The binder system included Portland limestone cement (PLC) from Lafarge Holcim Cement Co., CSA from CTS company, VA sourced from Gulf Business Horizon (commercially known as SNP crete), and DS from Saudi Readymix. The chemical compositions and particle size distributions of these binder constituents are shown in Table 4-4 and Figure 4-1, respectively. Figure 4-2 illustrates the morphology of FA and VA obtained from a scanning electron microscope (SEM). While the particle size of VA is comparable to the reference FA, its angular particles contrast with the spherical shape of FA. The angular morphology of VA results in inferior paste rheology in the fresh state of ECC.

Table 4-4. Chemical compositions of PLC and VA (%).

Constituents	SiO_2	Al_2O_3	Fe_2O_3	CaO	MgO	Na_2O	K_2O
PLC	18.8	4.6	2.8	68.3	2.1	0	06
CSA	7.0	10.1	0.7	47.2	1.1	0	0.1
VA	48.35	14.43	12.34	12.43	6.54	1.26	0.77
FA	51.6	16.2	5.0	10.8	3.7	4.8	2.5

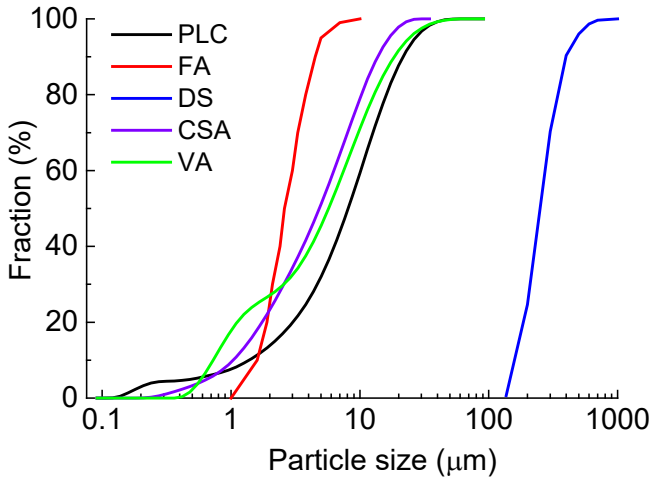

Figure 4-1. Particle size distributions of dry constituents.

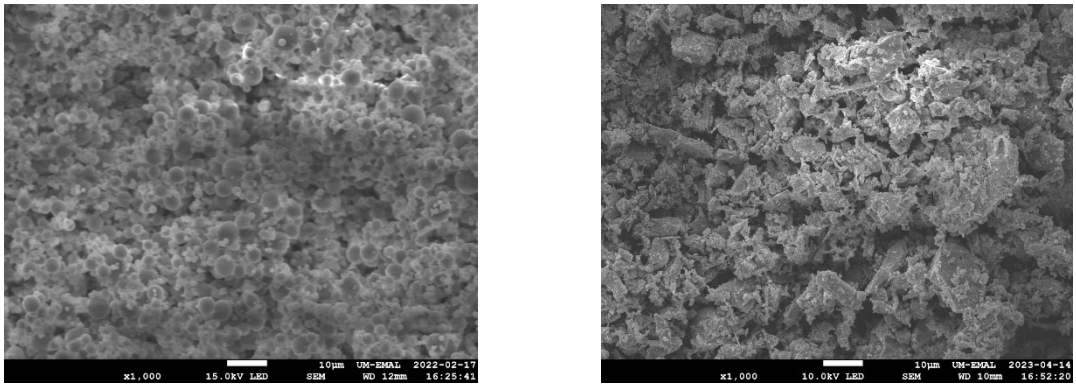

(a) FA (b) VA

Figure 4-2. SEM pictures of (a) FA and (b) VA.

4.2.2 Sample preparation

The dry ingredients comprising PLC, CSA, VA, and DS were pre-mixed for 5 minutes with a Hobart HL300 planetary mixer operated at the first speed (94 rpm). Water and water reducer were added and mixed for 5 minutes to attain a uniform paste. Once the fresh mixture was prepared, 1% PE and 1% PP fibers were added and mixed at the second speed (174 rpm).

Following 28-day curing under air condition (T20-Air, 20±3 ℃, 40±5% RH), compressive strength, uniaxial tension, and bending tests were carried out on cubes measuring 50 by 50 by 50 mm^3, dogbone-shaped specimens (see Figure 4-3), and beam samples measuring 300 by 75 by 13 mm^3, respectively.

4.2.3 Mechanical properties tests

This study used a 100 KN capacity Material Testing Systems (MTS) loading frame for uniaxial tension tests and 4-point bending tests. The tests were performed on specimens after 28 days of curing. The uniaxial tension tests were conducted under displacement control at a 0.5 mm/min rate per JSCE [40]. The dimensions of dogbone-shaped specimens used for the uniaxial tension test are shown in Figure 4-3(a). Two linear variable displacement transducers (LVDT) were positioned with an 80mm gauge length, as illustrated in Figure 4-3(b). The 4-point bending tests were conducted according to ASTM D6272 [41] to measure the ultimate tensile strength and tensile strain of beam specimens. Detailed experimental configuration for the 4-point bending tests can be found in Figure 4-4. Additionally, 50 by 50 by 50 mm^3 cubes were fabricated and subjected to loading at a rate of 0.5MPa/s using the Forney machine following ASTM C109 [42].

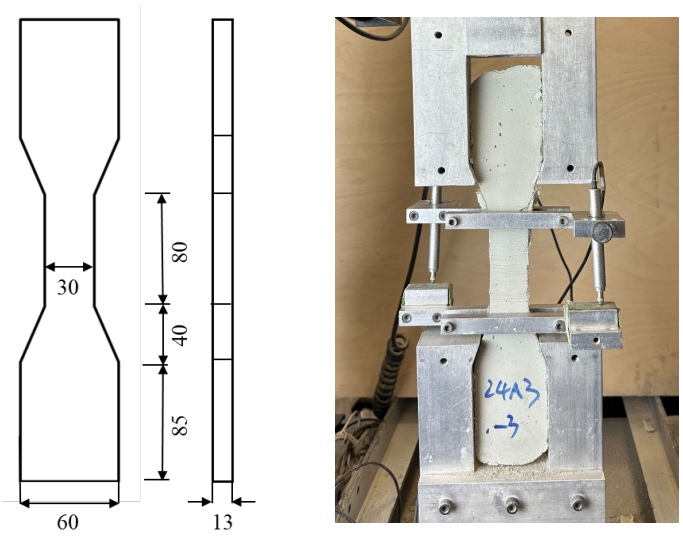

(a) (b)

Figure 4-3. Dogbone-shaped specimen for uniaxial tension (a) showing dimensions (Unit: mm) and (b) the grip and LVDT setup.

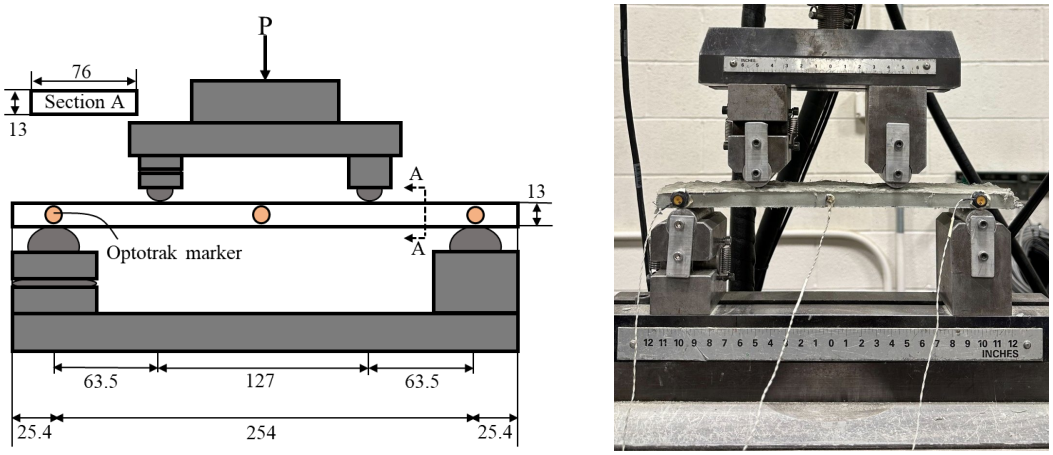

Figure 4-4. Experiment configuration for 4-point flexural bending (Unit: mm).

4.2.4 Shrinkage monitoring

For the free shrinkage/expansion tests, square prism specimens measuring 25 by 25 by 300 mm^3 were utilized with the test setup in accordance with ASTM C490 [43] (refer to Figure 4-5). The length of the specimens was measured 3 hours after demolding and continued until 90 days. Five distinct curing conditions were implemented, as depicted in Table 4-2. T20-Air and T40-Air

denoted curing in the air at 20 ℃ and 40 ℃, respectively. Similarly, T20-Wet72 and T40-Wet72 indicated that the samples were covered with a wet cloth for 72 hours and subsequently cured in 20 ℃ and 40 ℃ air, respectively. T20-Wet24 represented the samples only covered with a damp cloth for 24 hours in 20 ℃ air.

Shrinkage/expansion characteristics for W20-C70, W20-C100, and W20-C130 with different curing conditions were analyzed, including the maximum expansion, expansion at 28/90 days, and expansion loss. The mix proportion of W20-F100 was also measured as a reference benchmark for comparing shrinkage/expansion between VA and FA ECC.

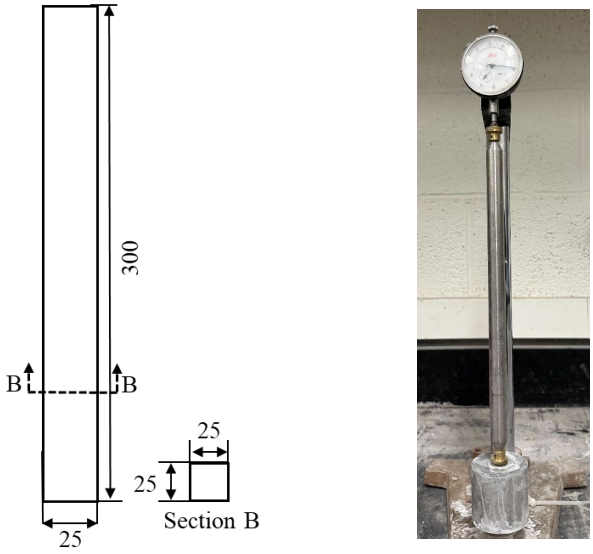

(a) (b)

Figure 4-5. Square prism specimen for free shrinkage/expansion test (a) showing dimensions (Unit: mm) and (b) the test setup.

4.2.5 Micro/mechanism investigation

Due to difference in water demand, it is anticipated that VA-ECC will exhibit substantially higher shrinkage in comparison to FA-ECC. Therefore, the chemical compositions of W20-F100 and W20-C100 T20-Air/Wet24 ECC were evaluated using the XRD method. The paste samples were ground into powders with particle sizes under 100 μm and sealed before measurement. The fibers were separated through sieving before conducting the tests. This study used a Rigaku Ultima

4 diffractometer with Cu K-alpha radiation for the XRD analysis (scan step 0.05 degree/step and 1 degree/min).

4.2.6 Working time window/feasibility evaluation

The working time window and flowability of DS-VA-ECC were determined by flow table tests following ASTM C1437 [44]. ECC mortars were filled into the truncated cone, which had a bottom diameter of 100 mm and 60 mm in height. The truncated cone was lifted away from the mortar after 1 minute, and the table was immediately dropped 25 times in 15 seconds [44]. Afterward, the spread diameter of the ECC mortar was measured along the four scribed on the tabletop with a caliper. The spread diameter was recorded every 30 minutes after the mixing water was added to the mixtures until the surface of ECC hardened and the spread diameter dropped below 130 mm, which is regarded as suitable fluidity to secure workability at a construction site [45].

4.3. Results and discussions

4.3.1 Shrinkage behavior

4.3.1.1 Effect of substituting FA with VA

Figure 4-6. plots the 90 days free length change of air-cured fly ash ECC (W20-F100) and VA-ECC (W20-C70, C100, and C130 ECC). The shrinkage for the benchmark W20-F100 mixture at 28 days is -728 με, which is smaller than conventional ECC, i.e., -1200 με to -1800 με [26–28,46], due to the usage of CSA. The shrinkage of W20-F100 in this study was consistent with those of CSA ECC in the literature [25,47,48], showing around -600 με to -900 με shrinkage with similar CSA dosage. The decreased shrinkage is caused by the expansion mechanism of CSA cement forming the ettringite [32,49], which is governed by Equation (4-1) - (4-3) [50–52]:

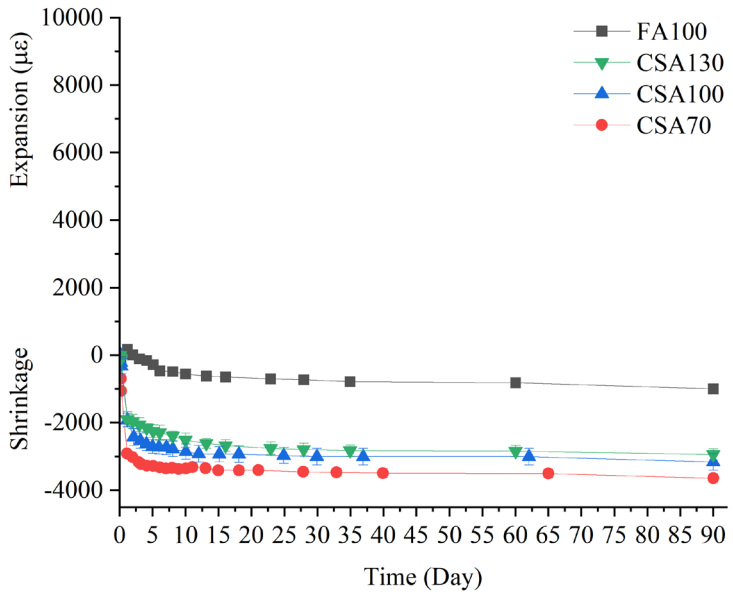

Figure 4-6. Shrinkage deformation of air-cured (T20-Air) W20-F100, C70, C100, and C130 ECC.

$$2C_3S + 11H \rightarrow C_3S_2H_8 + 3CH$$
$$2C_2S + 9H \rightarrow C_3S_2H_8 + CH \quad (4\text{-}1)$$

$$C_4A_3\bar{S} + 2C\bar{S} + 37H \rightarrow C_3A \cdot 3C\bar{S} \cdot H_{32} + 2AH_3$$
$$C\bar{S} + 2H \rightarrow 2C\bar{S}H_2$$
$$C_4A_3\bar{S} + 2C\bar{S}H_2 + 34H \rightarrow C_3A \cdot 3C\bar{S} \cdot H_{32} + 2AH_3 \quad (4\text{-}2)$$

$$C_4A_3\bar{S} + 8C\bar{S}H_2 + 74H + 6CH \rightarrow 3C_3A \cdot 3C\bar{S} \cdot H_{32} \quad (4\text{-}3)$$

where C_3S and C_2S represents the tricalcium and dicalcium silicate from cement, respectively. The hydration reactions of both calcium silicates in Equation (4-1) will form the Calcium hydroxide (CH) and Calcium silicate hydrate ($C_3S_2H_8$). $C_4A_3\bar{S}$, $C\bar{S}$, $C\bar{S}H_2$, are ye'elimite, anhydrite, and gypsum from CSA cement, which can react with water and CH (from Equation (4-1) and VA/FA) to form aluminum hydroxide (AH_3) and ettringite ($C_3A \cdot 3C\bar{S} \cdot H_{32}$) in Equation (4-2) and Equation (4-3).

Upon the substitution of FA with VA, specifically T20-Air W20-C70, C100, and C130 in this study, the 28 days shrinkage increased drastically to -3459 με, -3006 με, and -2794 με, correspondingly. This increase can be attributed to the higher water demand caused by the inherently angular form of VA particles, incorporating the water loss during the hydration process of VA-ECC compared to FA-ECC. The CaO and MgO contents within VA (12.43% and 6.54%) are higher relative to FA (10.8% and 3.7%), as shown in Table 4. The CaO and MgO in VA/FA consume water during hydration, competing with CSA cement, and could potentially impede ettringite formation.

The higher water demand associated with VA leads to larger autogenous shrinkage, as the water is maintained within the capillaries, eliciting high capillary forces when this water is used for hydration [53,54]. Therefore, alternative curing such as wet-curing rather than air-curing may be a plausible solution to provide sufficient water for VA instead of depending on a higher amount of mix water. Further detailed XRD analysis of the microstructural mechanism is discussed in Section 4.3.5.

4.3.1.2 Effect of curing conditions

The free length change for W20-C70, C100, and C130 with various curing conditions is depicted in Figure 4-7 to Figure 4-9. In the aspect of temperature, under air-cured conditions, 40℃ samples demonstrate higher shrinkage than 20℃ samples. The shrinkage at 28 days increased from -3459 με to -4140 με for W20-C70. The shrinkage also increased from -3006 με to -3319 με for W20-C100. A similar shrinkage increment effect was observed for W20-C130 that the shrinkage increased from -2794 με to -3374 με. Higher curing temperature accelerated the evaporation of free capillary water, resulting in considerable drying shrinkage. The evaporation of water also aggravated the lack of water for ettringite formation mentioned previously. T20-Wet24, T20-Wet72, and T40-Wet72 show the possible solution by providing adequate water to VA-ECC during curing. For both 20℃ and 40℃, VA-ECC demonstrates expansion rather than shrinkage.

Take T20-Wet24 (24 hours wet-curing, followed by 20℃ air-cured) for the W20-C70 mix as an example, a maximum expansion of 2261 με can be obtained and maintaining a 390 με expansion at 90 days. When raising the temperature to 40℃ (T40-Wet72), a maximum expansion

of 3141 με is reached for W20-C70 and retained a 1371 με expansion at 90 days. It is reasonable that T40-Wet72 provides more expansion than T20-Wet24 at first 24 hours since the rate of reaction for hydration grows with increasing temperatures [55–57]. With sufficient water supply, more ettringite is formed in a short period of time for higher temperature (40°C).

If the wet-curing time is also extended to 72 hours for 20°C W20-C70 so that there are longer hydration and ettringite formation time for the specimens, comparable maximum expansion and expansion at 90 days can be accomplished by T20-W72 (2989 με and 1221 με) compared to T40-W72 (3141 με and 1371 με), respectively. However, T20-Wet72 requires more time (3.17 days) to gain the maximum expansion than T40-Wet72 (1.14 days), which also relates to the hydration rate for different temperatures.

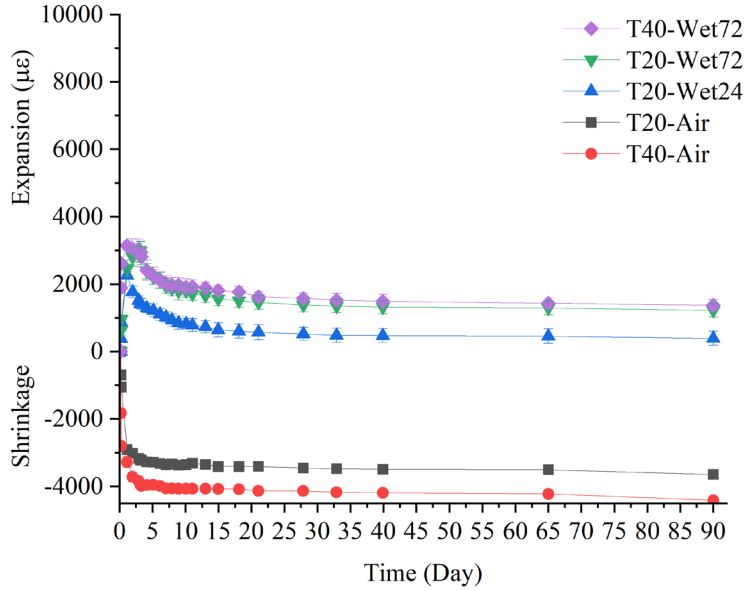

Figure 4-7. Shrinkage deformation of W20-C70 ECC under different curing conditions.

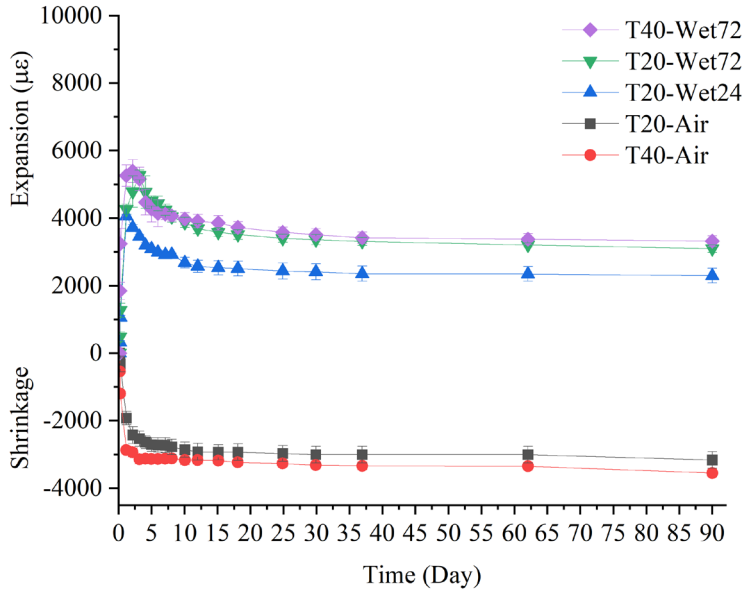

Figure 4-8. Shrinkage deformation of W20-C100 ECC under different curing conditions.

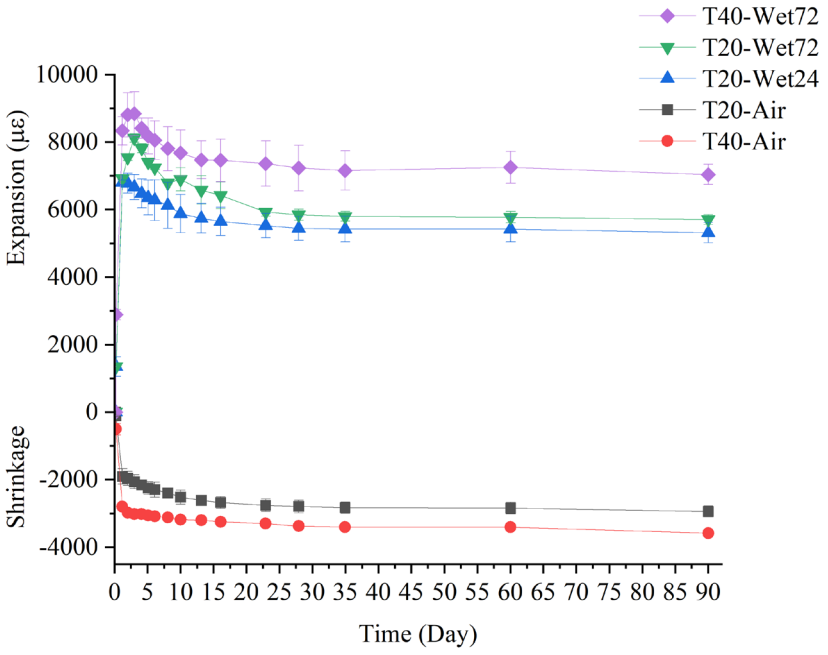

Figure 4-9. Shrinkage deformation of W20-C130 ECC under different curing conditions.

4.3.1.3 Effect of CSA contents

When it comes to the different contents of CSA, W20-C70, C100, and C130 ECC shows an expansion enhancement with increased CSA to PLC, consistent with that reported in the literature [28,33,47,58], no matter the curing conditions. The maximum expansion rose from 3141 με (W20-C70) to 5390 με and 8843 με (W20-C100 and C130 ECC) under T40-Wet72 curing. A similar trend can also be found in other curing conditions.

The expansive behavior of ECC with CSA is known to reverse after reaching a peak. To achieve the goal of long-term self-stressing, the expansion loss of ECC should be limited to 50% of its maximum expansion for promising self-stressing effect [33], which could be verified by free-length change tests. Table 4-5 shows the expansion characteristic for all W20 ECC with various CSA contents and curing conditions. It can be found that the expansion loss/maximum expansion ratios ($\frac{EL}{ME}$ ratio) for W20-C70 are greater than 50%, specifically, 83%, 59%, and 56% even under wet-curing conditions. In contrast, once the content of CSA exceeds 100, i.e., W20-C100 and W20-C130, the $\frac{EL}{ME}$ ratio are all controlled below 50% when wet-curing. For W20-C100, $\frac{EL}{ME}$ ratios are 43%, 41%, and 38%; For W20-C130 exhibits $\frac{EL}{ME}$ ratios of 22%, 30%, and 20%, showing a robust self-stressing effect. W20-C70 is then ruled out in this study, considering its lack of self-stressing behavior. It should be noted that although wet-curing W20-C100 and W20-C130 meet the self-stressing criteria, further investigation is needed to verify their workability.

Table 4-5. Expansion characteristics for W20 ECC mixtures.

Mixture	Maximum expansion*		Expansion at*		Expansion loss/maximum expansion
	Age (d)	(με)	28d (με)	90d (με)	
T20-Air-F100	1.18	178	-728	-1001	662%
T20-Air-C70	0.21	-699	-3459	-3675	-
T40-Air-C70	0.21	-1833	-4140	-4414	-
T20-Wet24-C70	1.14	2261	521	390	83%
T20-Wet72-C70	3.17	2989	1380	1221	59%
T40-Wet72-C70	1.14	3141	1575	1371	56%
T20-Air-C100	0.21	-216	-3006	-3166	-
T40-Air-C100	0.21	-542	-3319	-3552	-
T20-Wet24-C100	1.17	4056	2405	2295	43%
T20-Wet72-C100	3.16	5275	3361	3094	41%
T40-Wet72-C100	2.14	5390	3509	3318	38%
T20-Air-C130	0.21	-110	-2794	-2944	-
T40-Air-C130	0.21	-504	-3374	-3587	-
T20-Wet24-C130	1.18	6803	5444	5313	22%
T20-Wet72-C130	3.00	8115	5846	5704	30%
T40-Wet72-C130	3.00	8843	7231	7038	20%

* Positive and negative values represent expansion and shrinkage, respectively.

4.3.2 Working time window

The diameters were recorded within 30-minute intervals starting 30 minutes after water was added to ECC mixtures. The flow table tests were stopped once the spread diameters fell under 130 mm for in-site suitable workability [45], incorporated with the surface hardening of the ECC mixtures. The open working time windows could then be determined for each VA-ECC mix design.

Figure 4-10 illustrates the spread diameters for T20-Air-C100 ECC under distinct water-to-binder ratios of 0.18 (W18), 0.20 (W20), and 0.22 (W22). T20-Air-C100 ECC exhibits a reduction of spread diameter with a decrement in the water-to-binder ratio. W20 and W22 show comparable spread diameters of 165 mm at 30 minutes, while W18 demonstrates a reduction to 150 mm. As time progressed, the spread diameter diminished to 135 mm and 130 mm at 60 and 90 minutes, respectively. W20 and W22 maintain relatively larger spread diameters compared to W18. However, the spread diameter should increase significantly when the water-to-binder ratio increases [59,60]. W20 and W22 show equivalent spread diameters of 149 mm and 130 mm at 60 minutes and 139 mm and 142 mm at 90 minutes. This phenomenon can be attributed to the mitigated water reducer for W22 (from 32 to 20), which compensates for the increment, as the amount of water reducer also positively correlated to the mixtures' setting time and spread diameter [61]. It should be noted that the WR content for W18 is already 40 kg/m^3, making it ineffective to enhance workability by further increasing WR. Doing so would result in excessive cost and bleeding of cementitious matrix. Therefore, water-to-binder ratio of 0.18 (W18) is not considered suitable for this study due to its limited working time window. W20 may be more attractive for its greater strength compared to W22 with a comparable working time window.

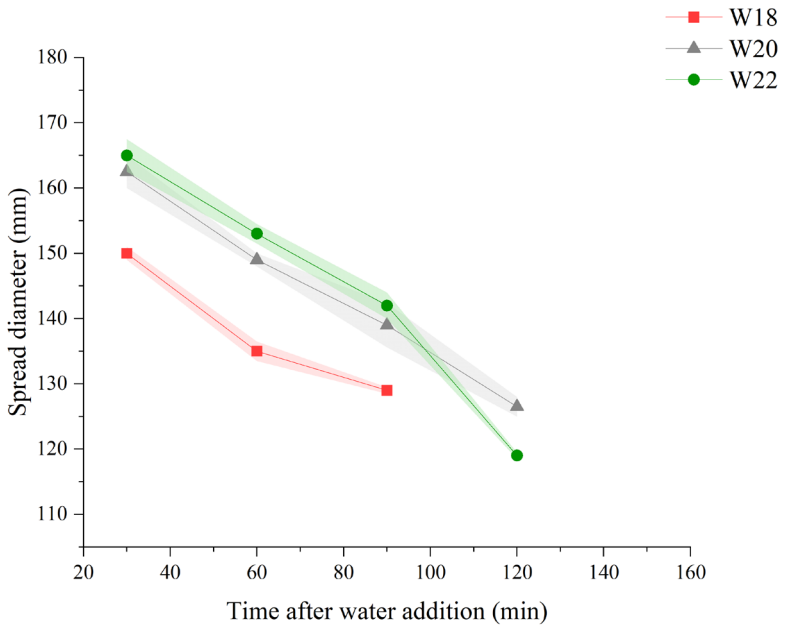

Figure 4-10. Spread diameter test results for T20-Air-C100 ECC. Shaded areas represent the range of experimental variability.

The results of flow table tests for W20-ECC with various CSA contents and curing temperatures are included in Figure 4-11. The diminution of spread diameters is noticeable in correlation with an increment of CSA contents for both 20℃ and 40℃ curing temperatures. A substantial effect of temperature on spread diameter is reported in previous literature [62]. The diameter of the T40-Air-C130 decreased drastically from 131 mm to 115 mm compared to T20-Air-C130. In addition, the open working time window for W20-C130 was shortened to less than 60 minutes at 40℃ curing conditions since the diameter already fell under the targeted 130 mm for in-field workability. 40℃ is a possible temperature when considering casting in the Middle East. In contrast, the working time window for W20-C100 is extended to 90 minutes at 40℃. Additionally, the spread diameter for W20-C100 retains slightly under 130 mm requirement for 127 mm at 120 minutes, which implies that W20-C100 can achieve nearly 2 hours of working time window at 20℃, representing that CSA dosage of 100 is more suitable considering the working time window than W20-C130.

Although both W20-C100 and W20-C130 exhibit self-stressing behaviors, considering their feasible open working time windows, W20-C100 will be a more favorable option for infrastructure construction in the Middle East. However, it should be emphasized that while the

spread diameter of W20-C70 fell under 130 mm after 150 and 120 minutes for 20℃ and 40℃ curing, showing a sufficient long working time window for applications, W20-C70 ECC is not a preferred choice due to its lack of self-stressing effect.

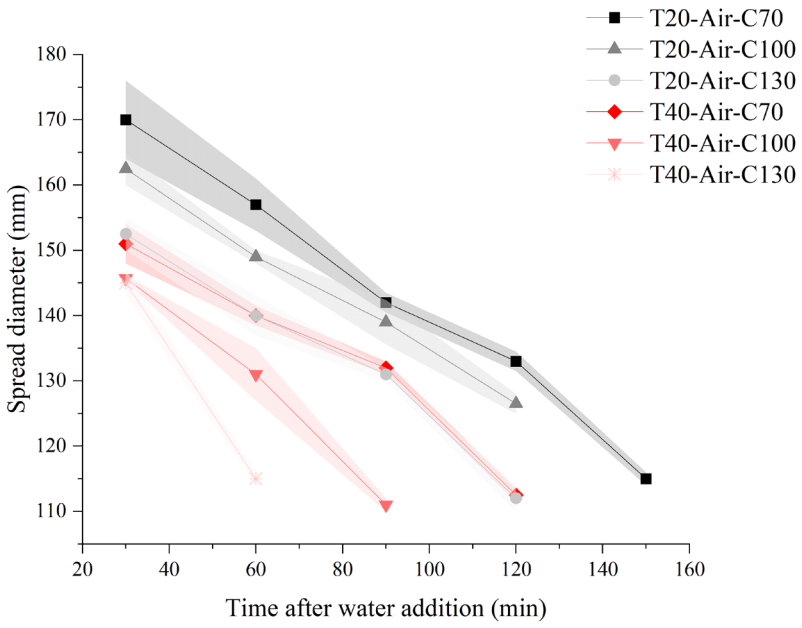

Figure 4-11. Spread diameter test results for W20 ECC. Shaded areas represent the range of experimental variability.

4.3.3 Mechanical performance

4.3.3.1 Compressive strength

Increasing the water-to-binder ratio reduces the compressive strength of ECC, which is identical to the behavior of conventional CSA cement concrete and ECC [63,64]. As shown in Figure 4-12(a), the 28 days compressive strength of T20-Air W18-C100 decreased from 48.3 MPa to 40.9 MPa (by 15%) for W20-C100. The compressive strength further diminished to 38.9 MPa (19% decrease) and 36.4 MPa (25% decrease) for W22-C100 and W24-C100, respectively. The compressive strength for W20-C100 ECC with different curing conditions at 28 days is shown in Figure 4-12(b), indicating that the wet-curing conditions lead to enhanced strength. Wet-curing promotes the hydration process, lowering the porosity and densifying the microstructure of the cementitious matrix, resulting in higher compressive strength development [65–67]. The strength

gain for wet-curing is approximately 13% for T20-Wet24, T20-Wet72, and T40-Wet72 compared to T20-Air ECC (from 48.3 MPa to 54.6MPa, 54.6MPa, and 53.6MPa at 28 days). Nevertheless, inadequate water supply associated with 40°C curing temperature was found to lower the compressive strength by 5% (from 40.9 MPa to 39.0 MPa at 28 days) for T40-Air ECC.

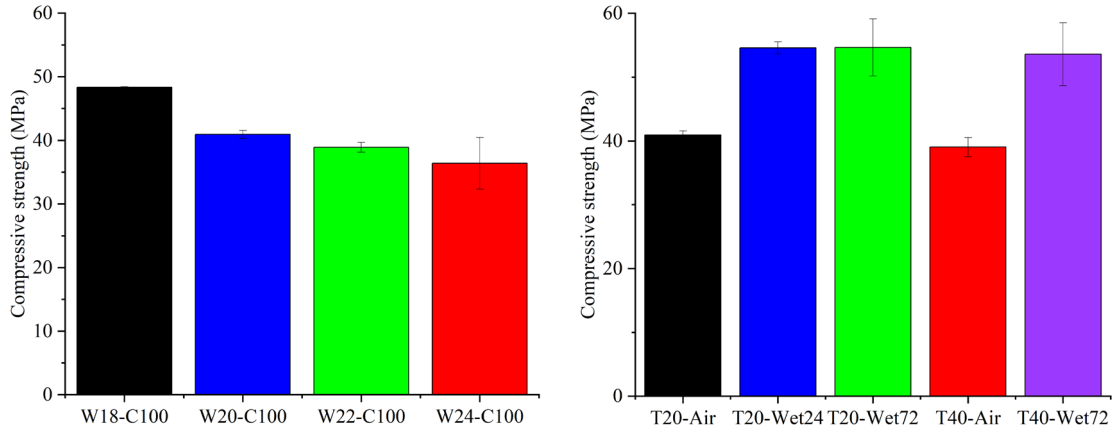

Figure 4-12. Compressive strength of C100 ECC with different (a) water/binder ratio, and (b) curing conditions at 28 days.

4.3.3.2 Tensile performance

The tensile stress-strain curves at 28 days are shown in Figure 4-13, and the tensile properties are summarized in Table 4-6. Like compressive strength, the tensile strength of T20-Air-C100 ECC decreased from 9.03 MPa for W18 to 8.29 MPa, 7.71 MPa, and 6.32 MPa for W20 (8% decrease), W22 (15% decrease), and W24 (30% decrease), respectively. The phenomenon for wet-curing also corresponds to compressive strength, the tensile strength of wet-cured ECC increased significantly (T20-Wet24, T20-Wet72, and T70-Wet72), while tensile strength T40-Air declined to 7.35 MPa from 8.29 MPa for T20-Air. It should be noted that the tensile strain capacity of wet-curing ECC was impaired due to the enhanced tensile strength, which may hinder the formation of multiple cracks. However, the tensile strain capacity still exceeds 4%, except for the T40-Wet72, attaining a promising strain capacity [6].

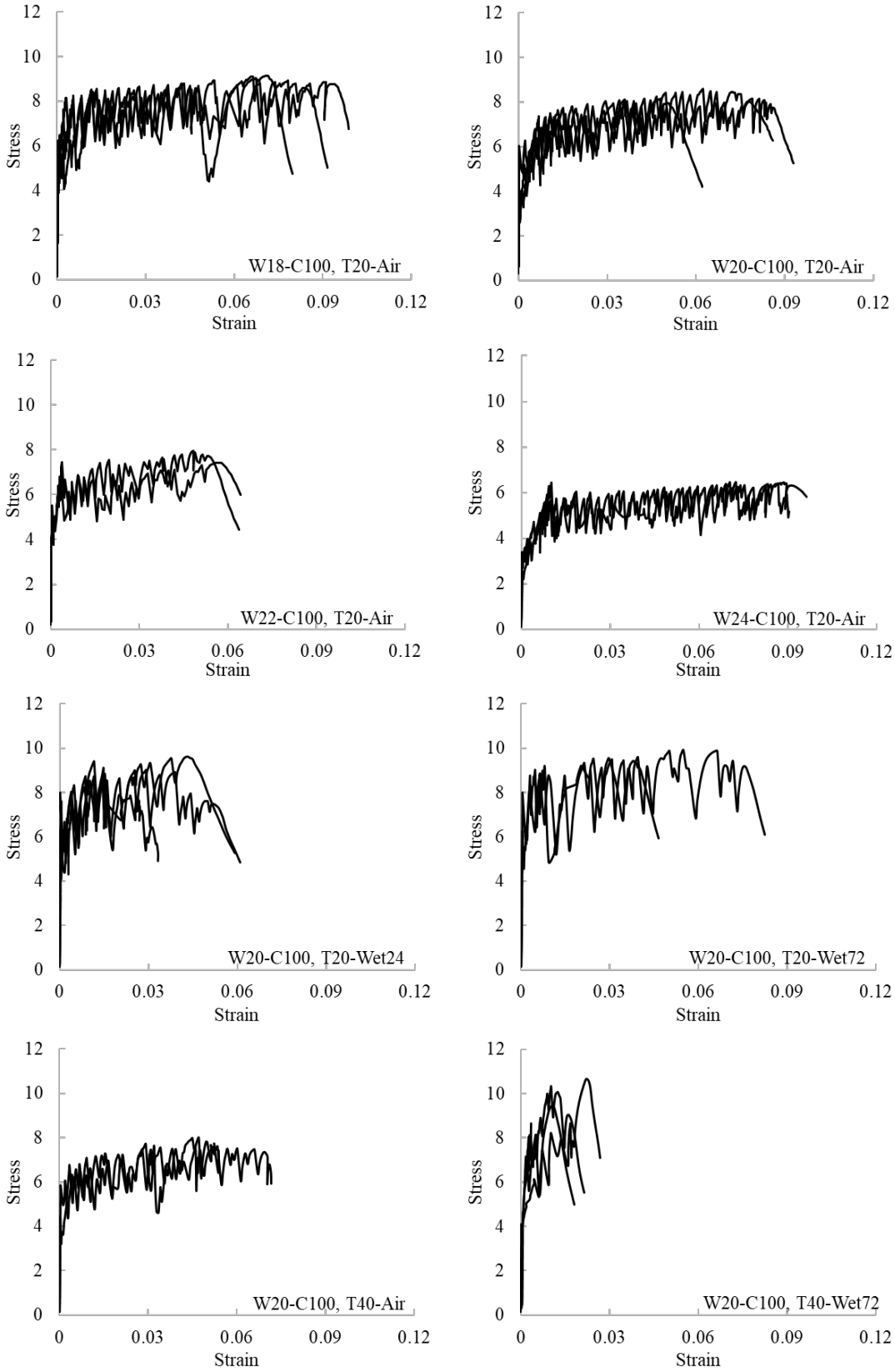

Figure 4-13. Tensile stress-strain curves at 28 days.

Table 4-6. Summary of tensile results.

Name	Ultimate tensile strength (MPa)	Tensile strain capacity (%)
W18, T20-Air	9.03 ± 0.51	7.17 ± 0.46
W20, T20-Air	8.29 ± 0.21	6.31 ± 1.26
W22, T20-Air	7.71 ± 0.42	5.62 ± 1.85
W24, T20-Air	6.32 ± 0.04	7.96 ± 0.72
T20-Wet24	9.35 ± 0.25	4.14 ± 0.27
W20-Wet72	9.42 ± 0.43	5.20 ± 1.40
T40-Air	7.35 ± 0.65	4.99 ± 0.32
T40-Wet72	10.15 ± 0.50	1.41 ± 0.56

4.3.3.3 Flexural performance

Consistent with the finding of compressive and tensile strength, flexural strength (MOR) of T20-Air-C100 ECC reduced contrary to the increment of water-to-binder ratio, as shown in Figure 4-14. Flexural strength-deflection curves at 28 days are portrayed in Figure 4-15. The MOR decreased from 14.0 MPa for W18 to 12.5 MPa and 12.0 MPa for W20 (11% decrease) and W22 (14% decrease), respectively. Although W24 shows a MOR of 9.3 MPa (34% decrease), it still maintains a considerable advantage with a MOR of around 80% higher than conventional concrete. This is noteworthy considering that the MOR of traditional concrete and FA-ECC typically falls below 5 MPa [68–72] and 5-10 MPa [73–75], respectively, which makes the developed ECC competitive.

The curing condition of T40-Air also impaired the MOR of W20-C100 by 13% (from 12.5 MPa to 10.9 MPa) due to the accelerated evaporation of water that should be used for hydration. In contrast, other curing conditions, wet-curing, benefit the MOR. The MOR increased to 14.7

MPa, 14.8MPa, and 16.9 MPa for T20-Wet24 (18% increase), T20-Wet72 (18% increase), and T40-Wet72 (35% increase), respectively.

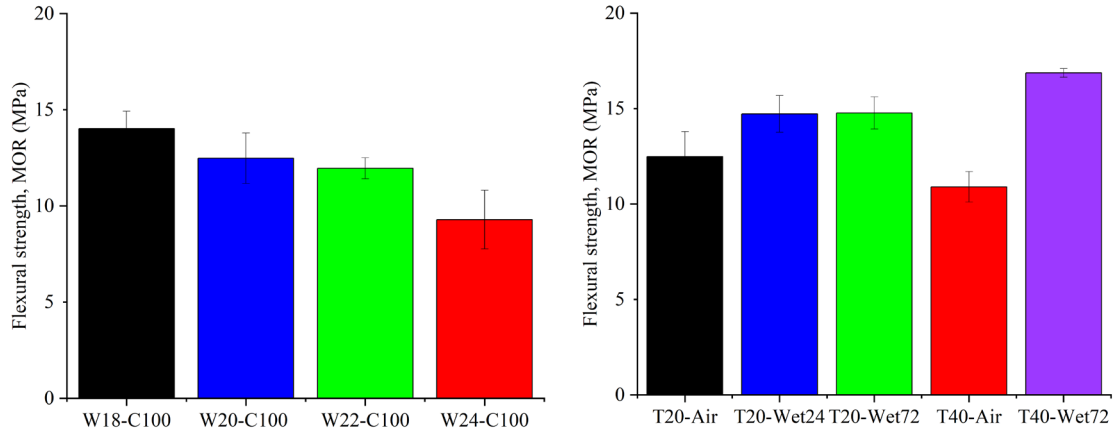

Figure 4-14. Flexural strength (MOR) of C100 ECC with different (a) water/binder ratio, and (b) curing conditions at 28 days.

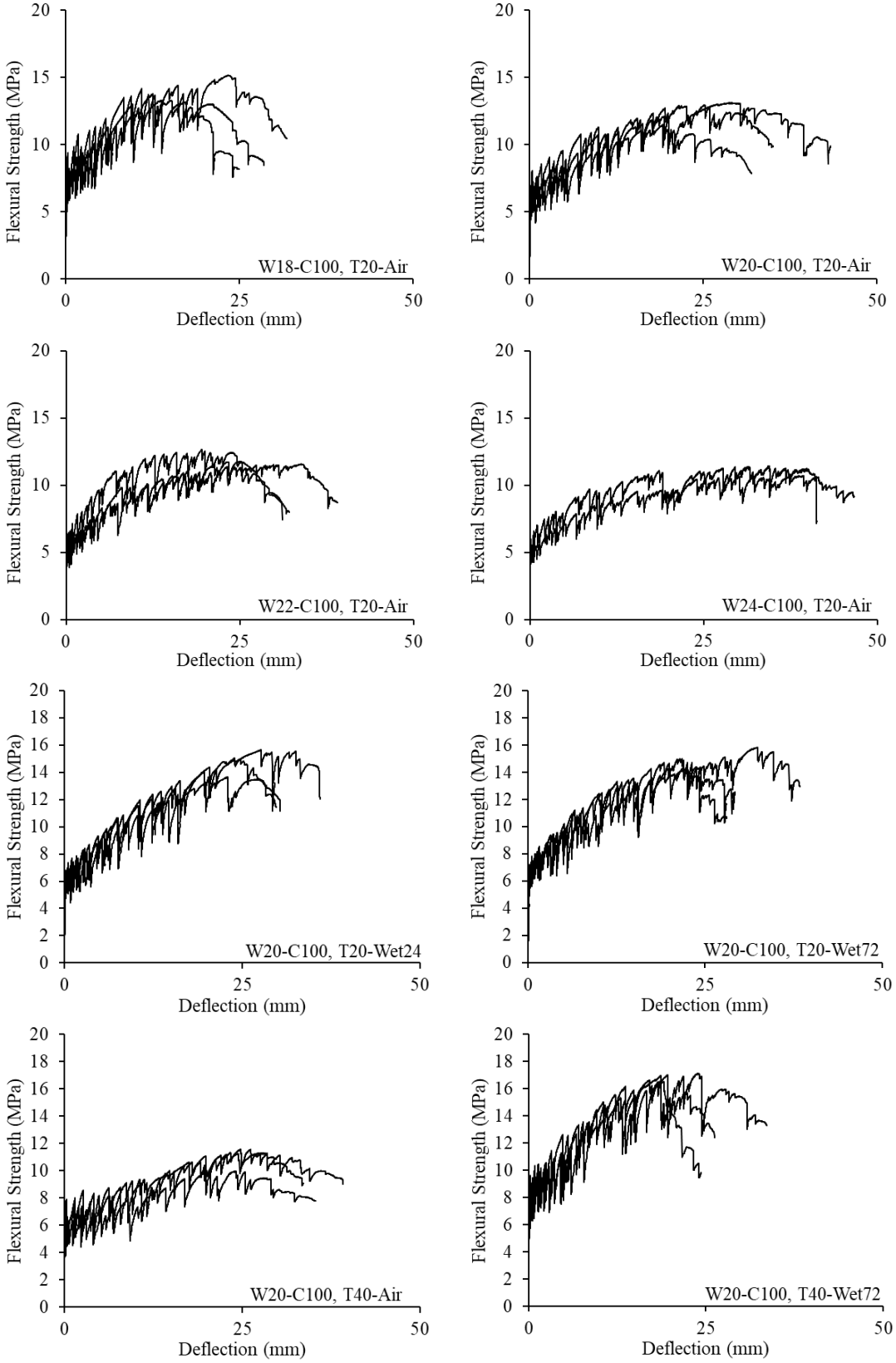

Figure 4-15. Flexural strength-deflection curves at 28 days.

4.3.4 Crack patterns and crack width distribution

Figure 4-16 illustrates the crack patterns in the narrow-gauge region (80 mm long, as shown in Figure 4-3(a)) of the ECC dogbone-shaped specimens. Typical specimens were selected to represent the crack patterns at failure with different water-to-binder ratios (T20-Air W18, W20, W22, and W24) and curing conditions (W20-C100 T20-Air, T20-Wet24, T20-Wet72, T40-Air, and T40-Wet72). The results indicate that the ECC with various water-to-binder ratios demonstrates multiple micro-cracking patterns. There are no significant variations of crack numbers with different water-to-binder ratios. However, the increased strength of the ECC induced by wet-curing limits crack initiation and propagation, and fewer cracks were observed when the curing conditions T20-Wet24, T20-Wet72, and T40-Wet72 were applied, especially for the T40-Wet72 specimen with only 5 cracks.

The crack number distribution of different C100 ECC at specimen failure is shown in Figure 4-17. The average crack width for air-cured specimens tight, specifically 64.1μm, 62.7μm, and 67.2 μm for W20, W22, and W24, respectively. Despite the crack numbers reduced after wet-curing, the average cracks width of T20-Wet24 and T20-Wet72 are still below 100 μm with 84.4 μm and 94.1 μm, respectively, which is comparable to conventional ECC that range from 70 μm to 120 μm [76–78] and the suggested criteria of <100 μm to maintain high durability [79]. In contrast, the average crack width and the tensile strain capacity for T40-Wet72 are 156 μm and 1.41%. Thus, long curing time (72 hours) at high temperature is not recommended is not recommended for further infrastructure applications.

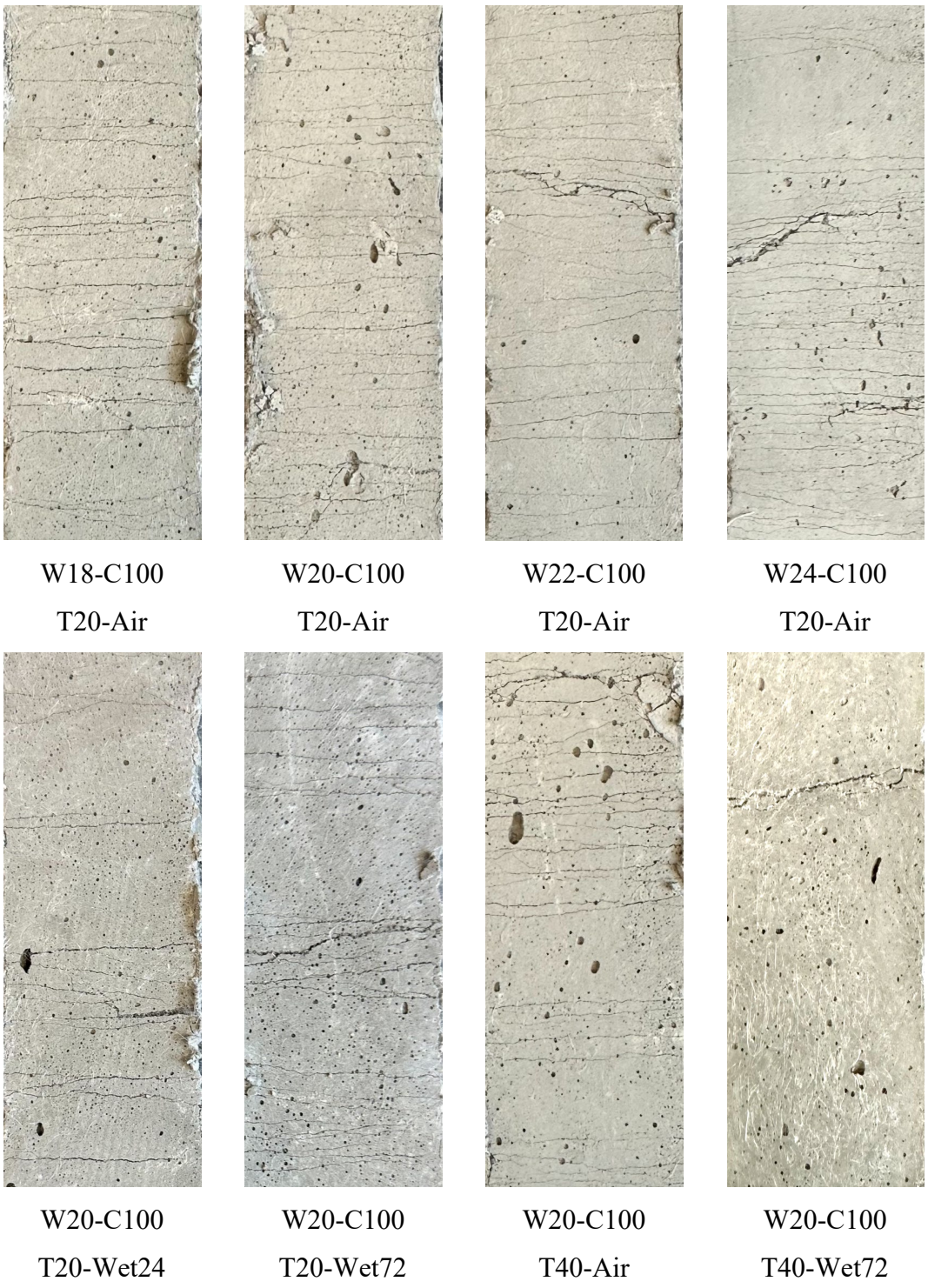

Figure 4-16. Representative crack patterns for ECC at failure with different water/binder ratios and curing conditions.

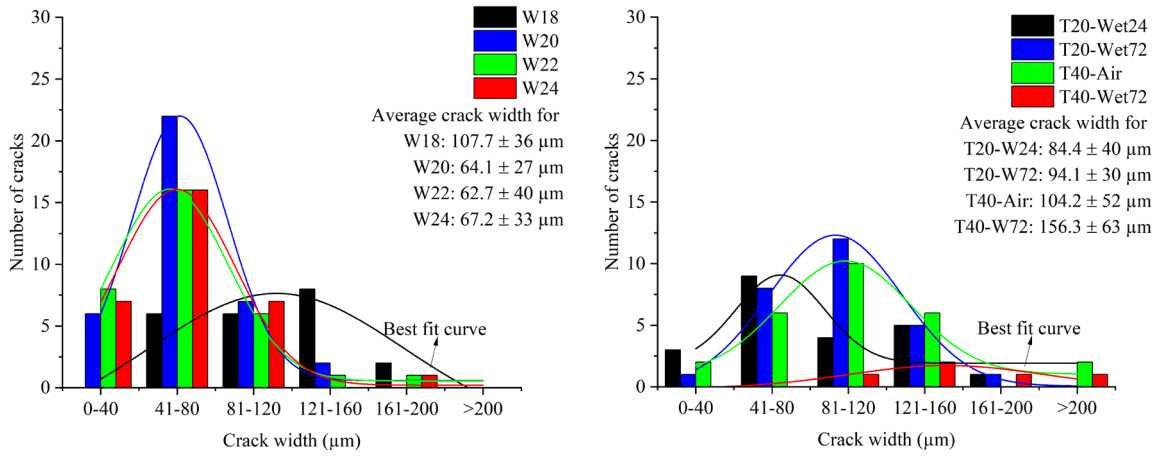

Figure 4-17. The crack number distribution of different C100 ECC at specimen failure, showing the effect of (a) water/binder ratio, and (b) curing conditions.

4.3.5 Micro/mechanism analysis

Figure 4-18 depicts the XRD patterns results. As per Eq. (2) in section 3.1, the reaction between anhydrite ($C\bar{S}$) and water with ye'elimite ($C_4A_3\bar{S}$) leads to the formation of ettringite ($C_3A \cdot 3C\bar{S} \cdot H_{32}$). XRD patterns indicate that the anhydrite peaks are notably higher in T20-Air-C100 ECC compared to T20-Air-F100 and T20-Wet24-C100. This observation suggests an insufficient amount of water available to react with anhydrite and form ettringite. Moreover, the XRD pattern demonstrates a pronounced increase in CH formation in T20-Air-C100, indicating that water was utilized to form CH from CaO. Therefore, the formation of ettringite in T20-Air-C100 is significantly lower than T20-Air-F100 and T20-Wet24-C100, as indicated by XRD analysis.

The results confirmed that the water supply for air-cured specimens is insufficient due to the competition from a higher content of CaO and greater water consumption caused by the angular particle shape of VA compared to FA. Thus, a suitable curing treatment, such as wet-curing, which provides sufficient water, emerges as an effective solution, as demonstrated in this study. This approach can compensate for the more significant shrinkage observed in the air-cured VA-ECC and facilitate the development of a self-stressing ECC that utilizes locally available materials.

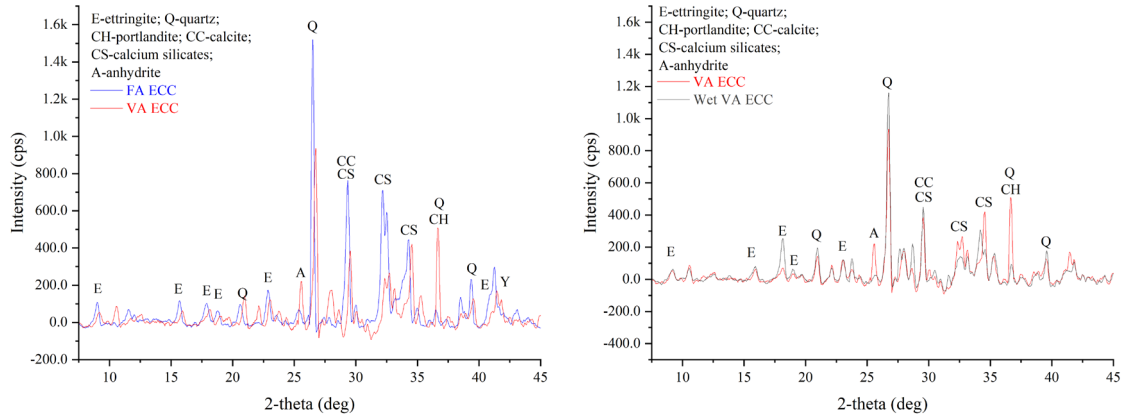

Figure 4-18. XRD patterns of the (a)T20-Air W20-F100 and W20-C100, and (b) T20-Air and T20-Wet24 W20-C100 ECC.

4.3.6 Pavement application, carbon footprint, and cost evaluation

To evaluate the sustainability of the localized materials DS-VA-ECC, the CO_2 emission and cost during the manufacturing process of the ECC ingredients are listed in Table 4-7. It should be emphasized that the material cost may change over time. FA and VA were assumed to be the industrial waste materials in this study with a zero embodied carbon footprint. However, for the Middle East, the transportation-related CO_2 footprints and costs should be included in FA and silica sand. As the average cargo transportation distance of 5571 kilometers to import FA [80] into the Middle East, incorporating the CO_2 emission of 3.67 to 5.61 g CO_2/t-km [81] and cost of 15.4 to 18.5 USD/t [82], specifically 16 USD/t provided by manufacturer, for FA, the additional 31.3 kg/t and 16 USD/t of CO_2 emission and cost should be included for FA and silica sand.

Embodied carbon footprint and cost of conventional concrete [16] were used as a benchmark to evaluate the sustainability of localized ECC in this study, as shown in Figure 4-19 and Figure 4-20. Shifting from the use of FA and silica sand to localized materials, namely VA and DS, the carbon footprint and cost (549 kg CO_2/m^3 and 354 USD/m^3) of VA-C100 were found to decrease compared to that of FA-silica sand ECC (585 kg CO_2/m^3 and 411 USD/m^3), while still higher than conventional concrete (341 kg CO_2/m^3 and 89 USD/m^3). The primary CO_2 emissions and costs in ECC are the high cement content and the use of synthetic fiber. As a result, even with the substitution of FA and silica sand with localized materials, the material costs and carbon

emissions for W20-C100 ECC remain higher than concrete. There is a 5% CO_2 emission and 14% cost reduction for VA-ECC compared to FA-ECC. It should be noted that this analysis disregards the increased MOR of VA-ECC compared to FA-ECC and conventional concrete, which would substantially reduce the costs and embodied carbon footprint of VA-ECC in practical field applications.

Using pavement construction as an example, the implementation of VA-ECC can significantly reduce the required volume of materials. The developed self-stressing localized DS-VA ECC, i.e., W20-C100, with 24 or 72 hours of 20℃ wet-curing, shows promising MOR and ample working time windows. The MOR values for W20-C100 (14.7 MPa and 14.8MPa for T20-Wet24 and T20-Wet72) are nearly three times and 1.5 times higher than conventional concrete and FA-ECC [68–75]. Consequently, this translates to a reduction of 42% and 18% in required pavement thickness. Figure 4-21 illustrates the materials embodied carbon footprint and costs for pavement construction for each 1 km^2 of pavement (surface area). Take the minimum recommended pavement thickness of 0.15 m for concrete [83–85] as an example, concrete pavement requires 150000 m^3 of material, while FA-ECC and VA-ECC necessitate 106500 m^3 and 87000 m^3, respectively. The embodied carbon footprint and costs for wet-cured W20-C100 (48 million kg CO_2 and 31 million USD) have been reduced by 22% and 30% compared to FA-ECC (62 million kg CO_2 and 44 million USD). Furthermore, the carbon footprint of VA-ECC is 7% below that of traditional concrete. At the same time, its high tensile ductility, MOR, and self-stressing properties contribute to its competitive advantage as a localized material.

Table 4-7. The carbon emission and material cost for ingredients of ECC production.

Component	CO_2 emission (kg/t)	Cost (USD/t)
PLC	815 [a]	45-67 [b]
CSA	588 [c]	33-40 [d]
FA	31.3 [e]	120 [b]
VA [b]	0	104
DS [b]	23.3	5
Silica sand [e]	54.6	79.9
WR [e]	1667	1211
PE fiber	2000 [e]	22000 [b]
PP fiber	3100 [e]	3500 [b]

[a] CO_2 emission of PLC was reduced to 90% compared to OPC in [86] according to [87].

[b] Provided by the manufacturer.

[c] CO_2 emission of CSA cement was reduced to 65% compared to OPC in [86] according to [88].

[d] Data from [88,89], where the exchange rate of 1:1.08 for euros and USD is used in this study.

[e] Data from [90–92], where cost and CO_2 emission of FA and silica sand included the transportation fee and CO_2 emissions [80–82].

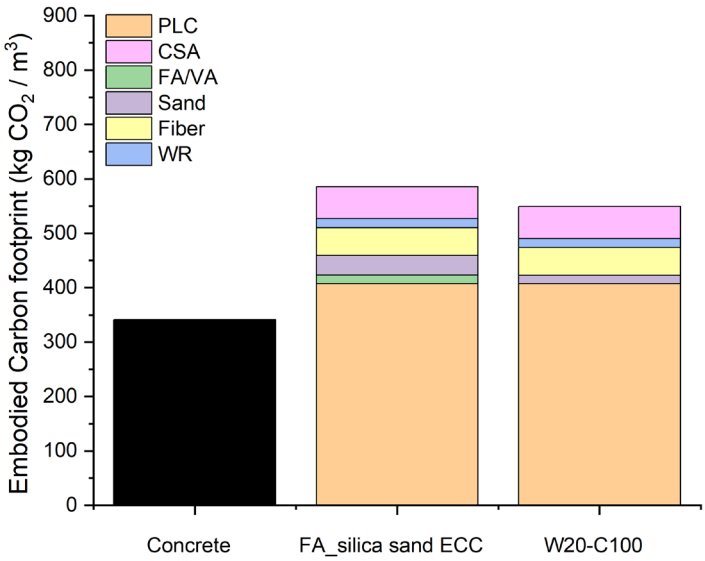

Figure 4-19. Contributions of embodied carbon footprint by ingredients of FA-silica sand ECC and W20-C100 ECC.

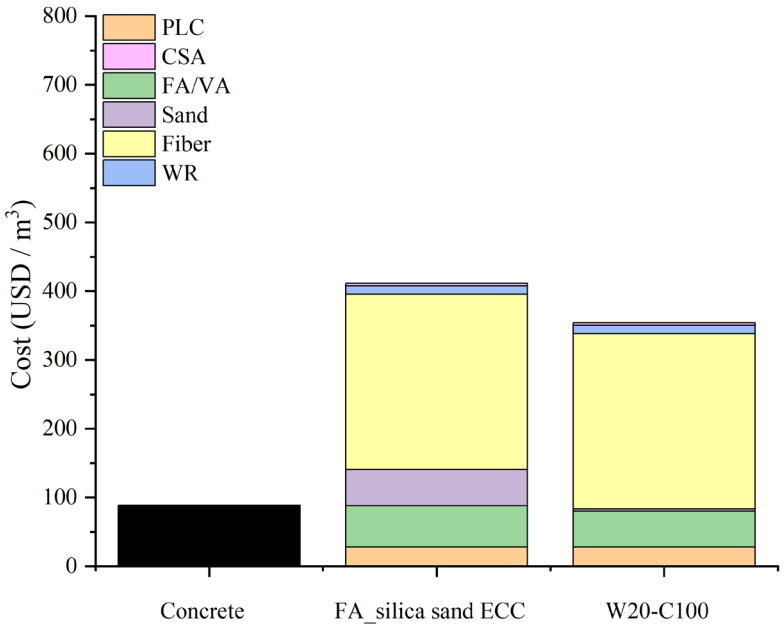

Figure 4-20. Contributions of costs by ingredients of FA-silica sand ECC and W20-C100 ECC.

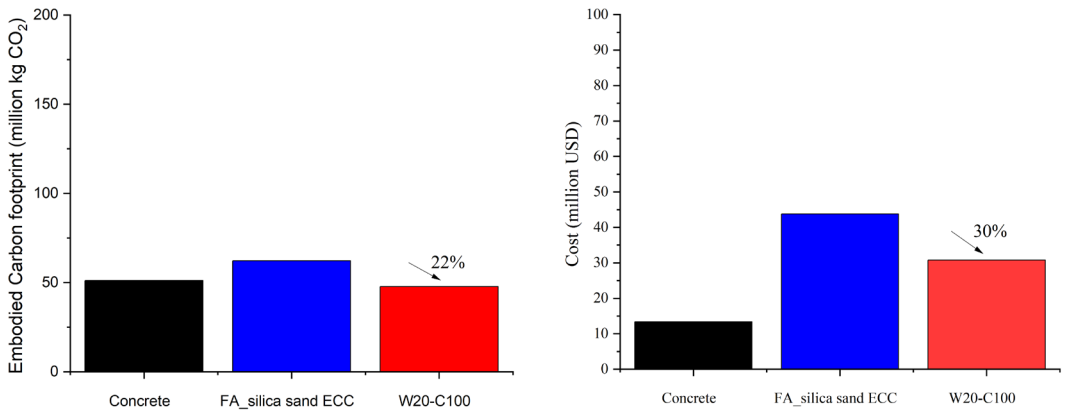

(a) (b)

Figure 4-21. Materials (a) embodied carbon footprint and (b) costs of pavement for concrete, FA-silica sand ECC and wet-curing W20-C100 ECC.

4.4. Conclusions

A self-stressing ECC has been developed utilizing locally available materials, volcanic ash (VA) and desert sand (DS), incorporating low-content calcium sulphoaluminate (CSA) cement under water curing strategy. Offering a potential pavement material for the Middle East with substantial mechanical performance and lower embodied carbon footprint than concrete and other fly ash ECC when considering the pavement application. Based on the results of mechanical performance tests, free length change tests, and XRD analysis, as well as sustainability evaluations, the following conclusions can be derived:

1. Wet-curing can compensate for the increased shrinkage from incorporating volcanic ash VA (replacing fly ash FA) by providing additional external water to meet the high water demand of VA. Consequently, a self-stressing expansion VA-ECC is achieved through wet curing in the case of W20-C100 and W20-C130 mixtures.
2. Increasing the calcium sulphoaluminate CSA content reduces the working time window. Given that the working time window for W20-C130 is limited to 90 minutes at room temperature, W20-C100 is more suitable for practical applications, offering a longer working time of 120 minutes.
3. The mechanical performance of VA-ECC is comparable to that of FA-ECC. Wet-curing enhances the strength of VA-ECC by providing ample water for the hydration process. Conversely, high-temperature air-cured conditions impaired the strength of VA-ECC.

4. The designed wet-cured W20-C100 mixture attains a 14.7 MPa of MOR, surpassing the performance of conventional concrete. As a result, the pavement thickness can be reduced by up to 42% when employing this VA-ECC than conventional concrete, leading to a 7% reduction in embodied carbon footprint. Additionally, compared to FA-ECC, the developed VA-ECC demonstrates further reductions in embodied carbon footprint and costs of 22% and 30%.

The substitution of FA and silica sand with local materials, VA and DS, results in a 7% reduction in CO_2 emissions for pavement applications, with the potential for further enhancements to align with the approach discussed in Chapter 2. Further investigations are required for the carbon sequestration approach involving carbonation curing, which holds promise for implementation in VA-ECC. Although the cost of localized materials ECC remains higher than that of conventional concrete, the gap between them is expected to diminish in the future due to the projected inflation of FA and silica sand, which make this VA-ECC more competitive alternative.

4.5. References

[1] H. Wang, Life-cycle analysis of repair of concrete pavements, in: Eco-Efficient Repair and Rehabilitation of Concrete Infrastructures, Elsevier Inc., 2018: pp. 723–738. https://doi.org/10.1016/B978-0-08-102181-1.00025-3.

[2] M. Al-Jabari, R. Al-Rashed, M.E. Ayers, D. Clement, Materials selection and proportioning for watertight and durable concrete, in: Integral Waterproofing of Concrete Structures: Advanced Protection Technologies of Concrete by Pore Blocking and Lining, Elsevier, 2022: pp. 109–134. https://doi.org/10.1016/B978-0-12-824354-1.00004-0.

[3] U.S. Department of Transportation Federal Highway Administration, Table HM-12 Highway statistics 2020, (2020).

[4] National Asphalt Pavement Association, The Asphalt Pavement Industry Fast Facts, 2020. https://doi.org/10.13140/RG.2.2.21946.82888.

[5] S. Tayabji, D. Ye, N. Buch, Precast concrete pavements: Technology overview and technical considerations, PCI Journal. 58 (2013) 112–128. https://doi.org/10.15554/pcij.01012013.112.128.

[6] V.C. Li, Engineered Cementitious Composites – Bendable Concrete for Sustainable and Resilient Infrastructure, Springer, Germany, 2019. https://doi.org/10.1007/978-3-662-58438-5.

[7] E. Cuenca, F. Lo Monte, M. Moro, A. Schiona, L. Ferrara, Effects of autogenous and stimulated self-healing on durability and mechanical performance of uhpfrc: Validation of tailored test method through multi-performance healing-induced recovery indices, Sustainability (Switzerland). 13 (2021). https://doi.org/10.3390/su132011386.

[8] H. Liu, Q. Zhang, V. Li, H. Su, C. Gu, Durability study on engineered cementitious composites (ECC) under sulfate and chloride environment, Constr Build Mater. 133 (2017) 171–181. https://doi.org/10.1016/j.conbuildmat.2016.12.074.

[9] M.D. Lepech, V.C. Li, Water permeability of engineered cementitious composites, Cem Concr Compos. 31 (2009) 744–753. https://doi.org/10.1016/j.cemconcomp.2009.07.002.

[10] P. Suthiwarapirak, T. Matsumoto, Fiber Bridging Degradation Based Fatigue Analysis of ECC under Flexure, J Appl Mech. 6 (2003) 1179–1188. https://doi.org/10.2208/journalam.6.1179.

[11] T. Matsumoto, P. Suthiwarapirak, T. Kanda, Mechanisms of Multiple Cracking and Fracture of DFRCC under Fatigue Flexure, Journal of Advanced Concrete Technology. 1 (2003) 299–306. https://doi.org/10.3151/jact.1.299.

[12] W.H. Hu, D. Zhang, B.R. Ellis, V.C. Li, The Impact of Carbonation Curing on the Fatigue Behavior of Polyvinyl Alcohol Engineered Cementitious Composites (PVA-ECC), Journal of Advanced Concrete Technology. 21 (2023) 322–336. https://doi.org/10.3151/jact.21.322.

[13] M.D. Lepech, V.C. Li, Application of ECC for bridge deck link slabs, in: Materials and Structures/Materiaux et Constructions, 2009: pp. 1185–1195. https://doi.org/10.1617/s11527-009-9544-5.

[14] H. Ma, Z. Zhang, Paving an engineered cementitious composite (ECC) overlay on concrete airfield pavement for reflective cracking resistance, Constr Build Mater. 252 (2020). https://doi.org/10.1016/j.conbuildmat.2020.119048.

[15] S. Qian, V. Li, Durable Pavement with ECC, in: 1st International Conference on Microstructure Related Durability of Cementitious Composites, 2011. https://www.researchgate.net/publication/280229384.

[16] D. Shoji, Z. He, D. Zhang, V.C. Li, The greening of engineered cementitious composites (ECC): A review, Constr Build Mater. 327 (2022). https://doi.org/10.1016/j.conbuildmat.2022.126701.

[17] A.A. Bahraq, M. Maslehuddin, S.U. Al-Dulaijan, Macro- and Micro-Properties of Engineered Cementitious Composites (ECCs) Incorporating Industrial Waste Materials: A Review, Arab J Sci Eng. 45 (2020) 7869–7895. https://doi.org/10.1007/s13369-020-04729-7.

[18] E.H.Yang, Y.Yang, V.C.Li, Use of high volumes of fly ash to improve ECC mechanical properties and material greenness, ACI Mater. J. 104 (2007) 620–628.

[19] E. Ghafari, D. Feys, K. Khayat, Feasibility of using natural SCMs in concrete for infrastructure applications, Constr Build Mater. 127 (2016) 724–732. https://doi.org/10.1016/j.conbuildmat.2016.10.070.

[20] I. Diaz-Loya, M. Juenger, S. Seraj, R. Minkara, Extending supplementary cementitious material resources: Reclaimed and remediated fly ash and natural pozzolans, Cem Concr Compos. 101 (2019) 44–51. https://doi.org/10.1016/j.cemconcomp.2017.06.011.

[21] S. Dietmar, A.R. Mohamed Jameel, Middle East Power Outlook 2035, 2017.

[22] W. Matar, R. Echeverri, A. Pierru, The Prospects for Coal-fired Power Generation in Saudi Arabia, 2015.

[23] K.M.A. Hossain, M. Lachemi, Strength, durability and micro-structural aspects of high performance volcanic ash concrete, Cem Concr Res. 37 (2007) 759–766. https://doi.org/10.1016/j.cemconres.2007.02.014.

[24] J.C. Liu, M.U. Hossain, S.T. Ng, H. Ye, High-performance green concrete with high-volume natural pozzolan: Mechanical, carbon emission and cost analysis, Journal of Building Engineering. 68 (2023). https://doi.org/10.1016/j.jobe.2023.106087.

[25] H. Zhu, W.-H. Hu, M. Mehthel, T. Villette, O.S. Vidal, W.N. Nasser, V.C. Li, Engineered cementitious composites (ECC) with a high volume of volcanic ash: Rheological, mechanical, and micro performance, Cem Concr Compos. 139 (2023) 105051. https://doi.org/10.1016/j.cemconcomp.2023.105051.

[26] S. Gao, Z. Wang, W. Wang, H. Qiu, Effect of shrinkage-reducing admixture and expansive agent on mechanical properties and drying shrinkage of Engineered Cementitious Composite (ECC), Constr Build Mater. 179 (2018) 172–185. https://doi.org/10.1016/j.conbuildmat.2018.05.203.

[27] Y. Xiong, Y. Yang, S. Fang, D. Wu, Y. Tang, Experimental Research on Compressive and Shrinkage Properties of ECC Containing Ceramic Wastes Under Different Curing Conditions, Front Mater. 8 (2021). https://doi.org/10.3389/fmats.2021.727273.

[28] H. Zhu, D. Zhang, Y. Wang, T. Wang, V.C. Li, Development of self-stressing Engineered Cementitious Composites (ECC), Cem Concr Compos. 118 (2021). https://doi.org/10.1016/j.cemconcomp.2021.103936.

[29] K.M.A. Hossain, M. Lachemi, Strength, durability and micro-structural aspects of high performance volcanic ash concrete, Cem Concr Res. 37 (2007) 759–766. https://doi.org/10.1016/j.cemconres.2007.02.014.

[30] W. Chen, H.J.H. Brouwers, Hydration of mineral shrinkage-compensating admixture for concrete: An experimental and numerical study, Constr Build Mater. 26 (2012) 670–676. https://doi.org/10.1016/j.conbuildmat.2011.06.070.

[31] B.C. Acarturk, I. Sandalci, N.M. Hull, Z. Basaran Bundur, L.E. Burris, Calcium sulfoaluminate cement and supplementary cementitious materials-containing binders in self-healing systems, Cem Concr Compos. 141 (2023) 105115. https://doi.org/10.1016/j.cemconcomp.2023.105115.

[32] L.E. Burris, K.E. Kurtis, Influence of set retarding admixtures on calcium sulfoaluminate cement hydration and property development, Cem Concr Res. 104 (2018) 105–113. https://doi.org/10.1016/j.cemconres.2017.11.005.

[33] H. Zhu, D. Zhang, T. Wang, M. McBain, V.C. Li, Intrinsic self-stressing and low carbon Engineered Cementitious Composites (ECC) for improved sustainability, Cem Concr Res. 149 (2021). https://doi.org/10.1016/j.cemconres.2021.106580.

[34] M.P. Adams, J.H. Ideker, Volume Stability of Calcium Aluminate Cement and Calcium Sulfoaluminate Cement Systems Rapid Repair Materials View project Multi-Physics Numerical Simulation of Corrosion and Service Life Evaluation of HPFRCCS View project, (2014). https://doi.org/10.13140/RG.2.1.2344.3920.

[35] A.N. Markosian, R. Thomas, M. Maguire, A. Sorensen, Calcium Sulfoaluminate Cement Concrete for Prestressed Bridge Girders: Prestressing Losses, Bond, and Strength Behavior (MPC-19-401), 2019.

[36] D. Meng, T. Huang, Y.X. Zhang, C.K. Lee, Mechanical behaviour of a polyvinyl alcohol fibre reinforced engineered cementitious composite (PVA-ECC) using local ingredients,

Constr Build Mater. 141 (2017) 259–270. https://doi.org/10.1016/j.conbuildmat.2017.02.158.

[37] J. Che, R. Yang, J. Wang, H. Liu, Y. Hu, S.I. Doh, Research on basic mechanical properties of different modulus alkaline excited ECC, Physics and Chemistry of the Earth. 128 (2022). https://doi.org/10.1016/j.pce.2022.103233.

[38] J. Che, D. Wang, H. Liu, Y. Zhang, Mechanical properties of desert sand-based fiber reinforced concrete (DS-FRC), Applied Sciences (Switzerland). 9 (2019). https://doi.org/10.3390/app9091857.

[39] J. Che, Z. Guo, Q. Li, H. Liu, Mechanical Properties of Desert-Sand-Based Steel-PVA Hybrid Fiber Reinforced Engineered Cementitious Composites (H-DSECC), KSCE Journal of Civil Engineering. 26 (2022) 5160–5172. https://doi.org/10.1007/s12205-022-1746-1.

[40] H. Yokota, K. Rokugo, N. Sakata, Recommendations for Design and Construction of High Performance Fiber Reinforced Cement Composite with Multiple Fine Cracks, Japan Society of Civil Engineers. (2008).

[41] ASTM, Standard Test Method for Flexural Properties of Unreinforced and Reinforced Plastics and Electrical Insulating Materials by Four-Point Bending, American Society for Testing and Materials. 02 (2017) 1–9. https://doi.org/10.1520/D6272-17E01.1.

[42] ASTM, Standard Test Method for Compressive Strength of Hydraulic Cement Mortars (Using 2-in. or [50-mm] Cube Specimens) 1, ASTM. (2020). https://doi.org/10.1520/C0109_C0109M-20.

[43] ASTM, Standard Practice for Use of Apparatus for the Determination of Length Change of Hardened Cement Paste, Mortar, and Concrete 1, ASTM. (2007). www.astm.org.

[44] ASTM, Standard Test Method for Flow of Hydraulic Cement Mortar, ASYM. (2020). https://doi.org/10.1520/C1437.

[45] L. Gündüz, M. Bekar, N. Şapci, Influence of a new type of additive on the performance of polymer-lightweight mortar composites, Cem Concr Compos. 29 (2007) 594–602. https://doi.org/10.1016/j.cemconcomp.2007.03.007.

[46] J. Zhang, C. Gong, Z. Guo, M. Zhang, Engineered cementitious composite with characteristic of low drying shrinkage, Cem Concr Res. 39 (2009) 303–312. https://doi.org/10.1016/j.cemconres.2008.11.012.

[47] W.C. Choi, H. Do Yun, Effect of expansive admixtures on the shrinkage and mechanical properties of high-performance fiber-reinforced cement composites, The Scientific World Journal. 2013 (2013). https://doi.org/10.1155/2013/418734.

[48] S.J. Jang, J.H. Kim, S.W. Kim, W.S. Park, H. Do Yun, The effect of shrinkage-compensation on the performance of strain-hardening cement composite (SHCC), Sustainability (Switzerland). 11 (2019). https://doi.org/10.3390/su11051453.

[49] I.A. Chen, C.W. Hargis, M.C.G. Juenger, Understanding expansion in calcium sulfoaluminate-belite cements, Cem Concr Res. 42 (2012) 51–60. https://doi.org/10.1016/j.cemconres.2011.07.010.

[50] F. Winnefeld, B. Lothenbach, Hydration of calcium sulfoaluminate cements - Experimental findings and thermodynamic modelling, Cem Concr Res. 40 (2010) 1239–1247. https://doi.org/10.1016/j.cemconres.2009.08.014.

[51] J. Bizzozero, C. Gosselin, K.L. Scrivener, Expansion mechanisms in calcium aluminate and sulfoaluminate systems with calcium sulfate, Cem Concr Res. 56 (2014) 190–202. https://doi.org/10.1016/j.cemconres.2013.11.011.

[52] S. Allevi, M. Marchi, F. Scotti, S. Bertini, C. Cosentino, Hydration of calcium sulphoaluminate clinker with additions of different calcium sulphate sources, Materials and Structures/Materiaux et Constructions. 49 (2016) 453–466. https://doi.org/10.1617/s11527-014-0510-5.

[53] W. Suaris, S.P. Shah, M. Asce, Properties of concrete subjected to impact, Journal of Structural Engineering. 109 (1983) 1527–1760.

[54] A.M. Brandt, Cement-Based Composites Materials, mechanical properties and performance, Second edition, Taylor & Francis, 2009.

[55] M. Nasir, O.S.B. Al-Amoudi, H.J. Al-Gahtani, M. Maslehuddin, Effect of casting temperature on strength and density of plain and blended cement concretes prepared and

cured under hot weather conditions, Constr Build Mater. 112 (2016) 529–537. https://doi.org/10.1016/j.conbuildmat.2016.02.211.

[56] M. Soutsos, F. Kanavaris, The modified nurse-saul (MNS) maturity function for improved strength estimates at elevated curing temperatures, Case Studies in Construction Materials. 9 (2018). https://doi.org/10.1016/j.cscm.2018.e00206.

[57] I. Elkhadiri, M. Palacios, F. Puertas, Effect of curing temperature on cement hydration, Ceramics – Silikáty. 53 (2009) 65–75.

[58] Y. Chen, J. Yao, Z. Lu, C.K.Y. Leung, Experimental study on the shrinkage reduction of high strength strain-hardening cementitious composites, Cem Concr Compos. 104 (2019). https://doi.org/10.1016/j.cemconcomp.2019.103416.

[59] X. Dai, S. Aydin, M.Y. Yardimci, K. Lesage, G. de Schutter, Influence of water to binder ratio on the rheology and structural Build-up of Alkali-Activated Slag/Fly ash mixtures, Constr Build Mater. 264 (2020). https://doi.org/10.1016/j.conbuildmat.2020.120253.

[60] M.H. Khudhair, M.S. El Youbi, A. Elharfi, Data on effect of a reducer of water and retarder of setting time admixtures of cement pastes and mortar in hardened stat, Data Brief. 18 (2018) 454–462. https://doi.org/10.1016/j.dib.2018.03.050.

[61] W.X. Chen, F.K. Xiao, X.H. Guan, Y. Cheng, X.P. Shi, S.M. Liu, W.W. Wang, The application of waste fly ash and construction-waste in cement filling material in goaf, in: IOP Conf Ser Mater Sci Eng, Institute of Physics Publishing, 2018. https://doi.org/10.1088/1757-899X/292/1/012001.

[62] S.A. Wade, J.M. Nixon, A.K. Schindler, M. Asce, R.W. Barnes, Effect of Temperature on the Setting Behavior of Concrete, Journal of Materials in Civil Engineering. 22 (2010) 207–286. https://doi.org/10.1061/ASCE0899-1561201022:3214.

[63] L.E. Burris, K.E. Kurtis, Water-to-cement ratio of calcium sulfoaluminate belite cements: Hydration, setting time, and strength development, Cement. 8 (2022) 100032. https://doi.org/10.1016/j.cement.2022.100032.

[64] H. Li, K. Yang, X. Guan, Effect of water-to-binder ratio on the properties of CSA cement-based grouting materials with LiAl-LDH, Advanced Composites Letters. 29 (2020). https://doi.org/10.1177/2633366X20908876.

[65] A. Suwansaard, T. Kongpun, Impact of wet and air curing methods on developing compressive strength in concrete, Progress in Applied Science and Technology. 3 (2021). https://doi.org/10.14456/x0xx00000x.

[66] M.A. Uddin, M. Jameel, H.R. Sobuz, M.S. Islam, N.M.S. Hasan, Experimental study on strength gaining characteristics of concrete using Portland Composite Cement, KSCE Journal of Civil Engineering. 17 (2013) 789–796. https://doi.org/10.1007/s12205-013-0236-x.

[67] M.A. Caronge, M.W. Tjaronge, H. Hamada, R. Irmawaty, Effect of water curing duration on strength behaviour of portland composite cement (PCC) mortar, in: IOP Conf Ser Mater Sci Eng, Institute of Physics Publishing, 2017. https://doi.org/10.1088/1757-899X/271/1/012018.

[68] C. Namarak, C. Bumrungsri, W. Tangchirapat, C. Jaturapitakkul, Development of concrete paving blocks prepared from waste materials without Portland cement, Materials Science (MEDŽIAGOTYRA). 24 (2018) 92–99. https://doi.org/10.5755/j01.ms.24.1.17566.

[69] D. Belani, J. Pitroda, Fly ash (F-Class): opportunities for sustainable development of low cost rural roads, International Journal of Engineering Trends and Technology (IJETT). 4 (2013). https://www.researchgate.net/publication/281241714.

[70] D. Teo, C. Lee, T.S. Lee, The effect of aggregate condition during mixing on the mechanical properties of oil palm shell (OPS) concrete, ENCON . (2017).

[71] S.P. Palanisamy, G. Maheswaran, M.G.L. Annaamalai, P. Vennila, Steel slag to improve the high strength of concrete, Int J Chemtech Res. 7 (2015) 2499–2505. https://www.researchgate.net/publication/282267666.

[72] S. Arora, S.P. Singh, Flexural Fatigue Analysis of Concrete made with 100% Recycled Concrete Aggregates, Journal of Materials and Engineering Structures. 2 (2015) 77–89. https://www.researchgate.net/publication/293556754.

[73] K. Turk, C. Kina, M.L. Nehdi, Durability of Engineered Cementitious Composites Incorporating High-Volume Fly Ash and Limestone Powder, Sustainability (Switzerland). 14 (2022). https://doi.org/10.3390/su141610388.

[74] A. Kumar Ammasi, Strength and Durability of High Volume Fly Ash in Engineered Cementitious Composites, 2018. www.sciencedirect.comwww.materialstoday.com/proceedings2214-7853.

[75] S. Belayutham, C. Khairil, I. Che, I.· Anizahyati, A.· Hazrina, M.· Muntasir, B. Editors, Proceedings of the 5th International Conference on Sustainable Civil Engineering Structures and Construction Materials, Springer, 2020. https://link.springer.com/bookseries/15087.

[76] K.Q. Yu, W.J. Zhu, Y. Ding, Z.D. Lu, J. tao Yu, J.Z. Xiao, Micro-structural and mechanical properties of ultra-high performance engineered cementitious composites (UHP-ECC) incorporation of recycled fine powder (RFP), Cem Concr Res. 124 (2019) 105813. https://doi.org/10.1016/j.cemconres.2019.105813.

[77] L. Wei, Y. Wang, J. Yu, J. Xiao, S. Xu, Feasibility study of strain hardening magnesium oxychloride cement-based composites, Constr Build Mater. 165 (2018) 750–760. https://doi.org/10.1016/j.conbuildmat.2018.01.041.

[78] K. Yu, Y. Wang, J. Yu, S. Xu, A strain-hardening cementitious composites with the tensile capacity up to 8%, Constr Build Mater. 137 (2017) 410–419. https://doi.org/10.1016/j.conbuildmat.2017.01.060.

[79] H. Ma, C. Yi, C. Wu, Review and outlook on durability of engineered cementitious composite (ECC), Constr Build Mater. 287 (2021). https://doi.org/10.1016/j.conbuildmat.2021.122719.

[80] A. Fan, Y. Xiong, L. Yang, H. Zhang, Y. He, Carbon footprint model and low–carbon pathway of inland shipping based on micro–macro analysis, Energy. 263 (2023). https://doi.org/10.1016/j.energy.2022.126150.

[81] O. Andersen, S. Gössling, M. Simonsen, H.J. Walnum, P. Peeters, C. Neiberger, CO2 emissions from the transport of China's exported goods, Energy Policy. 38 (2010) 5790–5798. https://doi.org/10.1016/j.enpol.2010.05.030.

[82] United Nations Conference on Trade and Development (UNCTAD), Review of Maritime Transport 2022 - Chapter 3: Freight Rates and Transport Costs, 2022.

[83] U.S. Department of Transportation Federal Aviation Administration, AC 150/5370-10H - Standard Specifications for Construction of Airports, U.S. Dept. of Transportation. (2018).

[84] D.W. Ardana, A. Ariawan, The significance of concrete slab flexural strength inference variation based on its compression strength characteristics in apron pavement analysis and design, MATEC Web of Conferences. 276 (2019) 01038. https://doi.org/10.1051/matecconf/201927601038.

[85] ODOT, Rigid Pavement Design, Ohio Department of Transportation. (2019).

[86] M.L. Marceau, M.A. Nisbet, M.G. Vangeem, Life Cycle Inventory of Portland Cement Concrete, 2006.

[87] H.W. Chung, T. Subgranon, M. Tia, H. Deford, J. Armenteros, The effects of reduced paste volume in Portland limestone cement concrete, Magazine of Concrete Research. 73 (2021) 958–972. https://doi.org/10.1680/jmacr.19.00541.

[88] T. Hanein, J.L. Galvez-Martos, M.N. Bannerman, Carbon footprint of calcium sulfoaluminate clinker production, J Clean Prod. 172 (2018) 2278–2287. https://doi.org/10.1016/j.jclepro.2017.11.183.

[89] M.K. Mohan, A. V. Rahul, B. van Dam, T. Zeidan, G. De Schutter, K. Van Tittelboom, Performance criteria, environmental impact and cost assessment for 3D printable concrete mixtures, Resour Conserv Recycl. 181 (2022). https://doi.org/10.1016/j.resconrec.2022.106255.

[90] H. Zhu, D. Zhang, T. Wang, H. Wu, V.C. Li, Mechanical and self-healing behavior of low carbon engineered cementitious composites reinforced with PP-fibers, Constr Build Mater. 259 (2020) 119805. https://doi.org/10.1016/j.conbuildmat.2020.119805.

[91] D. Zhang, B. Jaworska, H. Zhu, K. Dahlquist, V.C. Li, Engineered Cementitious Composites (ECC) with limestone calcined clay cement (LC3), Cem Concr Compos. 114 (2020). https://doi.org/10.1016/j.cemconcomp.2020.103766.

[92] H.L. Wu, D. Zhang, B.R. Ellis, V.C. Li, Development of reactive MgO-based Engineered Cementitious Composite (ECC) through accelerated carbonation curing, Constr Build Mater. 191 (2018) 23–31. https://doi.org/10.1016/j.conbuildmat.2018.09.196.

Chapter 5. Conclusions

5.1. Concluding remarks

The need to mitigate CO_2 emissions to slow down global warming has become an increasingly pressing challenge for our generation. Engineered cementitious composite (ECC) offers a potential solution to reducing the carbon footprint of the built environment due to its remarkable tensile ductility, which enhances durability and provides a practical strategy to mitigate concrete CO_2 footprint for the structural product use phase. However, ECC's high cement content and synthetic fiber usage contribute to a significant CO_2 footprint during the material production phase. Therefore, effective strategies to decarbonize ECC are essential if this material is broadly used in future construction applications.

The research conducted in this thesis explored various approaches to decarbonizing ECC while quantifying the reduction of embodied carbon footprints and costs associated with each strategy. These approaches included carbon sequestration through carbonation curing, utilization of industrial waste materials (IWMs), and incorporation of localized materials. Mechanical performances, such as compressive, tensile, flexural, and fatigue performance, were experimentally investigated, along with the study of micromechanical properties, including matrix and fiber/matrix interface properties. A low-carbon sustainable ECC material is developed, and a localized ECC is also presented to demonstrate the effectiveness of these decarbonization strategies.

A series of experiments were performed to examine the impact of carbonation curing on ECC. The mechanical performances, such as compressive, tensile, fatigue, and flexural behaviors of carbonation-cured ECC, were improved due to the matrix densification and enhanced interfacial bond between the fibers and cement matrix. Carbonation curing resulted in 14~30% of CO_2 uptake by cement mass after a 24-hour curing period, thereby reducing the embodied carbon footprint of ECC by an average of 22% compared to typical M45-ECC while maintaining equivalent costs. To further decrease the embodied carbon footprint of ECC, various IWMs, such as fly ash, LC3 cement, waste polyethylene fibers (WPE), and waste foundry sands (WFS), were integrated with

carbonation curing to develop a low-carbon ECC. Sisal plant fibers were introduced to serve as conduits for CO_2 diffusion transport to increase carbon sequestration. The addition of sisal fiber in the low-carbon ECC enhanced carbon sequestration by 10%. In combination, use of IWMs coupled carbonation curing resulted in a low-carbon sustainable ECC material with a 50 % reduction in embodied carbon footprint compared to conventional concrete and a 33% cost reduction, demonstrating a promising approach to decarbonizing ECC.

It should be noted that in the discussion of IWMs, it is assumed that all IWMs are universally accessible, however, this assumption may not hold since some IWMs are not universally available in all regions of the world. A case study of the Kingdom of Saudi Arabia (KSA) explored the use of localized materials, such as volcanic ash and desert sand, to investigate the challenges facing ECC applications when certain key materials, such as fly ash, are unavailable locally. The use of volcanic ash resulted in excessive shrinkage and greater water consumption in ECC, but these issues were able to be overcome through the addition of CSA cement and use of water curing. Using locally available materials reduced the embodied carbon footprint of VA-ECC by 5% compared to FA-ECC, with a 14% cost reduction. Considering the potential for enhanced mechanical properties of ECC that utilizes locally available materials, the embodied carbon footprint can be further reduced by 22% compared to conventional concrete.

This research demonstrated the synergistic application of carbonation curing and use of IWMs to achieve a low-carbon ECC. Carbonation curing alone led to a 14~30% reduction in the embodied carbon footprint compared to M45 ECC. Using IWMs alone can reduce the embodied carbon footprint by 24~55% and reduce the cost by 80~86%. When incorporating carbonation curing and the application of IWMs, the embodied carbon footprint of ECC can be decreased by as much as 67~77%. This substantial carbon reduction highlights the effectiveness of combining these approaches as an efficient way to mitigate CO_2 emissions in ECC production. When the upper bound of the range of carbon and cost savings for the developed low-carbon ECC is compared with the lower bound of the range of carbon and cost for conventional concrete, a 24% of reduction in embodied carbon footprint and 10% of cost savings is achieved. This gives high confidence that these decarbonization approaches are viable even if we consider the worst-case estimate for carbon and cost reductions of low-carbon ECC. It is important to note that the impact of carbonation curing should be carefully considered when integrating these methods. In the case

of including new IWMs in the ECC mixture, carbonation curing may possibly impair the performance of ECC.

5.2. Research impacts, limitations, and future recommendations

The mechanical performance of ECC after carbonation curing was systematically investigated. The fatigue failure, crack propagation, fiber/matrix interface, and fiber failure modes of carbonation-cured ECC were studied via micromechanical observations. These findings demonstrate that the application of carbon sequestration through carbonation curing offers a feasible strategy for future decarbonization of ECC and can be combined with other decarbonization approaches, as shown in Figure 5-1.

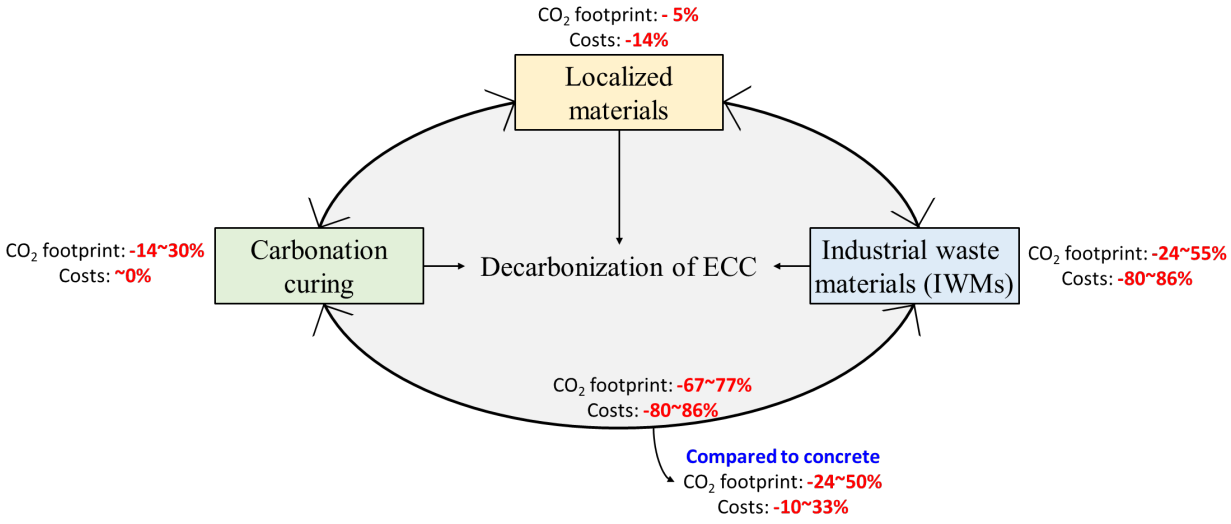

Figure 5-1. Integrated methods for decarbonization of ECC

This research lays the foundation for mitigating the embodied carbon footprint of the concrete industry, where ECC is the particular class of materials, demonstrating that use of low-carbon ECC can be a viable opportunity to support resilient and sustainable infrastructure. However, an important challenge lies ahead: translation of the methodologies and insights gained from decarbonization of ECC into traditional concrete applications.

While large-scale structures constructed with ECC have demonstrated successful casting and testing, further research is needed before applying the carbon sequestration method of carbonation curing in the conventional concrete industry because the carbonation curing used in this research was primarily conducted on a batch-scale and not applied to field-scale structures. Replicating the mechanical properties observed in batch-scale samples to larger field-scale elements presents challenges, particularly concerning the fiber dispersion and the lack of formation of multiple cracking behaviors when under stress, as evidenced in ECC railway ties. However, this research also highlights the potential of carbonation curing for scaled-up specimens if appropriate mixing and casting processes are adopted. Therefore, establishing a standard mixing and casting procedure for carbonation-cured infrastructures is highly recommended.

One solution to extend the decarbonization methodologies to a broader range of traditional concrete may be through the direct integration of pre-carbonated materials before the mixing and casting. Ground granulated blast-furnace slag (GGBFS) is a promising candidate for pre-carbonation, as it contains approximately 50% CaO and MgO, which facilitates CO_2 sequestration before concrete mixing. This approach not only overcomes previous barriers related to matrix densification but also improves CO_2 storage through mineral carbonation within large-volume specimens, thereby addressing the limitation posed by the slow diffusion of CO_2 into the material. This innovative strategy may provide a pathway for reducing cement usage in both ECC and traditional concrete, potentially leading to development of cement-free concrete materials in the future.

Addressing the carbon emissions of our concrete construction industry, especially in the concrete materials portion of the built environment, remains an urgent need. While the decarbonization of ECC shows the possible opportunities for lowering the carbon footprint of cementitious materials, there remains a need to extend these approaches to encompass a wider range of conventional concrete applications. This will require significant efforts to deal with potential performance challenges, such as the corrosion of steel rebar in carbonation-cured traditional concrete due to the decreased alkalinity and lower cement pore water pH environment. Despite the potential obstacles, maintaining a proactive approach to reduce carbon emissions associated with the concrete and cement industries is imperative to ensuring future reductions in the carbon footprint of the built environment.